UNIVERSITY OF SOUTHAMPTON

FACULTY OF HEALTH, MEDICINE AND LIFE SCIENCES

School of Medicine

DEVELOPMENT OF IMPROVED ANALYSIS OF RADIONUCLIDE IMAGES OF AEROSOL DEPOSITION

by

Spyridon Montesantos

A thesis submitted for the degree of

Doctor of Philosophy

April 2008

0

UNIVERSITY OF SOUTHAMPTON
<u>ABSTRACT</u>
FACULTY OF HEALTH, MEDICINE AND LIFE SCIENCES
School of Medicine

<u>Doctor of Philosophy</u>
**DEVELOPMENT OF IMPROVED ANALYSIS OF RADIONUCLIDE IMAGES
OF AEROSOL DEPOSITION**
by Spyridon Montesantos

Over the last few years, there has been an increase in the clinical methods targeting the human tracheobronchial tree, both for therapeutic and diagnostic purposes. For these methods to be effective, a good understanding of the lung structure is necessary. This knowledge can be attained through the use of medical imaging protocols such as CT and MRI, and can in turn be used to predict aerosol deposition for particles employed for inhalation therapy via the simultaneous use of radionuclide imaging. However, due to limitations imposed by the technologies currently available, not enough information can be gathered in-vivo about the respiratory tract. Consequently, widespread use of anatomical models of the lung is being made by clinicians in order to enable them to fill this gap in information. The thesis is concerned with the improvement of such models and the introduction of new, more advanced ones in an effort to accurately describe the human lung using mathematical and physical principles.

A method is developed for improving the Conceptual Model constructed in the Nuclear Medicine Department of Southampton General Hospital by incorporating to it real, patient-specific data obtained through CT imaging. A model of the bronchopulmonary segments of the lung is also created and an atlas that can be used for the identification of these sub-structures in any lung space is formed. An algorithm for the generation of a fully-descriptive 3D model of the airway tree is then designed and implemented, the morphometry of which is assessed to confirm that it is a realistic representation of the target organ. The deterministic algorithm reveals the 3D geometry and orientation of the lung airways, thus enabling aerosol deposition and flow-pattern studies to be performed in a comprehensive way in previously inaccessible regions of the lung.

Contents

List of Figures

List of Tables

Acknowledgements

I would like to thank my two supervisors, Professor John S. Fleming and Dr. Livia Bolt for giving me the opportunity to undertake this project while they provided a comprehensive academic training, which was almost as important as the advise and insight they offered that assisted me to overcome crucial difficulties throughout the duration of this study. I am indebted to Professor Fleming for his invaluable help that he provided in the form of extended discussions and by communicating his enthusiasm for this work as much as for the hard data without which no progress would have been made for the completion of this thesis.

I am grateful to Dr. Veronique Sauret; this study is basically a continuation, if not an extension, of her work, which provided me with all the necessary data to proceed with my research unobstructed.

I would like to thank my family and friends; none of this would have been possible without their love and their continuous and unconditional support. I dedicate the results of my arduous work to them.

I acknowledge the financial assistance provided by Astra Zeneca Lund Ltd., which provided me with the necessary funds to take up and complete this study.

Academic Thesis: Declaration Of Authorship

I, Spyridon Montesantos declare that this thesis and the work presented in it are my own and has been generated by me as the result of my own original research.
[title of thesis] DEVELOPMENT OF IMPROVED ANALYSIS OF RADIONUCLIDE IMAGES OF AEROSOL DEPOSITION

I confirm that:

1. This work was done wholly or mainly while in candidature for a research degree at this University;

2. Where any part of this thesis has previously been submitted for a degree or any other qualification at this University or any other institution, this has been clearly stated;

3. Where I have consulted the published work of others, this is always clearly attributed;

4. Where I have quoted from the work of others, the source is always given. With the exception of such quotations, this thesis is entirely my own work;

5. I have acknowledged all main sources of help;

6. Where the thesis is based on work done by myself jointly with others, I have made clear exactly what was done by others and what I have contributed myself;

7. Parts of this work have been published as: [please list references below]:

S. Montesantos, *"Airway Tree Models: The Hybrid Conceptual Model"*, University of Southampton, Faculty of Medicine, Health and Life Sciences Postgraduate Conference, 31, 2006.

S. Montesantos, J.S. Fleming and L. Bolt, *"The Hybrid Conceptual Model of the Human Lung"*, Proceedings of the 10th Medical Image Understanding and Analysis Conference, 1: 36-40, 2006.

Signed: ....

Date: ....

created with
nitro^PDF professional
download the free trial online at nitropdf.com/professional

Abbreviations

2D   Two-Dimensional

3D   Three-Dimensional

CT   X-ray Computed Tomography

FRC   Functional Residual Capacity

HCM   Hybrid Conceptual Model

HRCT   High Resolution CT

LL   Left Lower

LU   Left Upper

MRI   Magnetic Resonance Imaging

PET   Positron Emission Tomography

RL   Right Lower

RM   Right Middle

RU   Right Upper

SHCM   Segmental Hybrid Conceptual Model

SPECT   Single Photon Emission Computed Tomography

STD   Standard Deviation

TLC   Total Lung Capacity

Chapter 1

Introduction

1.1 Modern Aerosolised Medicine And The Need For Detailed Modelling Of The Lungs

The technical advances of the last century that benefited all areas of human knowledge have not left untouched the field of medicine. New equipment gave rise to the development of better techniques which, in turn, allowed for a more thorough examination of the human body. Furthermore, the social requirement of healthier and safer working places, along with the demand for a better quality of life resulted in a shift on the doctor's outlook on many issues concerning the diagnosis and treatment of disease.

Along these lines, the importance of aerosolised medications as a means of directly targeting both the respiratory and the circulatory system with non intrusive methods has increased. Today, when the lungs are the target organs, the prevalent treatments commonly include the utilization of aerosol medicine. The respiratory tract is used as the entry point to medicinal aerosol nebulae and the particles get deposited along the way to the inner parts of the lung, thus performing their healing functions. However, there is great variation in the effectiveness of these treatments due to several factors such as variation of anatomy between patients, dosage, particle size and particle geometry. Therefore, to increase the efficiency of the treatment, the prediction of the aerosol deposition with respect to the patient lung anatomy is necessary.

This can be achieved either with the use of external measurements, usually involving medical imaging techniques, or with the application of computer modelling of the aerosol deposition. However, both methods require the employment of anatomical models of the lung and, more importantly, of the airway tree. These models are based on the collection of anatomical data

from various lung casts or from CT images of the lung that display the airway tree down to a certain depth. However, since data collection and analysis of morphological data is tedious, not much information exists in the literature, making it difficult to make comparative studies in order to describe some of the most important aspects of the human anatomy such as inter- and intra-subject variability. Therefore, the existing models have to either follow average statistics or mathematical, semi-intuitive rules in order to describe the respiratory tract.

1.2   Objectives And Contribution Of This Study

The main purposes of this thesis are the creation of three-dimensional models of the lungs, focusing on the airway tree, and the verification of the validity of these models. Both of these will be done using medical image data. The objectives are:

- ➢ To revise previously created models for deriving the aerosol deposition per generation from the 3D spatial distribution of deposition measured using specific imaging protocols like CT and MRI.
- ➢ To develop new realistic and fully deterministic 3D models of the lung based on patient specific *in-vivo* image data and other statistical data.
- ➢ To confirm the validity of the resulting models using medical image analysis techniques and statistical analysis.

This work took place in within the Nuclear Medicine Group, department of Medical Physics, Bioengineering and Nuclear Medicine at Southampton University Hospitals NHS Trust under the administration of the Developmental Origins of Health and Disease division, School of Medicine, University of Southampton. The research is focused on the assessment of aerosol deposition within the airway tree using radionuclide imaging in conjunction with computer modelling.

created with
nitro^PDF professional
download the free trial online at nitropdf.com/professional

The main contribution of our work will be to provide the scientific community with new, realistic, statistically correct and patient specific models of the lungs with the purpose of improving the analysis of the deposition of inhaled particles on the different regions of the respiratory tract. This is done with the primary intention of both promoting the use of targeted inhalation therapy, which produces more effective and personalised treatments of various lung diseases such as asthma and cystic fibrosis, and for the resulting improvement of the cost/effectiveness ratio of the treatments based on aerosolised medicine. An equally important contribution will be made in advancing some existing techniques used for diagnosing lung disease, and in the prediction of the harmful effects of pollutants in particle form. Furthermore, an analysis on the airways in particular subspaces of the lung will be performed. This is an approach that, to the best of our knowledge, has not been followed before for the distal regions of the human lung. Finally, our models are intended to remove some weaknesses of previously suggested models in the literature, and to advance our understanding of the physical processes within the human lung.

1.3   Layout

The thesis will consist of 7 chapters and one Appendix.

Chapter 2 is concerned with the anatomical and morphological features of the human lung. The substructures it consists of and their functions will be described and some statistical data of their morphometry will be shown. Furthermore, some physics underlying the lung operation will be presented.

In Chapter 3 some medical imaging modalities relevant to the human lungs will be briefly reviewed and morphometric models presented in the literature will be described and investigated. Moreover, the main aerosol deposition mechanisms and some important models will be shown and a description of the fluid dynamic principles that dominate the airways will be made.

Chapter 4 presents the creation of the Hybrid Conceptual Model, which is an algorithmic method developed to describe airway tree morphology in the lung in a generalistic way. The results will be displayed and discussed with comparison to previous similar efforts.

In Chapter 5 the need for the segmentation of the lung in smaller, more manageable sub-spaces is discussed and a relative algorithm taking advantage of the pre-existing lung anatomical structures is explained. The Hybrid Conceptual Model presented in the previous chapter is revisited and adapted to fit the newer lung subspaces and the results of this modification are exhibited and examined.

Chapter 6 describes the development of the algorithmic process that generates the Deterministic Airway Tree Model and some tests to prove its functionality and consistency. Furthermore, the results of the algorithm are displayed and compared to previous similar efforts while the realism of the model is evaluated.

In Chapter 7 the conclusions of our study are drawn and some future work suggestions are made.

Appendix A contains the engineering flow charts through which the results of the algorithms in Chapter 6 can be reconstructed.

Chapter 2

Description of lung anatomy and function

2.1 Introduction

The purpose of this chapter is to lay the biological foundations that will have to be taken into account for the generation of our models in further chapters. First the morphology and morphometry of the lungs will be described and analyzed. The respiratory tract and its substructures will be detailed, along with the lobar and segmental structures of the pulmonary system. Furthermore, the air volumes and capacities that define lung function will be summarized. Finally, the anatomical information on the morphometry of these structures and some of the physics that underlie their function will be investigated.

2.2 The Human Respiratory Tract

The human respiratory tract includes the anterior nose and the posterior nasal passages, the mouth, the larynx, the pharynx (sometimes including the vocal cords), the trachea, the bronchi and the lungs. According to the ICRP (1994), it can generally be divided into four distinct regions: The **extra-thoracic region**, that comprises the anterior nose and the underlying nasal passages, larynx, pharynx and mouth; the **bronchial region**, that consists of the trachea (windpipe and voice box) and the bronchi; the **bronchiolar region**, consisting of the bronchioles and terminal bronchioles; and, finally, the **alveolar-interstitial region**, that consists of the respiratory bronchioles, the alveolar ducts and sacs and the interstitial connective tissue. An image of the several parts of the respiratory tract is displayed in Figure 2-1. All regions contain lymphatic tissue or some of its components.

created with nitro PDF professional
download the free trial online at nitropdf.com/professional

2.2.1 Regions Of the Respiratory Tract And Their Anatomy

The Extra-Thoracic Region

The main function of this part of the respiratory tract, besides conducting the inspired air to the trachea and the lungs, is the conditioning, cleaning and filtering of the inhaled air. Usually, the air inspired through the nose is enough to maintain the oxygen balance in the body. However, an auxiliary path that includes the mouth exists, in case of nasal obstructions or additional demands on oxygen. The inspired air leaves the nasal cavity and enters the nasal pharynx, before continuing to the oral pharynx, the larynx and the trachea. At the intersection of the nasal and the oral pharynx, which is covered by a mucous membrane, the food is prevented from entering the respiratory tract by the epiglottis, which automatically moves to cover the respiratory passage during swallowing. The smell receptors are located at the top of the nasal cavity.

The entry of the nasal passage is filled with hairs that are used for the purpose of air filtration. This region also contains associated lymph vessels and nodes. Most of the nasal wall is covered by respiratory mucosa, which contains a complex vascular system and many glands. It is also covered by a ciliated epithelium that moves a layer of mucus in the lower nasal passages. Epithelium is defined as the type of cells covering the internal and external surfaces of the body, including the lining of vessels and other small cavities, while a cilium (plural cilia) is a micro-tubular, hair-like structure that cover the cells of some tissues and help those cells sweep away fluids or particles. These passages are covered by ciliated, pseudostratified epithelium. The oral part of the pharynx is covered by a membrane with stratified, squamous epithelium.
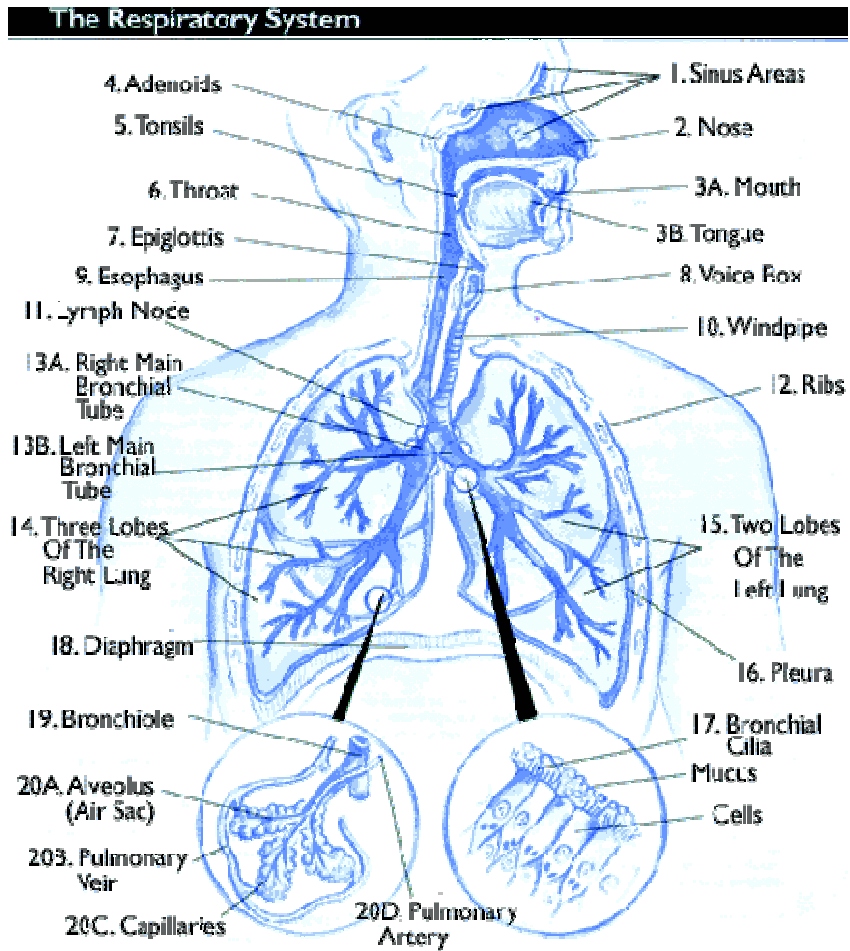
Figure 2-1: The human respiratory tract. (Obtained from the American Lung Association internet site, web address http://www.lungusa.org/site/pp.asp?c=dvLUK9O0E&b=22576. Reprinted with permission. © 2008, American Lung Association.)

The Bronchial Region

This region is part of the air conducting system within the thorax. The purpose of this part of the respiratory tract besides conducting air is to adjust the humidity and temperature of inspired air. Due to the morphology and the bifurcating branching structure of the respiratory tract below the trachea, the tract is usually referred to as the airway tree, with the trachea being the main stem branching down to bronchi, bronchioles and alveoli. Each new branch is usually referred to as a generation. The bronchial region is considered to consist of the first eight branchings out of the trachea, i.e. the first 8 generations, with the trachea being generation zero. More information about the morphometry, morphology and identification of branches of the airway tree will be given in Section 2.5.

The trachea has tubular form and is lined with C-shaped cartilaginous rings that keep it open, supporting the air flow during a breathing cycle. Typical size values for the trachea are 0.09m in length, 0.017m in inner diameter and $2x10^{-5}$ m^3 in volume. The trachea branches dichotomously to the main bronchi at the carina, and the branching process continues with relatively little irregularity throughout both the bronchial and bronchiolar region. Finally, the average diameter and length of the branches decreases as they penetrate deeper into the lung.

Though the bronchial wall composition remains the same for the first few branchings, the tissue becomes softer as the branching infiltrates deeper into the lungs, until the cartilage gradually disappears. Besides the cartilage plates, the walls of the trachea are covered by respiratory mucosa and contain many glands. Throughout the intra-thoracic gas transport system, the airway walls are lined with ciliated cells interspersed with mucus-secreting goblet cells and other secretory cells.

The Bronchiolar Region

This is the second part of the intra-thorax air conducting system. It consists of bronchioles, starting from the bronchi distal to the terminal bronchioles where transfer of air stops and the gas exchange becomes the primary function. Though there is great variation as to the depth of the lung where the bronchioles and, therefore, the alveoli appear, it is generally agreed that the conducting system transforms into the gas exchange system after an average of 15 [Weibel (1963), Horsfield and Cumming (1968), Raabe et al. (1976), Yeh and Schum (1980)] bifurcations from the trachea. The last conducting branches are called terminal bronchioles; all airways beyond them carry alveoli.

The bronchioles don't contain cartilage or glands. By definition, airways without cartilage are termed bronchioles. The cartilage is replaced by smooth muscle, which makes the airways prone to collapse if overly compressed. This is avoided with the intermingling of elastic fibres with the muscle tissues that completely surround the airways. Furthermore, the ciliated cells, which are pseudo-stratified columnar cells in larger airways, become cuboidal in this area of the lung. In addition, the mucus secreting cells are substituted by a special type of secretory cells called Clara cells, which are particularly evident at the terminal bronchioles. Clara cells actively divide

and differentiate to form ciliated cells which are also able to metabolise airborne toxins.

The Alveolar-Interstitial Region

This is the part of the respiratory system where the gas exchanges occur. It comprises the respiratory tract system distal to the terminal bronchioles, which is approximately from generation 16 to 26, though it is known to go as deep as generation 32. It consists of the respiratory bronchioles, which are the first bronchioles to present alveoli, thus combining both gas transfer and exchange behaviour, and the alveolar ducts and sacs, as well as lymphatic tissues and vessels. The portion of the lung supplied by a primary respiratory bronchiole is called an acinus and is usually treated as a single unit for all practical purposes due to the microscopic sizes of its parts. All airways within an acinus participate in gas exchange.

According to Haefeli-Bleuer (1988), the number of alveolated airways connecting the terminal bronchioles to an alveolar sac is an average of 9. In these airways the whole circumference is occupied by alveoli. The gas exchange region terminates in alveolar sacs, which are closed at the peripheral end by a group of alveoli. The alveoli are tiny hemispherical cavities supported by a thin elastic porus membrane. They borrow their name from the Latin word for hollow or cavity. The alveolar sacs are groupings of alveoli, interconnected through the pores on the alveolar surface, which are called pores of Kohn and allow for gas transfer between them. As can be seen in the drawing of Figure 2-2, the acini are also connected with the vascular system, thus accommodating gas exchanges of O_2 and CO_2 with the blood.

19
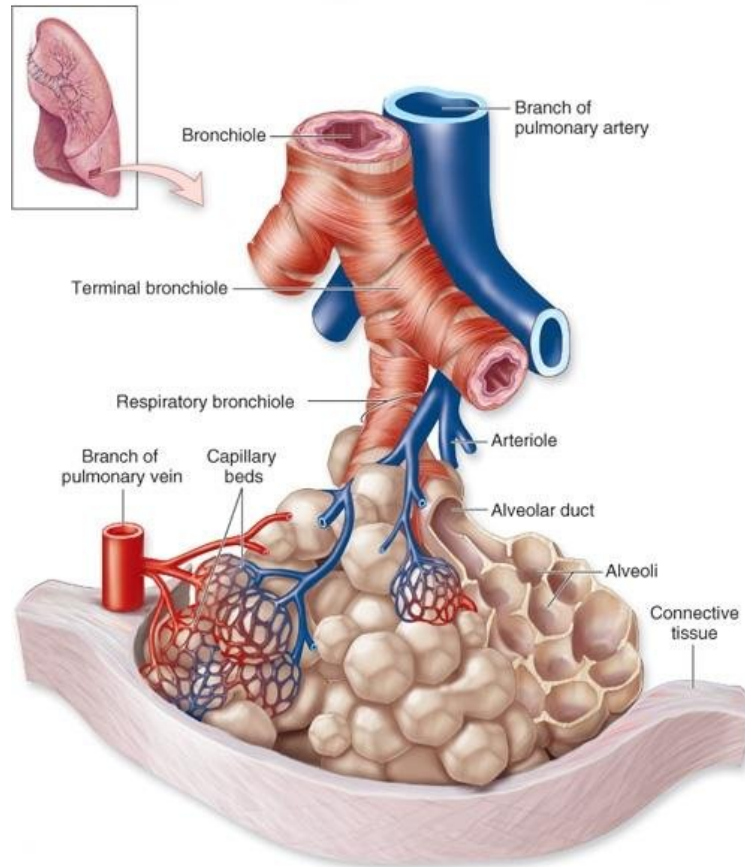
Figure 2-2: Drawing of the human pulmonary acinus structure, along with parts of the vascular system. (Image obtained from Kellogg Community College internet site, web address http://academic.kellogg.edu/herbrandsonc/bio201_McKinley/Respiratory%20System.htm. Reprinted with permission. © 2008, The McGraw-Hill Companies, Inc.)

The alveolar ducts and the alveoli are lined with a simple squamous epithelium composed of type I and type II alveolar cells. Type I alveolar cells cover about 95% of the alveolar surface, they are unable to divide, and they form a thin, blood-gas barrier through which gas exchange occurs. Type II alveolar cells are cuboidal in shape and are able to differentiate into both type I and type II alveolar cells. Type II cells secrete a pulmonary surfactant which decreases the surface tension of the alveolar surface, allowing the alveoli to expand during inspiration, and preventing their collapse during expiration. Bordering the lumen of the alveoli are wandering cells called alveolar phagocytes, or macrophages. These cells are part of the respiratory immune system mechanisms and are used to reject foreign bodies. These

protection mechanisms will be presented in more detail in subsequent sections in this chapter.

2.2.2 Functions Of The Respiratory System

The main function of the respiratory system is the transfer of oxygen, and its exchange with carbon dioxide. Fresh air containing the necessary oxygen is inhaled and inspired into the lungs through the conducting airway tree. The necessary power for the air to flow is produced by the respiratory muscles after the command of the central nervous system. Blood with low density in oxygen and high in carbon dioxide is pumped by the right heart ventricle into the lungs, where the gas exchange takes place. The blood, which now has high content of oxygen, flows back into the left side of the heart from where it is then distributed throughout the body.

However, there are other significant functions of the respiratory system, which come as a by-product of the rules that dictate its performance. First of all, increases of carbon dioxide levels in the body can increase hydrogen ion concentration. As a consequence, the respiratory system can regulate and control the acid-base balance of the human body, using the help of sensors connected to the central nervous system. Other significant functions that have to be taken into account are the phonation, which is generated by the flow of air through the vocal cords and the respiratory tract's participation in the defence mechanisms of the human body. Finally, the lungs can contribute to the whole metabolic process of the body with the existence of cells that can produce, metabolise or modify naturally occurring substances through the use of enzymes.

2.3   The Lungs

The lungs are paired organs placed in either side of the thorax. They are separated from each other by the heart and the other contents of the mediastinum, as shown in Figure 2-3. Both lungs are enclosed and protected by the pleural surface. Their pleural surface is of a light, porous, spongy texture, while the organs themselves are highly elastic to help the function of respiration. Besides the bronchial and acinar structures which belong to the respiratory tract, the lungs also contain blood, nerves

and lymphatic vessels. The lungs are heavier in males than in females, constituting on average $1/37^{th}$ and $1/43^{rd}$ of male and female body weight respectively.

Each lung is of conical shape and has an apex, a base, 3 borders and 2 surfaces. The base of the lungs is broad, concave and rests upon the diaphragm, which separates the right lung from the right lobe of the liver, the stomach and the spleen. To accommodate these organs, the diaphragm is slightly higher on the right side than on the left, which makes the right lung about 10% shorter but broader and thicker than the left lung. For that reason the right lung is also heavier and has greater capacity.

The lungs lie on the ribcage both posteriorly and anteriorly. The surface of the lungs that lies on the thorax is called costal surface and its shape matches closely the position of the ribs in the chest. The rest of the lung surface is in contact with the mediastinal pleura, from which it takes its name. It presents a deep concavity, which is larger and deeper on the left side, called the cardiac impression. This concavity contains the pericardium that lies in the region called the cardiac notch. Above and behind the notch is a triangular depression called the hilum, where the structures that form the root of the lung enter and leave the viscus. The root is on the mediastinal area at about $1/3^{rd}$ total-lung-height distance from the apex and it connects the lung to the heart and the trachea.
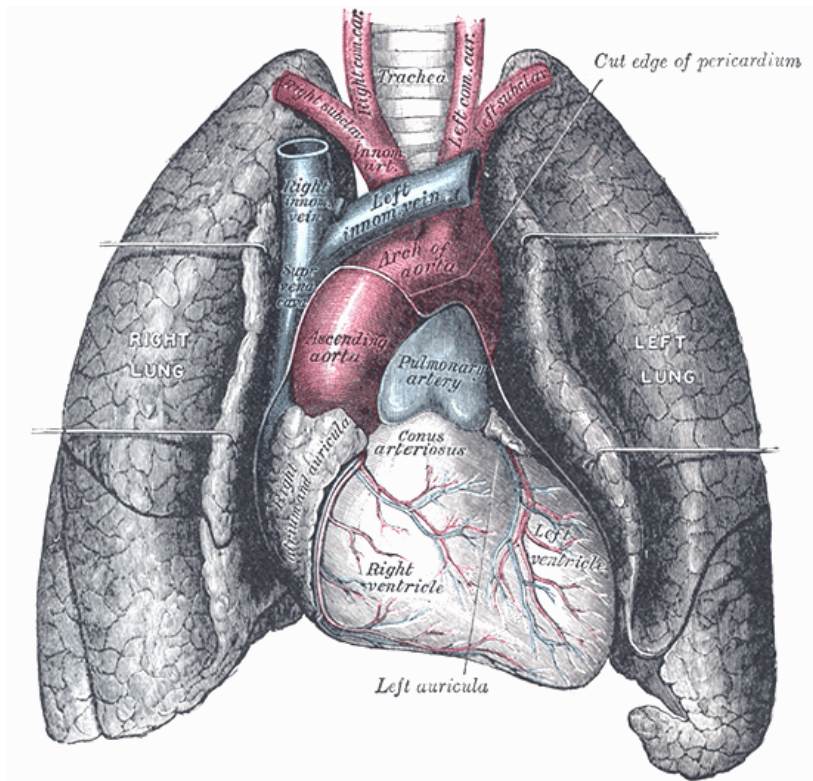
Figure 2-3: The lungs and the interstitial area that separates them. (Image obtained from the Bartleby.com internet site, web address http://www.bartleby.com/107/illus970.html. Permission to reprint not applicable.)

Finally, the lungs are divided into lobes, the left lung in 2 lobes, the left-upper (LU) and left-lower (LL), and the right lung into 3 lobes, the right-upper (RU), right-middle (RM) and right-lower (RL). These lobes are separated by intralobular fissures. The single fissure of the left lung runs diagonally from the upper and posterior part of the mediastinal surface to the lower and anterior part of the costal surface. In the right lung, the lowermost fissure follows the one in the left lung but in a more vertical orientation, while the uppermost fissure begins at the same point as the previous one and runs almost horizontally forward, thus creating the wedge-shaped middle lobe, which is the smallest of the 3 in the right lung.

The lobes themselves are divided into 10 lung tissue substructures called bronchopulmonary segments. These segments are independent from each other and can only be fully identified *ex-vivo*. The shape and topology of each lobe and segment can be visualised with the help of atlases of excised lungs that exist in the literature (good modern atlases can be found on the internet site

http://www.anatomyatlases.org). However, though the intersubject variability of these formations is great, no attempt for quantifying this variability could be found in the literature.

2.3.1 Additional Structures Of The Respiratory System

The Muscles Of Respiration And The Chest Wall

Since the lungs are not capable of inflating themselves the force for this inflation must be supplied by the muscles of respiration. The chest wall must be intact and able to expand if air is to enter the alveoli in a normal fashion. The primary components of the chest wall are the rib cage, the external and internal intercostals muscles and the diaphragm. These are the main muscles of respiration. Other muscles that participate in the breathing cycle are the abdominal muscles, the parasternal intercartilaginous muscles and the accessory muscles of inspiration.

The Central Nervous System and Neural Pathways

Another important component of the respiratory system is the central nervous system. Unlike cardiac muscle, the muscles of respiration do not contract spontaneously, which means that each breath must be initiated in the brain and the message must be carried via the spinal column to the appropriate nerves for the respiratory cycle to occur. The respiratory centre for spontaneous automatic breathing is located in the medulla and it serves as the interface between higher brain functions and the respiratory system.

2.4 Air Volumes, Capacities And The Respiratory Cycle

The average pair of lungs can hold about 6 litres of air but only a small amount is used during normal breathing. Different lung volumes and capacities measure various features about the lungs and are mainly used for diagnostic purposes. Though these volumes show intra- and inter-personal variation, some average values are typically used as references.

Air volumes are generally measured either directly by spirometry or they are calculated using the directly measured values. The 4 directly measured lung volumes are the following:

➢ Tidal Volume (TV): The amount of air that can be breathed in or out during normal respiration. It is normally from 400 to 500ml.

➢ Inspiratory Reserve Volume (IRV): The additional gas that can be inhaled after a normal tidal breath in. This is about 2500ml.

➢ Expiratory Reserve Volume (ERV): The amount of additional air that can be breathed out after normal expiration. This volume is usually around 1500ml.

➢ Residual Volume (RV): The amount of gas left in the lungs after maximal exhalation. The average value of this is 1500ml.

Other important volumes and capacities that are calculated based on the above are:

➢ Functional Residual Capacity (FRC): It is the amount of air left in the lungs after a tidal breath out. It can be found as the sum of

$$FRC=ERV+RV$$

which brings it in the area of 3000ml. The FRC is the usual marker of normalisation between different people.

➢ Inspiratory Capacity (IC): It is defined as the volume that can be inhaled after a tidal breath out and is given by the formula

$$IC=IRV+TV$$

➢ Vital Capacity (VC): It is the maximum volume of air that can be expelled at the normal rate of exhalation after a maximum inspiration. It is calculated through the formula

$$VC=IRV+TV+ERV=IC+ERV,$$

and is usually around 4500ml.

➢ Total Lung Capacity (TLC): This is the volume of gas that is contained in the lungs at the end of maximal inspiration. It is given by the formula

$$TLC=IRV+TV+ERV+RV=IC+FRC$$

and, as mentioned above, it is usually around 6000ml.

➢ Anatomical Dead Space: The volume of the airways, usually around 150ml.

The Total Lung Capacity depends heavily on a person's age, weight, sex and physique. Females tend to have 20-25% lower capacity than males. Lung capacity is also affected by altitude, due to atmospheric pressure changes and lower oxygen density in the air. The results of spirometry and the indirect calculations can be used to divide pulmonary diseases into restrictive, where volumes are decreased, and obstructive, in which volumes are normal but air flow is impeded, thus reducing flow rates. All the above measures and their corresponding average values can be observed in the graph of Figure 2-4. It is worth noting that with advancing age, the airways and tissues of the respiratory tract lose their elasticity, which is also the case for the chest wall. This results in a reduction of vital capacity, which in turn makes elderly people more susceptible to pulmonary diseases like pneumonia and emphysema.
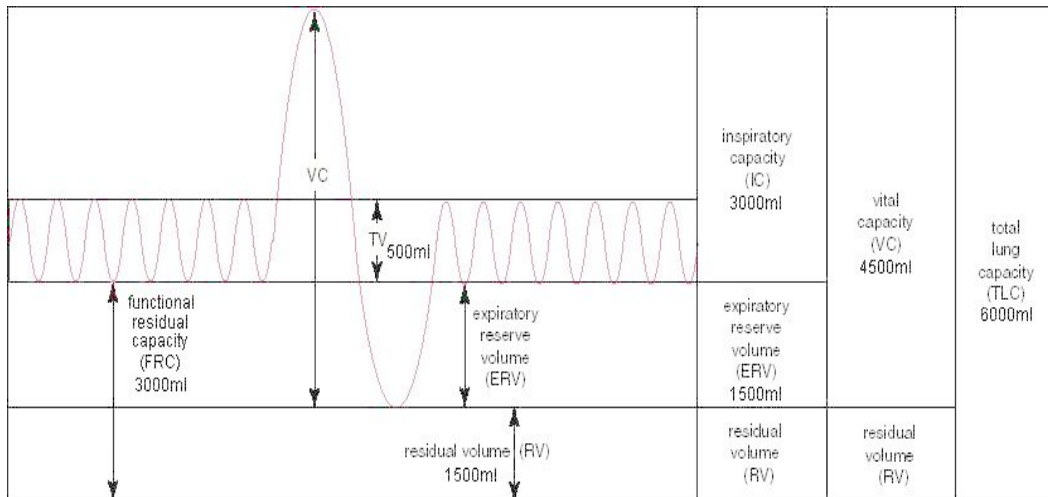
Figure 2-4: Typical air volumes and capacities in the respiratory system.

Finally, 2 commonly used quantifiers of lung volume are:

➢ Physiologic Dead Space, which is the volume of the airway tree of the lung that does not participate in gas exchange. In normal lungs, that is equal to the Anatomic Dead Space, but it is greater in lungs where disease is detected.

➢ Forced Expiratory Volume in 1 second (FEV1), which is defined as the volume of air that can be expired in 1 second after maximal inspiration. It is normally 80% of the vital capacity, expressed as the ratio FEV1/VC. In obstructive lung disease FEV1 is reduced more than the VC, thus the ratio is less than 0.8.

2.5   The Airway Tree In Man

The human bronchial tree consists of the trachea, the main, lobar and segmental bronchi all the way down to the terminal bronchioles and the acini.

2.5.1 Pre- And Neo-Natal Growth Of The Human Airway Tree

Intra-uterine development of the lung in a human foetus can be classified into four phases [Burri (1984)]. The first phase is called embryonic and it goes on for the first 5 weeks of gestation. In the first few weeks of development, a single pouch develops in the laryngotracheal groove. The lung bud divides into two as the endodermic epithelium pushes out into the mesenchyme investing the lung buds, forming a series of branching tubular structures. The ridges defining the laryngotracheal groove begin to hump up and fuse to separate the trachea from the oesophagus. The endodermic brunching continues and by week 5 the trachea is completely separate from the oesophagus. By the end of this period, the lobar structures are established.

The second phase is named pseudo-glandular phase and it is defined as the period between weeks 6-16. The branching leads to the foundation of the segmental patterns within the lobes, which take their final adult form, including the intralobar fissures, by the twelfth week of gestation. Internally, the lung looks like any other gland until week 10, when a burst of bronchial proliferative activity which lasts 6 weeks starts. During these 6 weeks, cartilaginous differentiation that begins at the trachea spreads centrifugally in concentric spheres down the bronchial tree, which appears to be already defined by the end of this phase. Muscular differentiation also begins late in this period.

The next phase starts at week 17 and continues on for about 10 more weeks. It is called the canalicular phase, in which the bronchi continue to divide in order to produce the airway tree down to the bronchioles. Radial extension of cartilage, muscle and elastin differentiation continues during this period and by its end, smooth muscle has reached the bronchiolar depth. Furthermore, toward the end of the canalicular phase the cell differentiation into terminal bronchioles and potential alveolar ducts occurs. This differentiation between bronchiole and acinus gives birth to the 4th and final phase, termed the alveolar phase.

The alveolar phase, also known as the terminal sac phase, is identified as the period of time from week 27 onward. During this period the epithelium lining the terminal

acinus rapidly attenuates, and capillaries develop along the sub-epithelial plane, protruding into the potential air space, creating what may be described as air-blood barriers. In addition, at some point between weeks 28 and 32, the alveoli are completely formed, with the process of alveolation starting at the alveolar sacs just before the 40th week of gestation.

At full term, the centripetal conversion of terminal bronchioles into respiratory bronchioles and the subdivision of existing alveoli begin. Though most of the airway tree is formed prior to birth, smaller airways and the acinar space continue to develop rapidly until the 3rd year of the child's life. It is suggested that the process of filling the human lung space continues throughout the human adult life, however no clear evidence for this exists. Still, at the age of 3, the human lung has almost taken its final configuration and very small variation is introduced henceforth.

2.5.2 Threats And Protective Mechanisms Of The Airway Tree

Of all the organs in the body, the lungs present the largest surface in contact with the environment, somewhere in the area of 50 to 70m^2, exposing the delicate lung tissues to about 10^4 litres of air each day. This section will briefly describe the threats to the airway tree and the protective mechanisms it employs to secure its functionality.

The air inhaled is almost invariably cooler than body core temperature and is not saturated with water vapour. This is a potential danger to the alveoli that must be protected from the cold and from drying out. Though most of the conditioning of the air happens in the upper respiratory tract (Section 2.2.1), some portions of this function occurs in the trachea and upper airways of the bronchial tree, especially during forced inspiration.

In addition to the above, inhaled dust and other pollutants in particle form with diameter smaller than 3μm have good chances of bypassing the upper respiratory tract filtration system, mainly in the nasal passage, and penetrating the tracheobronchial tree, where they get deposited into different depths and locations according to their size and shape. The potential threat to the well-being of the lung can be clearly seen since an average human living in a clean environment inhales about 10^{10} dust particles per day. The particle deposition mechanisms in the human tracheobronchial tree will be described and discussed in Chapter 3.

created with nitro PDF professional

download the free trial online at nitropdf.com/professional

Filtered material trapped in the airway tree can be removed with the use of two principal mechanisms: Reflexes in the airways, expressed in the form of cough, and mucociliary clearance. The airway reflex mechanisms are activated after mechanical or chemical stimulation of receptors anywhere in the respiratory tract and they may produce contraction of the bronchial smooth muscle to prevent deeper penetration of the irritant. At the same time intrapleural pressure rises and the larynx remains closed until it suddenly opens to produce explosive expiration with very high air velocity, sometimes reaching the speed of sound. However, the air velocity required to shear irritants from the mucus lining the walls of the bronchial tree can only be attained in larger airways, thus making this clearing mechanism appropriate only for the first few generations of the tree. The cough reflex is also useful in helping the airway mucus to move toward the nose or mouth.

As mentioned in Section 2.1, the entire respiratory tract, from the upper airways down to the terminal bronchioles, is lined by a mucus-covered ciliated epithelium. The cilia lining the airways pulse in such a way that the mucus covering them is always moved up the airway, toward the pharynx [King et al. (1974)]. The pulse frequency is between 1000 and 1500 beats per minute and the mucus linear velocity ranges from 0.5mm/min in the smaller airways to 20mm/min in the trachea. All particles caught in the mucus layer will move with it until they reach the pharynx, where they get excreted from the body in various ways.

Coughing is ineffective in small airways and mucociliary transport is absent beyond the terminal bronchioles. For those reasons, other cleaning methods are required to keep the respiratory tract unobstructed. This function is being performed by the alveolar macrophages, phagocyte cells that scavenge particulate matter of small diameter and defend against bacterial and viral threats that get inhaled with it. The failure of these macrophages is believed to be a contributing factor for the development of diseases such as pneumonia, tuberculosis or cystic fibrosis [Green et al. (1977)].

Other hazards to the bronchial tree may include noxious gases and smoke, from tobacco to riot control chemical and fire fumes. Even the inhalation of matter from the alimentary tract can cause the lung serious danger since, if not effectively cleared, it can cause pneumonia. All these are dealt with by the defence mechanisms discussed above. If these are not enough, the lung utilises the general immune system of the body.

2.5.3 Anatomy Of The Bronchial Tree

As mentioned in Section 2.2, the trachea is a tubular passageway lined by C-shaped cartilaginous rings that provide support against the collapse of the tracheal wall during inhalation. It extends from the larynx to the 5th vertebrae (T5), where it divides into the left and right main bronchi at a ridge called the carina. The carinal wall is extremely sensitive for triggering a cough reflex.

The two main bronchi enter the lungs at the hilus, the left bronchus in a more horizontal fashion, being longer and narrower than the right. On entering the lung, the main bronchi subdivide to form the lobar bronchi, 2 in the left and 3 in the right lung. The branching continues, usually in a binary way, though trifurcations may occur, to form smaller airways, the segmental (tertiary) bronchi, which in turn divide into several generations of bronchioles.

From a fluid dynamics point of view, the design of the airway conducting system is optimal for transferring fluids of gaseous form, air in this case, between the atmosphere and the gas exchange structures deep in the lungs. This is done by minimizing the airflow resistance with the adoption of appropriate cross-sectional areas, lengths, branching and planar angles, which are actually the main characteristics of each airway. The purpose is to accommodate the principle of minimal work evident in the biological structure of all organisms. The relationships between airway dimensions and flow dynamics will be investigated in Chapter 3. It is obvious that the dimensions of the airways tend to change *in vivo* due to airway compliance and the movement induced by the muscles of respiration. Airway compliance is of particular importance when air flows are limited, i.e. during forced breathing. Macklem et al. (1963) suggests that small diameter airways collapse rather often, a situation which gets worse in patients with asthma.
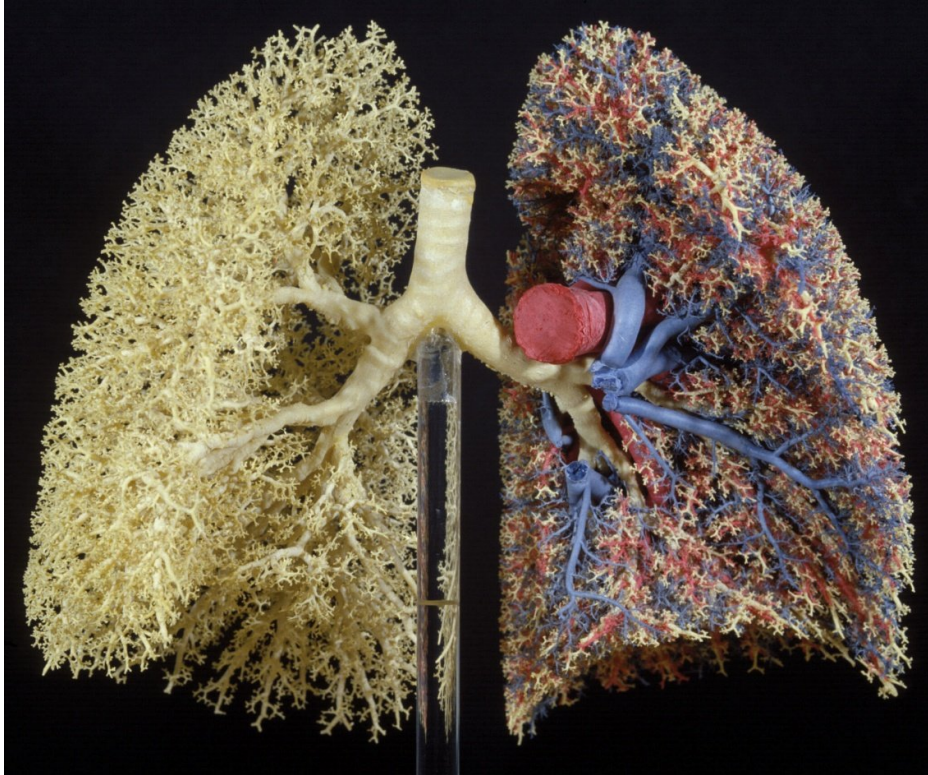
Figure 2-5: Photograph of a rubber cast of the human airway tree, including the pulmonary vascular system.

2.5.4 Morphometry Of The Bronchial Tree

Human lung morphometric data such as diameters, lengths, branching and planar angles are derived either from hand-made measurements conducted on airway tree casts (Figure 2-5) or through computer analysis of lung medical images obtained via protocols like Computed Tomography (CT) or Magnetic Resonance Imaging (MRI). The CT method, especially when it is in High Resolution mode (HRCT), dominates research in the last decade, however new methods that involve MRI scans of hyperpolarised noble gases are being developed for clinical applications involving the bronchial tree.

Weibel (1963) provided the first detailed measurements of the lengths and diameters of airways by evaluating all the airways in the first 6 generations of the tracheobronchial tree, as well as sampling all other generations, using 5 normal

human resin and silicon rubber casts inflated to 75% TLC. Horsfield and Cumming (1967) used a resin lung cast of a 25 year old male, inflated to 5 litres, which corresponded to the position of inspiration in life. Raabe et al. (1976) produced what has come to be known as the Lovelace data by measurements on silicon rubber replica casts of a 50 and a 60 year old male. Schlesinger and McFadden (1981) used a 29 year old male and a 59 year old female to produce negative hollow wax casts for their studies. Finally, in 1983, Mortensen et al. used 11 casts of children aged from 0-21 years. Unless stated otherwise, the lung casts were inflated to almost ¾ TLC, which corresponds to the lung volume at the end of inspiration during tidal breathing.

A different approach made its appearance in 1992, when McNamara et al. (1992) used HRCT in order to measure airway dimensions in excised canine lungs. A similar method for computationally segmenting and measuring three-dimensional pulmonary trees was applied to the human bronchial tree by Wood et al. (1995). Instead of manual quantification of individual airways, a semiautomatic computer algorithm was developed to take advantage of computer power and medical imaging advances. Brown et al. (1998) adjusted these techniques in order to use them in several clinical applications such as the measurement of abnormalities in asthmatic lungs. Sauret et al. (1999, 2002) first performed CT scanning on a human lung plastic cast, followed by a 12cm long CT scan on a healthy 27 year old male for the extraction of morphological information. Related methods were used by Aykac et al. (2003) and Schmidt et al (2004), who produced analytical human airway tree structures based on HRCT images of a rubber cast, as well as by Chatuverdi et al. (2005) who modified his methods to fit research of small animal pulmonary structures. Finally, comprehensive statistical data are presented by Tawhai et al. (2004) who performed multidetector row X-ray-CT (MDCT) on several human volunteers at 90% vital capacity.

There are several advantages using medical imaging to extract structural information from the airway tree. First of all, the methods used are automatic and systematic, thus avoiding errors in the identification of airways and the classification of data. Angular data are now easier to compute, filling a crucial gap in the relevant literature. Finally, information on secondary geometrical aspects of the airway tree that are of great importance to specific applications, like the curvature of bifurcation, can be investigated. However, measurements on angles are still dependant on the particular skeletonization process applied.

In addition to the above, there is a debate as to whether it is better trying to get information *ex-vivo* or *in-vivo*. Even though obtaining data *in-vivo* has inherent difficulties, such as involuntary movement or the need for application of registration techniques to make the results reproducible, lung casts are suggested to be prone to deformation due to inflation [Thurlbeck and Horsfield (1980)].

Airway Identification Systems

Before proceeding, some concepts relating to branching systems require discussion. When a branch, named "parent", divides, it divides into "daughters". If there are two daughters, which is mostly the case with the human airway tree where only occasional trichotomies occur, then the branching is called dichotomous. If the daughters divide, then they become parents and the process may continue until no more parents exist in the structure. In tubular dichotomous branching systems, the daughter with the higher diameter is referred to as the primary daughter. The original branch is called the stem. The final daughters are labelled as leaves. The airway tree is hence described as a sequence of irregular dichotomies.

There are two different systems for the classification of the airways of the airway tree, with many different variations of each used in the literature. The first way, introduced by Weibel (1963) is to count down the tree by generations, i.e. if the parent belongs to generation n, its daughters belong to generation n+1. The trachea may be set to be either generation 0 [Weibel (1963)] or 1 [Phalen et al. (1978), Koblinger and Hoffman (1985)]. This system of numbering tends to be straightforward and can be used almost directly in many different ways. The simplest way is a modification of the method used by the Lovelace group [Raabe et al. (1976)] described by Sauret et al (1999), according to which the digit 1, 2 or 3 is added to a number identifying each parent to define its daughters, while the structural information of the airways are stored elsewhere. The generation number is found by the number of digits in this ID. The main drawback of this technique is that, since the acinar regions in the periphery of the lungs can be reached along pathways of varying lengths and number of bifurcations, tubes with different biological functions may belong to the same generation.

In order to avoid this unwanted characteristic, Horsfield and Cumming (1967), inspired by methods used by geographers to describe the branching of rivers, proposed a different approach. According to their method the airways are counted

upwards in orders, from the periphery toward the trachea. While this is relatively easy to do in symmetric systems, certain difficulties arise when the system is asymmetric. In such a case, when two daughters with different orders meet, the parent gets an order number one unit greater than that of the daughter with the larger order number. An additional problem introduced by this numbering method is how to identify the starting points. Horsfield and Cumming (1968) designated the first tubes with diameters higher than 0.7mm as starting points (order 1). The Horsfield numbering method, though not as straightforward as the Weibel one, is frequently used in systems with clearly defined and similarly structured leaves [Schmidt et al. (2004)].

Diameters And Lengths Of The Bronchial Tree

Diameters and lengths and their relationships are the airway tree characteristics that have been most thoroughly investigated in the past, partly because they are the geometrical elements most easily measured on lung casts. Both the range and the average of the diameters and lengths decrease as the tree branches deeper into the lung. Due to strong inter- and intra-subject variability, the quantification is made using ratios such as the length-to-diameter ratio, daughter-to-parent diameter or cross-sectional ratio between parent and primary daughter or primary and secondary daughter, which serves as a commonly used estimator that measures the asymmetry of the tree. The quantification is based on either statistical analysis of tabulated data [Weibel (1963), Horsfield and Cumming (1968), Raabe et al. (1976), Koblinger and Hofmann (1985), Wood et al. (1995), Sauret et al. (2002)] or on the application of fluid dynamics principles [Uylings (1977), Pedley (1977), Andrade et al. (1998), Kitaoka et al. (1999)].

Weibel (1963) was the first to measure the length-to-diameter ratio for all airway diameters ranging from 1mm to 4.5mm; he calculated it to consistently remain around the value 3.25. Phalen et al. (1978) estimated the same ratio to be 2.8, where Yeh and Schum (1980) had discrepancies in the area of 25%, mainly due to differences in the casting methods and the standardisation of the data to similar lung capacities. Sauret et al. (2002) calculated the ratio to be 3.1 at the first 9 generations of a lung cast. Analysis of the Lovelace data [Raabe et al. (1976)] by Kitaoka's group in 1999 provided an almost Gaussian distribution of the ratio with a mean value of 2.8 and STD equal to 1, when a study by Tawhai et al. (2004) determined the length to be 3.04 times higher than the diameter, with a STD of 2.2.

35

All researchers indicated that there is a positive correlation between length and diameter which is steady throughout the lung, and as a rule of thumb their ratio is considered to be about 3.

In order to find the relationship of the airway diameters with respect to their generation, Weibel (1963) plotted the mean airway diameters against their generation number for the first 10 generations of a lung cast and came up with the following equation

$$d_j = d_o 2^{-\frac{J}{3}} \quad \text{(2.1)}$$

where d_j is the mean diameter in generation j and d_o is the diameter of the trachea. The validity of this equation was confirmed by Horsfield and Cumming (1967) who used the principle of minimal work to derive the optimal ratio

$$\frac{d_{J+1}}{d_J} = 0.794 \quad \text{(2.2)},$$

which is an expression equivalent to (2.1). Experimental measurements of the ratio of equation (2.2) down to airway diameters of 0.7mm generated a value of 0.76, further confirming the legitimacy of the theoretical result. Furthermore, Sauret et al. (2002) calculated this ratio to be 0.83 and 0.78 for the first 6 and 9 generations of a CT scan on a healthy volunteer and a lung cast respectively, while Tawhai et al. (2004) recently calculated it to be equal to 0.71 with STD 0.14. A different theoretical explanation as to why this value is the optimal for the human airway tree can also be based on fractal principles as described by West and Deering (1994).

An alternative way of measuring the same quantity was presented by Horsfield and Cumming (1968). The method they used involved the plotting of the order of bifurcation u against the experimentally found mean log d(u), d(u) being the airway diameter at order of branching u. After splitting the resulting graph into 3 discrete regions, they found that the relationship connecting order and diameter is given by the equation

$$d(u) = ab^u \quad \text{(2.3)},$$

where a and b are constants defined according to the order of branching. For orders of branching 1-6, a=0.676 and b=1.175. For u in the range 7-16, a=1.340 and b=1.062. Finally, for all the rest orders (17-25, which is the trachea), a=0.330 and b=1.161. Investigation of the same equation by Schmidt et al. (2004) turned out equivalent results.

In order to evaluate the asymmetry of the bronchial tree, the most commonly used indicators are either the secondary-to-primary daughter ratio or the bifurcation exponent n that determines the relation of parent and daughter branches according to the equation

$$ d_p^n = d_1^n + d_2^n \quad \text{(2.4)}, $$

where d_p denotes the diameter of the parent, d_1 and d_2 the diameter of the daughters. Equation (2.4) is valid only in systems where the conservation of flow is applicable, as the human respiratory tract is considered to be. Several authors calculated the ratio secondary-to-primary to be in the area of 0.86 [Weibel (1963), Phalen et al. (1978), Sauret et al. (2002), Tawhai et al. (2004)]. On the basis of the minimum energy loss principle, the value of n in equation (2.4) is determined by Horsfield and Thurlbeck (1981b) to be between 2.4 and 2.9 for the airways of four mammalian species. Kitaoka et al. (1999), using the same data as stated previously, calculated n=2.8 in the human lung where Schmidt et al. (2004) found the bifurcation exponent to be 2.475 for airways of the first 9 generations.

Finally, it is sometimes necessary to calculate the total path length from the trachea to the alveolated regions of the lung. Horsfield and Cumming (1968) estimated this length to be in the range from 7.5cm to 21.5cm, with a median of 12.5cm. Fleming et al. (1995) using modified Weibel data, calculated a total path length from the hilum to the acini between 5.5cm and 13.6cm.

Branching And Planar Angles

In order for the orientation of the tubes of the airway tree to be completely defined in all three dimensions, the angular information of the branching and the planarity of the airways are required. However, angular data and the relationships concerning them are scarcer in the literature than length and diameter data, mostly because of the difficulty involved in the process of measuring angles on lung casts. Especially

concerning the planarity of bifurcation, data have only become available after the introduction of medical imaging for measurement purposes.

The branching angle is defined as the angle formed between the extension of the skeleton of the mother airway and the skeleton of each of the daughters and it has been the angular characteristic most researched in the past (Figure 2.6). Horsfield and Cumming (1967), again using the principle of minimal work for the minimization of airflow resistances in the airway tree, calculated the optimal value for this angle to be 37° 28'. Experimentation on a lung cast by the same author and by Horsfield et al. (1971) showed that the mean branching angles varied between 30° and 43° for airways with diameters larger than 1mm. Later, Yeh and Schum (1980), after analyzing the data extracted by Raabe et al. (1976), revealed a range between 18° in generation 5 to 51° in generation 15, with a mean angle of 32°. The mean value observed by Phalen et al. (1985) was 43° with a minimum value of 28° in generation 3 and a maximum at 54° in generation 9. Finally, Sauret et al. (2002), after measurements on the CT data of a volunteer and a cast found a mean branching angle of 41° with a variation of 12° to 78°, while the estimated value of the same quantity by Tawhai et al. (2004) was 36.11^{o} with a STD of 20.85^{o}.

In an effort to study the branching angle with respect to the asymmetry displayed by the airway tree of 4 mammalian species, Phillips and Kaye (1997) introduced two complementary angular parameters. These are the angular asymmetry, namely the difference between branching angles, and the total branching angle, defined as the total bifurcation angle between the daughters. The main conclusions they reached, with respect to branching angle analyses are:

i) The branching angle of the primary daughter is almost always smaller than that of the secondary.

ii) Branching angles tend to decrease as airways diameters decrease.

A different approach was followed by Kamiya et al. (1974) who tried to produce relationships between branching angles and airway diameters. Based on fluid dynamics principles, they derived the equation

$$\frac{d_{O}^{2}}{\sin(\theta_{1}+\theta_{2})} = \frac{d_{1}^{2}}{\sin\theta_{1}} = \frac{d_{2}^{2}}{\sin\theta_{2}} \quad (2.5),$$

38

where d_0, d_1 and d_2 are the diameters of the mother and the two daughters respectively and θ_1 and θ_2 are the daughters' branching angles. According to Kitaoka et al. (1999), Thurlbeck and Horsfield's (1980) results display a tendency similar to that predicted by equation (2.5), which confirms its validity for the human lung.
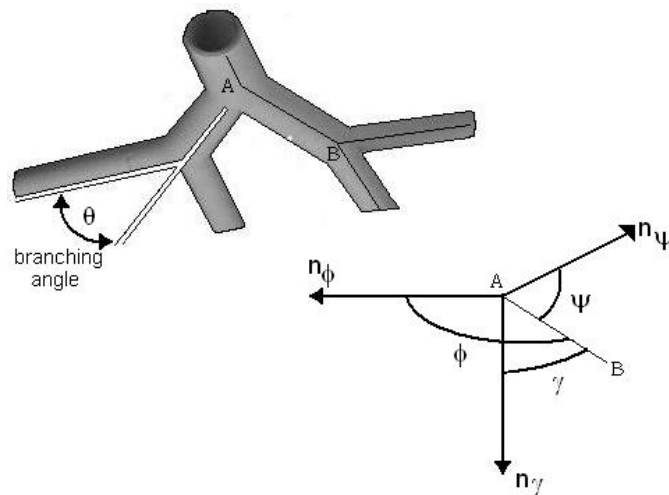
Figure 2-6: Definition of the orientation in space of an airway, described by the gravity, the coronal and the sagital angles, denoted with the symbols γ, φ and ψ respectively. The middle line of the airway starts at A and ends at B. The branching angle of a different path of the tree is also shown, the angle indicated by the symbol θ.

Other than branching, the most analysed angle in the literature is the gravity angle **γ**, defined as the angle between the tube and the direction of the force of gravity which is denoted by the normal vector $\mathbf{n_\gamma}$. It is clear that this set of information alone cannot illustrate the airway tree spatial distribution. For the morphometry of the airway tree to become apparent in 3D two more angular parameters are necessary, the coronal angle and the sagital angle, termed **φ** and **ψ** respectively in the image of Figure 2-6. These two angles display the displacement of the airway with respect to two normal vectors $\mathbf{n_\varphi}$ and $\mathbf{n_\psi}$ that point to directions perpendicular to that of $\mathbf{n_\gamma}$. These angles were thoroughly investigated by Sauret et al. (2002). The same author also examined the rotation angle between consecutive bifurcation planes, also known as planar angles. These were found to have a mean value of 79°,

confirming visual observations on lung casts and verifying the validity of the assumption of several modelling efforts [Martonen et al. (1995), Kitaoka et al. (1999)] that suggested values close to 90°. Tawhai et al. (2004) further corroborate this result calculating the rotation angle to be near 76° with a STD of 45°.

2.5.5 The Human Pulmonary Acinus

The information on the acinar region are not as detailed in the literature as on the conducting airways. Several morphometric studies of the pulmonary acinar structures have been carried out, either by making serial histological exams [Hansen and Ampaya (1975), Hansen et al. (1975)] or by cast observations. The latter method was used by Boyden (1971), who produced extensive drawings of an acinar wax cast of a six and a half year old male. Haefeli-Bleuer and Weibel (1988) provide the most extensive information on the geometry and morphometry of the intra acinar passageways. A structural study of the respiratory acinus was also conducted by Schreider and Raabe (1981). A human acinus photograph is displayed in Figure 2-7.
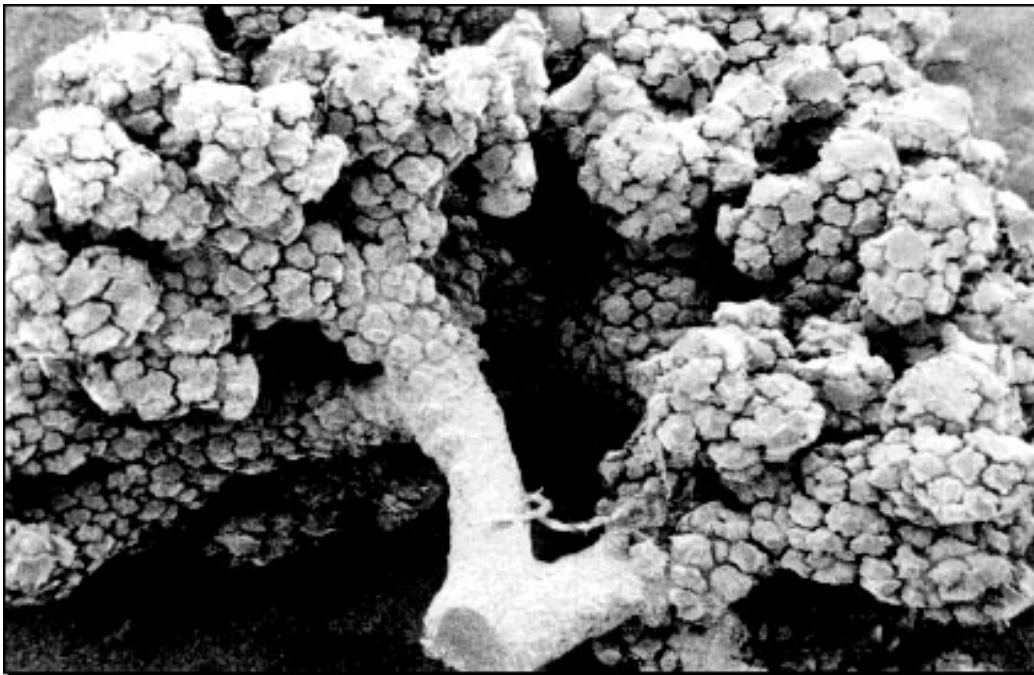
Figure 2-7: Photograph of the human pulmonary acinus. (Image obtained from the UCDAVIS, University of California internet site, web address http://trc.ucdavis.edu/mjguinan/apc100/modules/Respiratory/lung/lung6/lung.html. Reprinted with permission. © 2008, The Regents of the University of California, Davis campus.)

Hansen and Ampaya (1975) found an average acinar volume of 182mm^3, a number confirmed by Haefeli-Bleuer and Weibel (1988) who described it to range between 51 and 459mm^3, with a mean value of 186mm^3 and a STD of 79mm^3, the volume distributed in the manner of a slightly skewed log-normal distribution. These figures disagree with the results obtained by Boyden (1971), who estimated the volume to be only in the area of 15.6mm^3. Although it was previously suggested that the intra-acinar branching is dichotomous, trichotomous or even polychotomous, later results state that the predominant branching pattern is binary, a result that agrees with Weibel (1963). Furthermore, assuming a total acinar volume at total lung capacity of 6 litres and a mean acinar volume of 187mm^3, Haefeli-Bleuer and Weibel (1988) estimated that the human lung should contain a number of acini in the range of 26000-32000.

According to the same authors, the most important parameter is the mean acinar path length, which is defined as the mean distance along the acinar airways from the first respiratory bronchiole to the end of the alveolar sacs. This was found vary between 5.5mm and 13.5mm, with a mean at 8.25mm and a STD of 1.4mm. Hansen and Ampaya (1975) further verify these results, calculating the mean path length to be 6-7mm long. The discrepancy is considered to exist mainly due to different methods of casting.

Finally the acinar airway diameters were shown not to follow the same rules as the bronchi and bronchioles of the airway tree. Although the bronchi diameter decreases with generation number, the acinar pathway diameter remains virtually unchanged almost down to the alveolar sacs. This was justified by the fact that the diffusion function performed in this area of the lung favour high cross-sectional areas. It has to be mentioned that the shapes and sizes of the acini vary greatly, a point agreed upon by all authors.

2.6 Conclusion

In this chapter the anatomic, morphologic and morphometric information of the human respiratory tract were investigated, with special care being given to the

airway tree. The main functions of the lungs were also discussed and the main threats and protective mechanisms examined. Both the intra- and inter-subject variability that dominate the human lungs were also described based on observations made on lung casts or from medical imaging. Finally, certain relationships between specific morphometric data were illustrated and their accuracy debated.

All the principles of the human lung anatomy presented in this chapter have been used in the past for the creation of various mathematical analyses that allowed the generation of a range of models referring to both lung morphology and function. The next chapter will be concerned with the presentation of various anatomical models that were created in order to accurately reproduce the human lung. Medical imaging methods prevalent in the generation of such models will firstly be presented. The fluid dynamic principles that dominate this part of the human body that led to those models will then be investigated. Finally, different aerosol deposition mechanisms and models will be examined in order to show why further research is required for the improvement of the 3D realism of the pulmonary anatomy.

Chapter 3

Visualisation, models and mathematics of the human lungs

3.1 Introduction

In the previous chapter the anatomical, morphological and morphometric aspects of the lung structure have been investigated. This chapter is more concerned with the theory underlying the efforts regarding the development of a complete mathematical description of the human lung and its workings, primarily based on the biological information made available earlier. At first, the different imaging modalities currently used to visualise the lungs and, more specifically, the respiratory tract, either *in-* or *ex-vivo,* are examined. Following that, the most important anatomical models of the human airway tree, many of which use medical imaging techniques, are studied. Furthermore, the fluid dynamic principles on which some of the models are founded, as already mentioned in Chapter 2, are explained. Finally, the ways these principles affect the deposition of particles in the respiratory tract are discussed. This discussion will include both the physics of particle retention in the pulmonary airway tree and the prediction models of anatomical distribution of particles within the human lung.

3.2 Imaging Of The Lungs And Their Components

Several imaging methods have been used in order to view the lung and its components *in-vivo* for both clinical and research purposes. The medical imaging techniques employed for such purposes can be divided into radiological and magnetic.

3.2.1 Imaging The Lungs Using Radiological Methods

X-ray Imaging

X-rays have been the foremost medical imaging tool ever since their inception in 1895. The general principle of this imaging modality is the bombardment of the body with X-radiation and the capturing of the distribution of the photons emitted as the radiation exits the object volume.

There are two mechanisms for producing such low energy X-radiation. The first is by decelerating a free electron through its interaction with the electrons orbiting an atom. This is the dominant method for X-ray production and is referred to as braking radiation. Through this method a wide spectrum of X-ray energies can be produced as the energy of the final beam is dependent on the original electron speed.

X-rays can also be produced by the ejection of an electron from an atom after the collision with a free, high-energy electron. X-rays are emitted from the atomic structure as the atom reshuffles its electrons in order to regain stability. This process is known as characteristic X-ray emission because the energy of the resulting radiation depends on the elemental nature of the target atom.

In a modern high-resolution X-ray source, electrons are emitted from a cathode and are then accelerated to speeds near the speed of light. The electrons are then set on a collision course with a metallic surface and are concentrated on a single spot with the help of a magnetic lens. The final image resolution depends on the quality of the lens focusing properties. The electron energy is reduced through the interaction of the electrons with the atoms of the target surface. It has to be noted that the vast majority of the energy consumed during this process is released with the form of heat whereas only a small percentage of the interactions produces X-ray beams.

The beams are then directed toward a target volume, i.e. the human body in medical imaging applications. As the radiation passes through the body

created with nitro PDF professional
download the free trial online at nitropdf.com/professional

tissues, it faces different attenuations according to the tissue types. For instance, bone attenuates X-rays almost three times as much as flesh and blood. In the case of the lungs, there is strong contrast between the ribcage bones and the nearly zero attenuation of the lung air. Therefore, problematic regions will be depicted on the X-ray film as high-contrast areas.

There are some inherent problems to the use of X-ray imaging for the *in-vivo* visualisation of the inner structures of the human lung, such as the airway tree. The most important of these is that the two-dimensional nature of this technique leads to the loss of all depth information as, even with the use of X-ray stereo pairs, the structural overlap of the highly complex airway tree hinders the assessment of the three-dimensional tree configuration. For both these reasons, single-projection X-ray imaging is no longer used for the depiction of the human airway tree.

X-ray Computed Tomography (CT)

To overcome the limitations imposed by single-projection X-ray imaging, a tomographic technique involving X-rays was developed by 1972 by G. N. Hounsfield, a scientist at EMI LTD, England, and separately by A. M. Cormack of Tufts University in the USA, which was originally named computerised axial transverse scanning. This process came to be known as X-ray Computed Tomography (CT) and was based on the mathematical framework described during the 2nd decade of the 20th century by the Austrian mathematician J. Radon who, while working on gravitational field theory, proved that a two- or three-dimensional image could be reproduced from an infinite set of projections.

Computed Tomography is the process of imaging an object from many different directions using penetrating radiation such as X-rays and then utilising a computer in order to calculate the interior structure of the object using the projected images. This method therefore allows for accurate sizes, shapes and locations of the internal configuration of a target volume to be captured and examined. Today, the predominant methods used are variations of High Resolution Computed Tomography (HRCT) which was devised in the

created with
nitro^PDF professional
download the free trial online at nitropdf.com/professional

early 1980s and incorporates a higher resolution and sensitivity compared to the original device.

During image acquisition by a CT scanner, the X-ray tube, in a definite pattern of movement which is usually either circular or spiral, permits the radiation rays to sweep in many directions through a cross-section of the human body. The X-ray beams exiting the target are captured by sensitive crystal detectors and a set of consecutive, high-resolution digital radiographs are acquired at regular intervals by storing the intensity of the beams in rectangular matrices. Each matrix element represents the attenuation coefficient of the tissue at each spatial location within the body volume. The acquisition process can be observed in the graph of Figure 3-1.
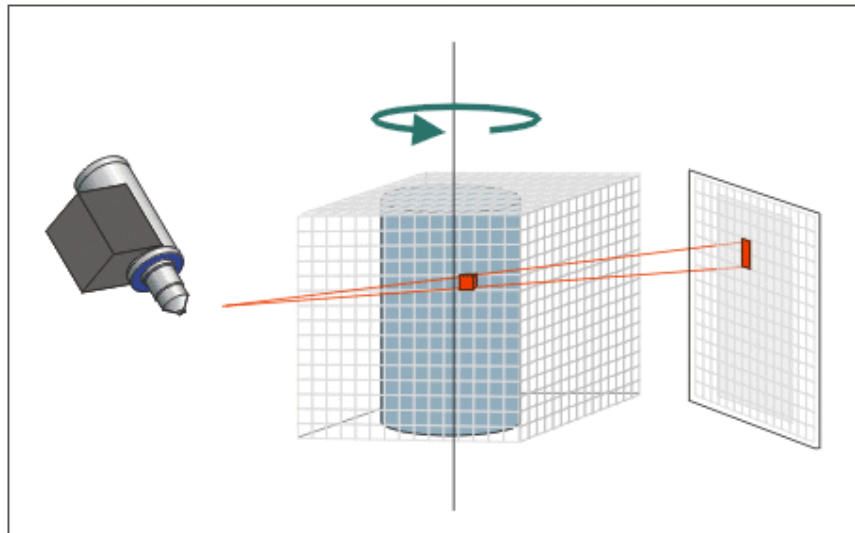
Figure 3-1: Image acquisition process of a CT scanner.

After the radiographs are collected, each projected image must undergo geometric and shading correction in order to remove spatial and intensity non-linearities introduced by the device. The output of the process is reconstructed as a set of parallel planar images of the scanned volume with a specific and steady spatial resolution with values in the region of 1 millimetre. The three-dimensional image of the internal structure can now be

reconstructed by stacking the slices on top of each other and then applying standard interpolation algorithms to fill in the gaps between the slices.

HRCT scanning has several desirable properties. First of all there is no correlation between image elements during reconstruction, thus ensuring that unbiased information is captured in the planar images generated. Furthermore, very good resolution can be achieved, limited only by the apparatus' data storing capabilities and the radiation dosage limitations involved in radiological medical applications. Additionally, the application of X-ray CT principles are being used in the radio-therapy of cancerous regions of the human body. However, CT's most important characteristic is its sensitivity to different tissue types, which makes this medical imaging modality extremely useful for diagnostic purposes.

Especially for the lung, HRCT has been shown to be very useful for the evaluation of airway hyper-responsiveness and for the assessment of airway abnormalities in patients with bronchopulmonary obstruction diseases such as asthma [Brown and Zerhouni (1998)]. HRCT can also be used to supply clear anatomical details of the lung and its substructures. CT images provide the 3D limits of the human lung and make the visualisation of lobar fissures possible, though the lung segment contours cannot be depicted since pulmonary segments are not enclosed in any enveloping tissue. Most importantly, the airway tree, down to an airway diameter of 1 to 2 mm, can be defined and imaged as available devices and techniques make the segmentation of individual airways down to generation 8 feasible [Sauret et al. (1999), Tawhai et al. (2000), Schmidt et al (2004)]. If this is combined with precise aerosol deposition models, the targeted inhalation therapy of many lung afflictions becomes a viable treatment option.

The achievement of even higher resolution for the imaging of the airway tree would be possible only with the intensification of the penetrating radiation dosage imposed on the subject scanned, a solution clearly unacceptable for modern medical practices. In addition, the process would also involve longer acquisition times, rendering the captured images prone to motion artefacts.

Furthermore, two-dimensional analyses of airways are limited to the airways that are reasonably close to a perpendicular orientation in the scan plane. Finally, the acquisition and reconstruction process is not only computationally expensive but also very demanding in storage capacities. Still, HRCT is currently the most popular medical imaging modality for applications concerning the human airway tree due to the level of detail it can attain and its relatively simple application.

Radionuclide Imaging

Single Photon Emission Computed Tomography (SPECT) is an alternate tomographic medical imaging modality that is used to acquire information on the concentration of radionuclides inserted to the human body. SPECT dates back to the early 1960's, when the idea of transverse section tomography was introduced by D.E. Kuhl and R.Q. Edwards. There are two major differences between SPECT and X-ray imaging. The first is that the emission sources are inside the body cavity and bombard the whole volume of the human organism from the inside out, although specific organs are targeted. The second is that in X-ray CT the quantity measured is the attenuation whereas in SPECT it is the actual transmission source.

As in CT, SPECT imaging involves the rotation of a photon detector around the body to acquire multiple projection data. Before this becomes possible, however, certain preparations must be made. The initial step is the selection of the proper pharmaceutical substance, depending on the organ that is to be studied. The pharmaceutical is then labelled with a suitable gamma-emitting radionuclide in such a way that its physiological properties are not affected. The imaging process can only begin after the radio-pharmaceutical is injected or otherwise introduced to the human body and an appropriate amount of time for it to be retained by the organ has been allowed for. The most commonly used pharmaceutical for diagnostic lung studies is albumin microspheres labelled with technetium-99m (Tc-99m).
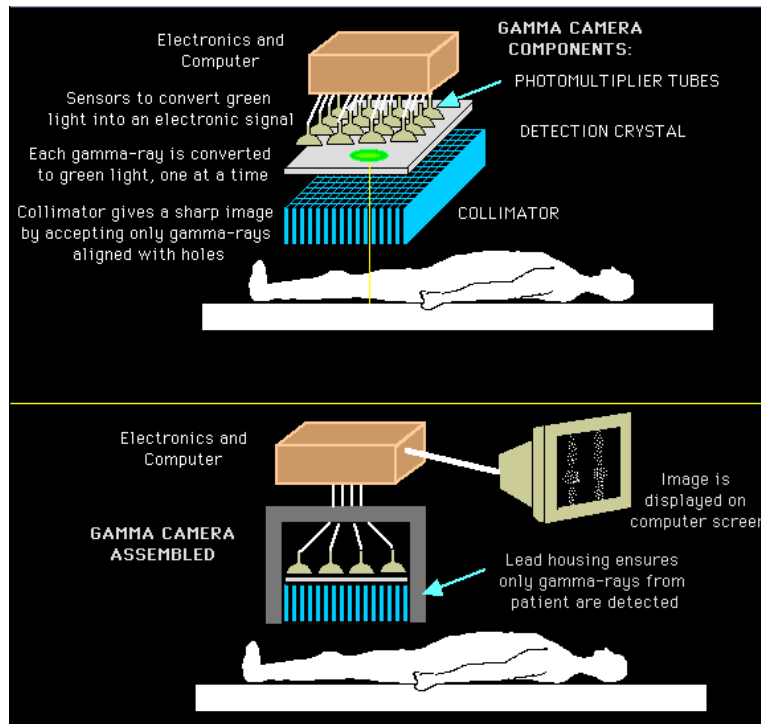
Figure 3-2: The gamma-camera standard configuration.

As mentioned above, the type of radiation used is gamma emissions. This form of radiation accompanies charged particle emission in radioactive decay. The daughter nucleus is still in a high energy state and it regains stability with the emission of gamma rays, which are actually photons of electromagnetic radiation.

Gamma radiation can be captured with the use of a gamma camera, a device that can produce images of the distribution of the gamma-emitting radio-pharmaceutical. A schematic of a gamma-camera typical configuration is displayed in Figure 3-2. The first such device was developed in 1957 by H. Anger and his original design is still widely used today. The system accumulates counts of gamma-photons that are absorbed by a large crystal in the camera, usually a large flat crystal of sodium iodine with thalium doping placed in a light-sealed housing. When a photon collides on the crystal, a small flash is produced. An array of photo-multiplier tubes arranged in a matrix formation behind the crystal detects the fluorescent flashes and a computer sums the counts. The computer in turn reproduces a two-

dimensional image of the specific projection of the body volume under investigation. Tomographic reconstruction can finally be applied to the multiple projections to yield a 3D dataset.

Spatial information about the gamma emissions from an imaging subject is done by correlating the detected photons with their point of origin. This is accomplished by filtering the photons radiated with the help of a thick sheet of lead, 1-3 inches thick, with thousands of adjacent holes through it, called a collimator. The collimator form is rather important for the device performance since it is subject to a trade-off between camera sensitivity, image resolution and human subject exposure to radiation.

The diagnostic function of SPECT imaging protocols is based on the fact that there are differences in the radio-pharmaceutical uptake between the healthy and the diseased organ. For example, in patients with asthma or other bronchopulmonary obstruction conditions, a smaller number of counts in the afflicted areas should be expected. Furthermore, the pharmacokinetic properties of the human body can be examined and studied. For example, in lung imaging, aerosol deposition can be investigated with the help of the images produced with SPECT.

However, there are certain undesirable properties associated with SPECT imaging. Firstly, only very low resolution is achievable, in the order of 1cm linear dimension. The randomness of radioactivity and attenuation affect the precision of the measurements. There are also multiple scattering effects that degrade the quality and contrast of the images. Furthermore, random noise is amplified during reconstruction and must be filtered out. Finally, the sensitivity decreases with increasing count rates because of the digital nature of the acquisition equipment, resulting in the underestimation of the count rate. While most of the above issues can be compensated using filtering algorithms, the low resolution of SPECT makes it inappropriate for detailed anatomical studies of the airway tree, though it can be used to provide the foundation of some generalistic lung models and verify the outcomes of other modelling efforts. Consequently, SPECT imaging studies are used to asses the

function rather than the structure of the body organs. For that reason, SPECT is mostly used in combination with other imaging modalities to provide medical practitioners with additional information on both the anatomy and metabolic levels.

A different approach to the use of radionuclides for the purpose of imaging the human body is Positron Emission Tomography (PET). PET imaging uses principles similar to SPECT, since a radiopharmaceutical needs to be introduced to the organ under examination before the radiation concentration at specific areas can be measured. However, instead of gamma radiation, isotopes with short half-life periods that emit positrons are utilised for this method. After travelling up to a few millimetres the positron encounters and annihilates with an electron, producing a pair of annihilation photons moving in nearly opposite directions. These are detected when they reach a scintillator material in the scanning device, creating a burst of light which is detected by photomultiplier tubes. The technique depends on simultaneous or coincident detection of the pair of photons. Photons which do not arrive in pairs are ignored.

Because of the paired arrival of photons in the detection device, almost the exact location in the body where the positron collision took place can be calculated. For that reason, PET scanners do not require the use of collimators for the acquisition of correct spatial information on the positron emissions while they can achieve higher resolution than SPECT protocols. Furthermore, modern PET scanners include integrated high-end multi-detector-row CT scanners to their apparatus, so that both examinations can be performed simultaneously. Nevertheless, PET imaging is a rather expensive procedure. This is partly due to the fact that the radio-isotopes utilised need to be produced in a cyclotron which is not too far away in delivery-time to the PET scanner. Finally, when applied to the lung, PET cannot reach the quality of spatial resolution predicted by theory because of the longer paths travelled by the positrons before their annihilation.

3.2.2 Imaging The Lungs Using Magnetic Methods

Magnetic Resonance Imaging

Magnetic Resonance Imaging (MRI), formerly referred to as Nuclear Magnetic Resonance Imaging (NMRI), is a method used to visualize the internal structure of living organisms as well as to detect the composition of geological formations without the use of harmful ionizing radiation. Its foundations lie on the principles of the magnetic resonance phenomenon, which was discovered independently by F. Bloch and E. Purcell in 1946, a discovery for which they were awarded the Nobel Prize in 1952. The relevant techniques applicable to the imaging of the human body were only developed in the late '70s. The catalyst for this development was the demonstration by R.V. Damadian (1971) that the nuclear magnetic relaxation times of tissues and tumours differ. In the last two decades MRI has become an extremely important diagnostic tool for clinicians.

MRI is based on the absorption and emission of energy in the radio-frequency (RF) range of the electro-magnetic spectrum. It gets around limitations imposed by the natural fact that it is not possible to visualize objects smaller than the wavelength of the energy being used to image by producing pictures of the spatial variation in the phase and frequency of the RF energy being absorbed and emitted from the object under inspection. Only nuclei with an odd number of protons or neutrons are studied in MRI. Since the human body contains a high number of hydrogen atoms (63% of the atoms in the human body), medical MRI most frequently relies on the relaxation properties of the hydrogen nuclei.

When placed within a uniform magnetic field, denoted B_o, the protons of the hydrogen nuclei, which have been in random alignments within their molecular environments, will align themselves in a parallel or anti-parallel fashion to the external magnetic field depending on their spin. Once uniformly aligned, the protons begin to "precess", i.e. to rotate about the axis of the B_o vector with a frequency called the Larmor frequency, given by the relationship

$$F_O = \gamma \cdot B_O \quad (3.1),$$

where F_o is the Larmor frequency in Hz, γ is the gyro-magnetic ratio, a material-dependent constant, and B_o is the magnetic field strength in Tesla (T). Furthermore, since the parallel alignment is associated with lower energy states than the anti-parallel one, a higher number of protons will end up in parallel with B_o, thus creating a net magnetic moment aligned with, or longitudinal to, B_o.

A RF pulse is then emitted by a coil integrated to the MRI scanner. If the RF pulse is chosen correctly it matches the Larmor frequency, causing the resonance of the precession rotation to occur. For that reason energy will be transferred to the protons that will disturb the nuclei equilibrium, resulting in the anti-parallel alignment of more protons. This has as a consequence the reduction of the longitudinal magnetisation and, since the protons spin in phase during precession, the creation of transverse magnetisation.

When the RF pulse is terminated, the nuclei start to move back to their equilibrium state. The time for the longitudinal magnetisation vector to be restored to its pre-RF signal stable condition is called the longitudinal relaxation time and is termed T1. Furthermore, the protons continue to precess but slowly turn out of phase thus reducing the transverse magnetisation. The energy emitted by this process is picked up by a receiving coil, usually the coil producing the RF signal, and is converted to an electrical signal called the Free Induction Decay (FID). The rate of decay of the FID is described by the time constant T2.

The combination of T1 and T2 represents the molecular structure in which they are found. T2 is always smaller than T1, usually in the order of 100ms while T1 is closer to 1s. The images are obtained by creating contrasts using a selection of image acquisition parameters that weight signals by T1, T2 or no relaxation time, depending on the application and the pathology of the region under investigation. Water and other liquids have long T1 and T2 while fats have shorter relaxation times. Generally, the relaxation times depend on the

water concentration of the examined tissue while T1 also depends on the strength of the external magnetic field. It becomes apparent that tissue contrast depends on the differences in T1 and T2.

The images displayed by the MRI process are produced in much the same way as in CT scans. However, MRI generally allows for the completely flexible orientation of the images. All spatial encoding is obtained by applying magnetic field gradients which encode position within the phase of the signal. A matrix of spatially encoded phases is acquired, filled with data representing the spatial frequencies of the imaged object, which can be visualized after the application of mathematical transformations. These transformations are well established variations of the Fourier Transform, like the Discrete Fourier Transform or the K Transform.

It is clear that there are several differences between X-ray CT and MRI examination protocols, the most important of which is the absence of ionising radiation from MRI scans, a fact that makes this technique appropriate for use in sensitive population groups such as pregnant women. Furthermore, though CT provides very good spatial resolution it can rarely be used to discriminate between different soft tissues. This causes certain difficulties in the diagnosis of the existence of tumour lesions, which cannot be accurate until the disparities had grown pronounced. MRI on the other hand is very tissue sensitive, offering comparable spatial resolutions along with enhanced contrast resolutions between different tissues. The additional capability of MRI to acquire projections of the probed area from many different angles constitutes this modality preferable in applications like tumour detection, where soft tissues are required to be scanned with a high degree of sensitivity.

MR volume imaging using T1-weighed procedures can also be employed to give the outline of the lung in 3D [Fleming et al. (1996)]. MR imaging of the lung, however, is severely limited due to the low proton density of the air contained in the tracheobronchial tree, the cardiac and respiratory motion and other air-to-tissue interface effects. Even though some of the problems

can be overcome by techniques such as cardiac and respiratory gating, the extent of the airway tree that can be visualised using this modality in stand-alone is very inadequate for both diagnostic and research purposes.

To overcome this issue, the introduction of contrast agents to the respiratory tract in the form of hyperpolarized noble gasses, such as Helium-3 (He-3) or Xenon-129 (Xe-129), was proposed [Albert et al. (1994), Kauczor et al. (1998)]. In these examinations the large non-equilibrium magnetisation of the nuclei of the hyperpolarized gasses provides the contrast instead of the hydrogen atoms in normal MRI protocols. Xe-129 is a non-radioactive noble gas, highly soluble to water and fatty tissues. This property makes it appropriate for perfusion studies, although its anaesthetic effects on the human organism restrict the variety of potential applications. On the other hand, for ventilation studies He-3 is the preferable gas since it is also non-radioactive but it is insoluble to liquids like water and blood. Furthermore, there are no adverse effects associated with its use as is revealed by its use in large concentrations (20% O_2, 80% He) in deep-sea diving. The low density of the gas that causes a low signal is compensated by its high spin density.

After hyperpolarized He-3 gas is inhaled, the airways can be visualized with strong intensity. Nevertheless, as pointed out by Brown and Zerhouni (1998), the technique provides limited enhancement of individual airways, in direct contrast with the resolution provided by HRCT. Another limitation of He-3 MRI is that He-3 is not a widely available element and it is rather expensive for clinical applications due to the sophistication of the hyper-polarization methods, while helium is rare even in its natural form because it is the product of tritium decay. Finally, MRI of the lungs using noble gasses is shown to be highly susceptible to motion artefacts.

Still, this technique shows great promise and much research is being conducted on the field. It is expected that in the near future the spatial and temporal resolution (the latter through dynamic imaging) will match its contrast resolution quality, overall surpassing the one available in HRCT. Moreover, its cross-sectional imaging and post-processing capabilities are

additional advantages, along with the lack of ionizing radiation. Furthermore, MRI also helps provide further insights into the pathophysiology of breathing. Finally, as shown in later studies [Waters et al. (2006)], since the apparent diffusion coefficient of He-3 in the lungs correlates to the peripheral airspace sizes, alterations in the lung microstructure can be detected, supplying clinicians with valuable information for diagnosing pulmonary disease.

3.3   Models Of The Human Respiratory Tract

As mentioned earlier, accurate mathematical descriptions of the human pulmonary airway tree can be broadly used in many medical applications. In conjunction with particle deposition studies they can be used to achieve better cost/effectiveness ratios of treatments based on aerosolised inhalable medicine, or they can be used to predict the harmful effects of pollutants in particle form on the human organism. Furthermore, a mathematical description of the morphometric properties of the bronchial tree can be combined with medical image analysis techniques to generate better diagnostic methods for lung disorders. For these reasons, various anatomical models were derived in an attempt to accurately illustrate the morphometry and morphology of the airway tree and the pulmonary acinus.

Two general approaches have been taken for the creation of these models: Either a deterministic approach (also referred to as descriptive), where the specific location of each element of the tree is explicitly defined, or a stochastic one, where the tree morphology is described in a statistical fashion. The latest developments in the medical imaging field along with the increase in the availability of computer power has resulted in the former approach being more popular in the last decade within this field of research.

3.3.1 Deterministic Bronchial Tree Models

The first modelling attempt concerning the airway tree was the product of a detailed study of 5 human resin and silicon rubber lung casts. The airway

features of these casts were manually measured by Weibel (1963) and the model produced based on that data was named "model A". It is also referred to as "typical path lung model" [Phalen et al. (1978), Yeh and Schum (1980)] and, though it is the simplest model available in the literature, it provided the basis for many subsequent efforts. The main attributes of this model can be observed in Figure 3-3.
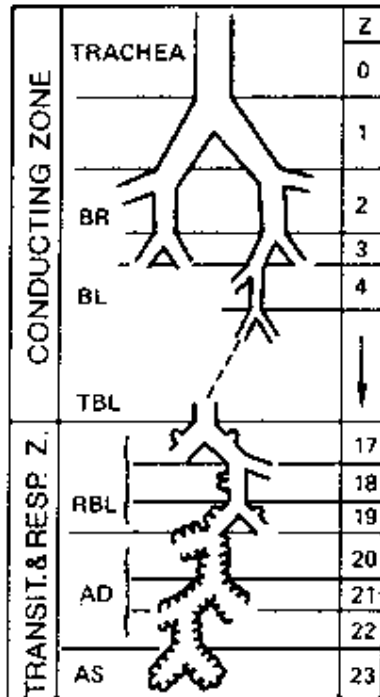
Figure 3-3: Idealisation of the human airways according to Weibel's model A. Z= airway generation, BR= Bronchi, BL= Bronchioles, TBL= Terminal Bronchioles, RBL= Respiratory Bronchioles, AD= Alveolar Ducts, AS= Alveolar Sacs.

According to this method, the airways are assumed to be a sequence of straight cylindrical tubes following a regular dichotomous branching pattern. The airways are measured and grouped into generations, each generation containing 2^j total number of airways and the system consists of 23 generations starting from the trachea, which is given generation number j=0. Every airway of each generation has the same dimensions, obtained from the statistical treatment of the experimental lung-cast data. Only lengths and diameters are modelled since angular data were not gathered due to the practical difficulties of making such measurements manually. The first 16 generations make up the conducting airway network ending in the terminal bronchioles, with the next 3 generations constituting the respiratory bronchioles, in which the degree of alveolation steadily increases. The true

57

respiratory zone consists of 3 generations of alveolar ducts and 1 of alveolar sacs.

It is obvious that this idealised, dichotomously branching airway system is an oversimplification of a particularly complex structure. Its main drawbacks are the lack of asymmetry evident in the lung, the inadequate description of intra-subject variability and the model's two-dimensional character, since no information of how the tree fills the 3D space are provided. However, because of its simplicity, it provided the foundation for the derivation of several other more complex models, such as the trumpet model [Taulbee and Yu (1975), Yu and Diu (1982), Egan and Nixon (1985)], the model developed by Yeh and Schum (1980), the stochastic model of Soong et al. (1979), the conceptual model [Fleming et al. (1995)] and the three-dimensional model described by Martonen et al. (1995).

The trumpet model, depicted simply as a trumpet shape, is a spatially continuous mathematical model consisting of partial differential equations that describe gas concentration in position and time in an effort to represent two fundamental physiologic principles. The first is that the respiratory tract is a tree structure that consists of 23 generations, begins at the mouth and ends at the alveolar sacs. The second is that gas transport is gradually replaced by diffusion processes the deeper the gas penetrates into the lung. According to this model, there is no discrete interface between these two forms of flux such as dead space or alveolar gas. The airway characteristic quantified by the trumpet shape is the cross-sectional area of the airways in each generation against the path-length from the trachea. The narrow neck of the trumpet represents the upper airways and the succeeding airway generations are represented by the widening trumpet shape. Since the gas velocity in a tubular system is governed by the cross-sectional area of the chosen position within the system structure, it follows that higher velocities will be evident at the narrower parts of the trumpet while the bell-end will display diffusive properties.

Yeh and Schum (1980), in an attempt to describe intra-subject variability with a model as much 3D realistic as possible, used the same symmetric dichotomous idea as Weibel, utilizing at the same time the dataset provided by Raabe et al. (1976), also known as the Lovelace data. Taking advantage of the data formalisation proposed by Phalen et al. (1978), according to which each of the airways was uniquely identified and its geometric characteristics separately recorded, the authors introduced an airway model for each lobe in the lungs. All the available pathways were traced from the trachea down to each terminal bronchiole and the number of pathways terminating at various generations was counted to form a frequency distribution. From this distribution the median generation number could be obtained, along with the range of generations where pathways terminated within each lobe. Airway lengths and diameters were presented by log-normal probability density functions of which the mean or median values were found for the section of the lung involved. The model also included branching and gravity angles (see Chapter 2 for definition) for each generation up to generation 15, calculated as the average values of all branches of the same generation within the same lobe. After generation 15, gravity and branching angles were fixed to 60° and 45° respectively, due to the scarcity of available data. The average data of the airways are available for the whole lung and per lobe.

The conceptual model [Fleming et al. (1995)] has certain similarities to the above models since it also describes the airway volume with respect to their depth in their lung. The model was originally developed with the specific intention of it being immediately applied to image analysis as suggested by Perring et al (1994). The purpose was to develop a methodology for the derivation of aerosol deposition per generation with the help of the 3D spatial distribution of deposition measured using SPECT imaging. According to this model, the lung volume, obtained through imaging modalities such as MRI, is subdivided into 10 concentric hemispherical shells via a hemispherical transform performed on each lung shape, centred on the hilum. Each voxel is assigned a shell on the basis of its fractional distance from the hilum to the corresponding extrapolated point on the lung periphery. The data available from previous morphometric studies [Weibel (1991a)] are then used to define

the number of acini in each shell and to calculate typical airway paths, starting at the hilum and ending at an acinus somewhere within a shell. The typical paths are considered to extend radially and with no retraction toward their starting point while the acini are assumed to fill the remaining volume uniformly.

In its revised form [Fleming et al. (2004)] the model includes more precise assumptions on the location of the acini and other airways. At the same time, its validation became possible due to new studies. The model is referred to as conceptual because of the lack of information on the spatial location of the individual airways. A great advantage of defining the airway this way was that the model could be easily adapted to fit any probable lung shape, which is a fundamental requirement of any model used for SPECT data analysis, along with three-dimensionality. However, though the conceptual model has been demonstrated to produce satisfactory results when calculating deposition from 3D image data, it has certain weaknesses in its design. The conceptual model, its weaknesses and the proposed methods of overcoming them will be a matter of discussion for the next chapter.

Martonen et al. (1995) made the first effort, to our knowledge, to create a fully deterministic, three dimensional model of the airway tree structure. The dataset of airway geometry utilized was the one described by Soong et al. (1979), which in turn was based on the data derived by Weibel (1963). The average values of airway lengths and diameters for each generation are used to describe all airways within the specific generation. The airways are also considered to be a sequence of straight cylindrical tubes forming Y-shaped bifurcations. The bifurcation angle of all generations is fixed to 35°, a value close to the theoretical optimal value derived by Horsfield and Cumming (1967), while the angle between bifurcation planes, which is also necessary when describing three dimensional structures, is intuitively set to 90°. The resulting model has the two lungs symmetrical and overlapping, which is a highly unrealistic situation for any biological system. This is because of the unrestricted growth of the tree in 3D space. A new version of the model [Martonen et al. (2000)] uses a template simulating realistically the lung

shape to place constraints on the expansion of the tree. If the airway final position is calculated to be outside the simulated lung, the cylinder is reflected back inside the spaced defined by the template. Even though better assumptions on the branching angles are used, this approach doesn't solve the symmetry or the single-airway superposition problem. However, this might be unnecessary for certain applications. This is displayed by Schroeter et al. (2002) who used a similar approach for the purpose of analyzing SPECT images.

The real lung exhibits strong asymmetry between airways, which is a property not taken into consideration by the models presented above. Furthermore, though Weibel's "model A" (1963) is very influential, it overestimates the number of airways present in different lung locations, simultaneously ignoring the possible appearance of alveoli in early airway generations. For these reasons, the realistic description of the bronchial tree depends on the level of asymmetry introduced to its branching pattern. Horsfield et al. (1971) proposed a process of incorporating asymmetry to the branching structure. According to this method, airways may branch into daughter tubes of different orders. As mentioned in Section 2.5.4, the branches are identified in orders instead of generations, beginning with the ones distal to the trachea. However, since bronchi of the same order are assumed to have identical geometric characteristics, there is a general evenness displayed by the airways of each order, a property equally unrealistic to the branching symmetry. Weibel's asymmetric version of "model A", presented in 1991, doesn't resolve this issue.

A different type of model was proposed by Kitaoka et al. (1999), who used a deterministic algorithm to develop a 3D model of branching duct systems that can supply fluid to an evenly distributed volume or organ. There are two basic principles this approach is based on for the determination of airway sizes and spatial arrangements: The first states that the amount of fluid delivery through a branch is proportional to the volume of the region it supplies. The second considers the terminal branches to be homogeneously arranged within the confining space. These two principles signify the need for

effective and homogeneous fluid transportation within an organ. The asymmetry of the branching structure is ensured by the fact that, instead of statistics, fluid dynamics rules are employed to describe the relationships between the geometric properties of the airways. This becomes possible with the introduction of initial conditions that specify the outer boundary of the organ and the initial configuration of the tree-trunk. The first is given by a series of mathematical expressions that are combined to mimic a lung shape while the second condition is satisfied by data available on anatomical text-books. Nine basic and four supplementary rules, based on the above principles, are established for the generation of the tree. The model appears to be very close to a realistic description of the tracheobronchial tree in terms of total number of acini and airway volume generated. However, it is markedly more asymmetric than the human lungs and the algorithm is very sensitive to the selection of some parameters in addition to the initial conditions. It is also important to note that validation of the model was not available in the literature.

Tawhai et al. (2000), based on the fractal nature displayed by many biological structures [Weibel (1991b)], proposed the development of a different deterministic process. The main assumption made was that the conducting airways are an approximately space-filling structure, which implies the same uniform distribution of acini within the lung that many of the previous models suggested. Similar initial conditions to Kitaoka's diameter-flow algorithm have to be provided for this method to be functional: The beginning few generations of the tracheobronchial tree as well as the lung surface enveloping it. The former condition is satisfied by modifications on the work of Horsfield and Cumming (1968) while the latter is given by MRI scans.

The process can actually be described as a space division algorithm. The volume mesh representing the organ is first filled with a matrix of seed points, either uniformly or randomly spaced, which are then grouped together depending on the distances to the bronchi, and the bifurcation plane of each branching pair is calculated. This plane divides each group into two groups of usually unequal volume. The centre of mass of each of the new two

sets is determined and the parent branch is connected to these points through a straight line beginning at the end of the parent and ending on the center of mass. The daughters lie on these lines, with a length equal to 0.4 times the distance from the endpoint of the parent to the centre of mass. The process is repeated until a minimum length threshold is breached or the seed point number is too small. The results of this algorithm are shown to be able to relate the airways to the local lung geometry, which is a very desirable property. Furthermore, they compare well with some previous modeling efforts, especially with the data provided by Horsfield and Cumming (1968) and Phalen et al. (1978). However, the model lacks proper rules for the assignment of diameters to the generated airways. In addition, there are some discrepancies between experimental studies and this process on the matter of bifurcation plane angles. More importantly, the branching angles on this model are found to remain close to the theoretical optimum even at high generations, which is not true according to previous experimental data. Also, only limited validation of the model by comparison with the literature was available.

3.3.2 Stochastic Bronchial Tree Models

Stochastic approaches have been primarily used in an effort to model inter- and intra-subject variability. The first model that uses stochastic methods for the description of the tracheobronchial tree was presented by Soong et al. (1979) and it basically involves the rearrangement of the Weibel (1963) "model A". The airway tree model produced by Weibel was considered to be an average around which distributions of the geometric characteristics were derived from published morphometric studies. Only airway lengths, diameters and the total lung Functional Residual Capacity (FRC) were treated in this analysis. The FRC was used for data standardization and model validation purposes. Those quantities were represented by log-normal and gamma distributions in order to preserve positivity and reflect the fact that there are many random sources of variability. A similar approach was taken by Yu and Diu (1982), who extended this model to the acinar region. Still the symmetric branching pattern of Weibel was preserved.

Koblinger and Hofmann (1985) used the Lovelace morphometric data [Raabe et al. (1976)] as a foundation for the generation of their stochastic model, which incorporated both parameter variability and asymmetric branching in order to demonstrate intra-subject variability. Average values and frequency distributions of all the straightforward geometric characteristics of the airways, like diameters, lengths and branching angles, were derived through statistical analysis of the available data. Furthermore, correlations between lengths and diameters, between parent-daughter and primary-secondary daughter cross-sectional areas were investigated and presented in log-normal graphs. The lack of available data on the gravity angles was countered with the assumption that the azimuth is uniformly distributed over (0,2π). Finally, the probability that the bronchi have reached the acinar region with respect to the airway diameter is calculated (termed termination probability). The model derived provides parameter variability for all the properties of the airway tree as well as branching asymmetry. In a further research paper, the acini were regarded as single spheres [Koblinger and Hofmann (1990)] with diameters calculated by the studies of Hansen et al. (1975) and Haefeli-Bleuer and Weibel (1988). Inter-subject variability relations were not integrated to the model due to the lack of sufficient data. As pointed out in a personal communication between Hofmann and Fleming [Sauret PhD thesis (2000)], "the stochastic lung is too flat, problem due to the gravity angle selection".

Another asymmetric stochastic model based on the Lovelace data was developed by Phillips et al. (1994a, 1994b). Their goal was to classify the bronchial airways of normal lungs by their diameters instead by their position in the lung as was the norm in previous models. This was founded on the assumption that there is strong equivalence between airways of similar diameters, a conclusion that led to the creation of the Horsfield airway ordering scheme (see Section 2.5.4). A statistical reconstruction technique was applied to obtain the missing parts of the bronchial tree geometry based on the parent diameter at each bifurcation. The daughter diameters were considered to be random but not independent to each other and their distributions were correlated to the diameter of their parent. Similarly, the

probability distribution of the length of an airway was associated to its diameter. Using statistical analysis methods, the path length distributions along the airway tree, the distribution of airway volume and surface area among bronchi of different diameters, the asymmetry factors and the average flows as a function of diameter were calculated. The main features of this model are the asymmetry of the branching pattern, its dependence on airway diameters and the additional variability for each diameter value. Comparison of the results with the Weibel model (1963) showed qualitative differences. However, there was generally a good agreement with the asymmetric model presented by Horsfield and Cumming (1971).

3.3.3 Acinar Models

In most studies where the use of a model of the human pulmonary acinus is necessary, the acinus is usually approximated by a single sphere [Koblinger and Hofmann (1990)] with a diameter calculated from the relevant morphometric studies. However, in the last years, three comprehensive deterministic models of the internal geometrical structure of the acinus were presented in the literature for the purpose of modeling the respiratory tract in a descriptive and accurate fashion.

Denny and Schroter (1996) were the first, to our knowledge, to descriptively model the human respiratory acinus in a three-dimensional way. According to their method, the acinus is subdivided into ventilatory units, each unit consisting of the final respiratory bronchiole, the alveolar ducts and all their associated alveoli. The algorithm begins by modeling this ventilatory unit as a single 3D block of single-sized truncated octahedral, therefore constituting the unit a space-filling, 14-faced polyhedron. Its ventilation is done through a single opening in the block surface and the air is transferred to all the octahedra by opening some of their faces. A 3D branching structure representing the acinus is thus formed, with some polyhedra representing ducts and others representing alveoli. The branching pattern of the tree is determined computationally through two strictly mathematical criteria: The maximization of the number of alveoli and the minimization of the average

paths to these alveoli. These two conditions represent the need for maximal effectiveness of the gas-exchange functions performed by the acinus. Finally, the geometry of the acinus, the number of alveoli, alveolar sacs and generations, as well as the average path lengths per generation are calculated and compared with the data published by Mercer and Crapo (1987). Although the two datasets relate well, the model contains many simplifications such as identical alveolar and pathway dimensions for all generations, which are clearly unrealistic. Furthermore, it was not validated against human morphometric studies making the confirmation of its accuracy impossible.

Kitaoka et al. (2000) proposed a different method to simulate the acinar structure in a fully three-dimensional deterministic way. The algorithm developed was essentially what could be described as a 3D labyrinth generation process. The conditions imposed on the pathway construction procedure were that it should start from an entrance, it should pass through all the labyrinth "chambers" only once and that branching should be included. The whole acinus is regarded as a set of numerous cubic cells (chambers) and the intra-acinar pathway is just a sequence of those cells. The entrance of the acinus is the cell connecting it to the edge of the most distal respiratory bronchiole. The cell size is fixed to values consistent to previous morphometric studies and the mean path length to all cells is required to be as small as possible to accommodate the maximum effectiveness of air transport through the structure. Finally, when the pathway is fully determined, alveoli are attached on its inner walls. The average path lengths, total acinar and alveolar volumes and the branching patterns are then investigated and reported. There appear to be certain limitations to this model. The cubic nature of the acinar formation is clearly an unrealistic shape while it allows for branching only at right angles. Furthermore, the alveoli are assumed to be congruent. However, the resulting acinar structure compares well with past results, displaying similar properties to the data provided by Haefeli-Bleuer and Weibel (1988), Weibel (1991a), Hansen et al. (1975) and Hansen and Ampaya (1975).

Another model was suggested by Tawhai et al. (2003) who used the same hypothesis as both Denny and Kitaoka, that the alveoli and alveolar sacs form a nearly space-filling structure. The model is generated around the fact that the alveoli are not bubble-like but polygonal in shape with pentagonal or hexagonal facets [Weibel (1963), Prange (2003)]. A 3D Voronoi meshing method is used to generate a mesh with similar geometric characteristics to the alveolar tissue. The resulting mesh is continuous, space filling and has an alveolar-to-volume ratio within 2.7% of the data published by Weibel (1963). Other validation results were not made available by the authors.

3.4   Mathematical Modeling Of Pulmonary Airway Dynamics

As mentioned in Section 2.5.3, the airway tree is optimally designed for the function of transferring fluids of gaseous form from the atmosphere to the gas-exchange structures in the lung. In this section, the theoretic mathematical principles underlying the design of all organic tubular structures are investigated and the derivation of relationships between airway morphometric characteristics is explained.

3.4.1 Fluid Dynamics Basic Relationships

The fundamental relationships of hydraulics are defined by the *Bernoulli equation* which relates pressure, velocity and elevation at points along a streamline using the law of conservation of energy, i.e. the fact that the total energy at two points of the streamline must remain constant. If the flow of an *ideal* liquid (a liquid is considered ideal when it is incompressible and has zero viscosity) through a rigid conduit is examined, the Bernoulli equation becomes

$$P_x + \frac{1}{2}\rho \upsilon_x^2 + \rho g h_x = P_y + \frac{1}{2}\rho \upsilon_y^2 + \rho g h_y \quad (3.1),$$

where P stands for pressure, u is the liquid velocity through the cross-sectional area of the conduit, h is the elevation above some reference level, ρ is the liquid density and the subscripts x and y represent two random points along the conduit.

The above relationship is not very realistic since it doesn't take into account the internal and external frictions present during the flow of a viscous fluid. For that reason, the energy downstream is always smaller than the energy upstream or, if x is the point upstream and y downstream then the following equation stands:

$$E_y = E_x - E_{friction} \quad (3.2).$$

If this extra energy is considered, then a more realistic expression for the flow of fluids through rigid tubes can be derived.

The basic expression for the flow of fluids through rigid tubes is given by *Poiseuille's law*, which states that "the volume of fluid flowing past a point in the tube per unit time (Q) is proportional to the difference in pressure between the inflow and outflow of the tube (P_I-P_O) and the 4th power of the radius (r) of the tube, and inversely proportional to the length of the tube (L) and viscosity of the fluid (η)" [Green (1977)] or, in mathematical terms,

$$\frac{P_I - P_O}{Q} = \frac{8\eta L}{\pi r^4} \quad (3.3).$$

Since the second term of the equation represents those factors that retard flow, it is referred to as resistance

$$R = \frac{8\eta L}{\pi r^4} \quad (3.4),$$

which tends to depend mostly on the radius of the tube since viscosity η and length L usually remain constant. By combining equations (3.3) and (3.4) the most common form of Poiseuille's law is obtained, according to which

$$Q = \frac{1}{R}(P_I - P_O) \quad (3.5).$$

In the case of collapsible conduits the surrounding pressure P_S must be involved in the calculation of flow and formula (3.5) turns into the conditional equation

$$Q = \begin{cases} \dfrac{1}{R}(P_I - P_O), & P_I > P_O > P_S \\ \dfrac{1}{R}(P_I - P_S), & P_I > P_S > P_O \\ 0, & P_S > P_I \end{cases} \quad (3.6).$$

It has to be mentioned that the conduit collapsibility is relevant to *Hook's law of elasticity* which is expressed by the formula

$$\frac{F}{A} = K\left(\frac{L}{L_0} - 1\right) \quad (3.7),$$

where F is the force applied on a surface of total area A, K is a constant called the *Young's modulus* which is dependent on the material, L is the final length of deformation and L_0 is the length when the system is at rest.

The formulas presented above refer to laminar flows under horizontal conditions. However, hydrostatic factors affect the pressure flow relationships when the tube is tilted within a gravitational field. In such a non-horizontal case, the inflow pressure is modified with respect to the gravitational hydrostatic pressure effect. Inflow pressure P_I must be replaced by an effective inflow pressure P_{Ieff} given by the formula

$$P_{Ieff} = P_I \pm \rho g |\Delta h| \quad (3.8),$$

where ρ is still fluid density, g is the acceleration of gravity and Δh is the difference in levels between the tube entrance and the point of lowest

pressure in the system. Equations (3.5) and (3.6) must be modified accordingly.

3.4.2 Optimization Of Organic Tubular Systems Characteristics

The relationships described in the previous section can be used to reach some conclusions about the conditions necessary for the optimum efficiency of a tubular bifurcating structure. For all practical purposes, the efficiency of the conducting system can be said to depend primarily on the conduit diameters: Though the minimization of energy lost due to frictional forces is inversely proportional to the pipe diameter, the airways need to be metabolically maintained and also have to fit in a pre-determined space, a condition best satisfied by small diameter tubes. Obviously, a compromise between those conflicting conditions of optimal fluid flow must be reached.

Murray (1926) was the first to propose an optimum relationship between the flow and the diameter of an organic tubular structure using the principle of "minimum work", after which his model was named. The equations characterizing the airway tree were calculated to be

$$\frac{r_0^3}{Q_0} = \frac{r_1^3}{Q_1} = \frac{r_2^3}{Q_2} = c \quad (3.9) \text{ and } \begin{cases} \cos\theta_1 = \dfrac{r_0^4 + r_1^4 - r_2^4}{2r_0^2 r_1^2} \\[2ex] \cos\theta_2 = \dfrac{r_0^4 + r_2^4 - r_1^4}{2r_0^2 r_1^2} \end{cases} \quad (3.10),$$

where c is a constant, r_0, r_1, r_2, Q_0, Q_1 and Q_2 are the radii and flow rates of the parent, the primary and the secondary daughters respectively while θ_1 and θ_2 are the related bifurcation angles between parent-primary and parent-secondary daughter respectively. An equivalent "minimum volume" model was also developed to satisfy the second optimization requirement but it was shown to have more degrees of freedom than the minimum work model, constituting the latter the predominant process where laminar flow in a symmetric bifurcating system is concerned.

Horsfield and Cumming (1967) performed a similar type of analysis of the theoretical principles of the airway tree design, in which both conflicting conditions of airway diameter size are satisfied to the maximum degree. Since minimal energy loss implies minimum flow resistance, their first goal was the minimization of resistance. The branching system was considered strictly binary and symmetric, with the number of branches N in each generation w given by the equation

$$N = 2^w \quad (3.11)$$

and all the airway resistances of a single generation R_w were regarded to be a parallel resistance configuration, thus satisfying the relationship

$$\frac{1}{R} = \frac{1}{R_w} 2^w \Leftrightarrow R = \frac{R_w}{2^w} \quad (3.12).$$

Therefore, the total resistance of the airway system is

$$R_t = \frac{R_0}{2} + \sum_{w=1}^{w=W} \frac{R_w}{2^w} \overset{(3.4)}{\Longleftrightarrow} R_t = \frac{8\eta L_0}{\pi r_0^4} + \frac{8\eta}{\pi} \sum_{w=1}^{w=W} \frac{L_w}{2^w r_w^4} \quad (3.13).$$

where R_0 and L_0 are the resistance and length of the trachea and W is the total number of generations.

Furthermore, the expression for the mass of airway tissue M_w was derived:

$$M_w = 2\pi r_w L_w a\beta \quad (3.14),$$

with α being the wall thickness and β being the wall density. The wall thickness is known to be proportional to the bronchus radius [ICRP (1994), 2nd Chapter] and, therefore

$$a = r_W c, \quad c = \text{constant} \quad (3.15).$$

The total mass of the bronchial wall tissue is then

71

$$M_t = 2\pi r_0^2 L_0 \beta c + 2\pi\beta c \sum_{w=1}^{w=W} 2^w r_w^2 L_w \quad (3.16).$$

Equations (3.13) and (3.16) were combined and partial differentiation was performed to obtain the minimum R_t with respect to r_w. If $\dfrac{\partial R_t}{\partial r_w} = 0$, it can be shown that

$$r_w = r_0 2^{-\frac{w}{3}} \quad (3.17a),$$

which is equivalent to

$$r_{(w+1)} = r_w 2^{-\frac{1}{3}} = 0.794 r_w \quad (3.17b).$$

This expression is clearly the same as the one described by equation (2.1), derived by Weibel (1963) when the mean airway diameters were plotted against their generation number for the first 10 generations of a lung cast, making it a very powerful validating criterion for many models.

For the minimisation of the volume occupied by the tree structure a geometrical analysis was performed. For any symmetric branching structure it can be shown that

$$\begin{cases} \cos\theta_1 = \dfrac{r_0^2}{r_1^2} - \dfrac{r_2^2 \cos\theta_2}{r_1^2} \\ \\ \cos\theta_2 = \dfrac{r_2^2}{r_0^2} - \dfrac{\left(\dfrac{r_1^2}{r_2^2} - \dfrac{r_0^2 \cos\theta_1}{r_2^2}\right) r_1^2}{r_0^2} \end{cases} \quad (3.18),$$

which is exactly the same as equation (3.10) derived by Murray. In a symmetrical system where $r_1 = r_2 = 0.794 r_0$, $\theta_1 = \theta_2 = 37^{\circ}28'$. This is the optimal angle of branching for minimal volume in a system of minimal resistance and it has been confirmed to be a valid value through different morphometric

studies. A similar analysis for an asymmetric branching system produced the formula

$$\frac{r_1^2}{\sin\theta_1} = \frac{r_2^2}{\sin\theta_2} \quad \text{(3.19a).}$$

Finally, this equation was independently confirmed and modified by Kamiya et al. (1974) to include the parent airway too:

$$\frac{r_0^2}{\sin(\theta_1 + \theta_2)} = \frac{r_1^2}{\sin\theta_1} = \frac{r_2^2}{\sin\theta_2} \quad \text{(3.19b).}$$

In all the above, the flow of fluid through the tubes was considered to be laminar. However, especially in the lower generations where bronchi tend to have relatively high diameter values, turbulent flow can be frequently observed, thus affecting the relationships connecting the morphometric characteristics of the airway tree. Uylings (1977), while working on the optimization of the vascular and the airway tree, modified equation (3.9) giving flow rate Q into the expression of (3.23)

$$Q = Kd^n \quad \text{(3.20),}$$

where d is the tube diameter, K is a constant that depends on the organ and the fluid and n is a constant called the *diameter exponent* and depends on the type of flow.

In a different study, Horsfield and Thurlbeck (1981b) found methods for determining the value of n and compared the theoretical values to the predicted values of the diameter exponent. In order for all morphometric characteristics to be expressed with respect to n, the authors introduced the flow dividing ratio, which is here denoted as FDR, and can be described as the ratio of flow in the secondary daughter to that of the parent, or

$$FDR = \frac{Q_2}{Q_0}, \quad Q_0 > Q_1 > Q_2 \quad \text{(3.21).}$$

73

Furthermore, as Uylings suggested, "with optimal power dissipation the continuity equation holds for fluid movements in the successive conduits forming a bifurcation", thus constituting the following relationship valid:

$$Q_0 = Q_1 + Q_2 \overset{(3.20)}{\Leftrightarrow} d_0^n = d_1^n + d_2^n \quad (3.22),$$

d_0, d_1 and d_2 being the airway diameters of the parent, the primary and the secondary daughter respectively. The daughter diameters can now be expressed in terms of parent diameter and FDR while branching angles can be related directly only to the FDR [Kitaoka et al. (1999)] according to the formulae

$$\begin{cases} d_1 = d_0 FDR^{\frac{1}{n}} \\ d_2 = d_0 (1-FDR)^{\frac{1}{n}} \end{cases} (3.23) \text{ and } \begin{cases} \cos\theta_1 = \dfrac{1 + FDR^{\frac{4}{n}} - (1-FDR)^{\frac{4}{n}}}{2FDR^{\frac{2}{n}}} \\ \cos\theta_2 = \dfrac{1 + (1-FDR)^{\frac{4}{n}} - FDR^{\frac{4}{n}}}{2(1-FDR)^{\frac{2}{n}}} \end{cases} (3.24).$$

The value of the diameter exponent was reported by Horsfield and Thurlbeck (1981b) to vary between 2.4 and 2.9 for the airways of 4 mammalian species, the discrepancies probably due to the strong monopody displayed by the lungs of species walking on 4 legs. Uylings theoretically calculated it to be n=3 for laminar flow and n=2.333 for completely turbulent flow. Arterial studies for the value of n predict it to be around 2.7 while Kitaoka et al. (1999), analyzing the data provided by Raabe et al. (1976) estimated it to be n=2.8 for the human lung. Finally, Schmidt et al. (2004) found n to be 2.475 for the first 9 generations of a lung cast.

Another very popular way of measuring turbulence quantitatively is the *Reynolds number*, which is the ratio of inertial forces to viscous forces and is used for determining whether a flow will be laminar or turbulent [Andrade et al. (1998), Caro et al. (2001)]. It is given by the equation

$$\text{Re} = \frac{\rho \upsilon_s d}{\eta} = \frac{Inertia}{Vis\cos ity} \quad (3.25),$$

where ρ, u_s, d and η are fluid density, mean fluid velocity, tube diameter and fluid viscosity respectively. Laminar flow occurs at low Re, where viscous and frictional forces are dominant while turbulent flow occurs at high Reynolds numbers and is dominated by inertial forces which produce different types of fluctuations. For tubular systems, the critical Reynolds number for transfer between laminar and turbulent flow is generally accepted to be in the range between 2100-2500.

3.5   Aerosol Deposition In The Airway Tree

The final section of this chapter will be concerned with the particle deposition mechanisms in the human airway tree. Furthermore, some relevant models that attempt to accurately describe these mechanisms with reference to the anatomical pulmonary airway models presented previously will be related.

3.5.1 Aerosol Classification

In order for aerosol deposition patterns to be comparable, the aerosol particles must be classified with reference to their physical and electrical features. One of the most common terms for categorizing particles with respect to their physical properties is their "*aerodynamic diameter*" (d_{ae}). For a particle of arbitrary shape and size, its aerodynamic diameter is defined as the geometric diameter of an equivalent spherical particle of unit density that has the same gravitational settling speed as the particle under investigation. For a droplet, this can be mathematically described as

$$d_{ae} = (\rho)^{\frac{1}{2}} d_g \quad (3.26),$$

where ρ is the droplet density and d_g is the geometric diameter.

For medical applications, an aerosol cloud, produced during drug delivery to a patient's lung, must be treated statistically. For that purpose, cascade impactors are employed in order to measure the *Mass Median Aerodynamic Diameter* (MMAD) and the *Geometric Standard Deviation* (GSD) of the particle size distribution. Based on these quantities, the behavior of the aerosol cloud can be predicted and the deposition of its constituent particles can be calculated.

3.5.2 Aerosol Deposition Mechanisms

There are four dominant particle deposition mechanisms in the human airway tree: deposition by sedimentation, impaction, diffusion and electrostatic effects.

Gravitational Sedimentation

This process describes the deposition of aerosol particles in the airways of the tracheobronchial tree as the result of gravitational pull during particle motion. It is obvious that this must be dependent on both particle size and the particle residence time within the respiratory tract. For that reason, the probability that a particle will settle by sedimentation (P_{set}) is given by

$$P_{set} \propto d_{ae}^2 T \quad (3.27),$$

where d_{ae} is the aerodynamic diameter characterizing size and T is the residence time, which can be written as

$$T = \frac{L}{\upsilon} \quad (3.28),$$

L being airway length and υ mean aerosol velocity. Sedimentation becomes increasingly important for particle size above 0.1μm and is dominant at peripheral lung regions where the flow and, therefore, the velocities,

decrease. Breath-holding further increases the effects of deposition by sedimentation.

Inertial Impaction

When a particle is transported by means of a fluid with mean velocity υ along a predetermined flow path, if the path deviates from a straight line by an angle θ then the particle will temporarily obtain a trajectory different from the one defined from the fluid stream. The particle will move along this trajectory until it loses its temporary momentum, in which case it will passively follow the fluid flow streamline along the new direction. The temporary aerosol velocity is determined by the angle θ as is the particle deflection displacement along its temporary path. In the case of the human lungs, such diversions from the straight path occur at bifurcation points. If the temporary trajectory at airway branching points brings the aerosol particle in contact with the bronchial wall and the particle doesn't deflect back to the air streamline then deposition by inertial impaction has occurred.

Inertial impaction increases with fluid velocity, the square of aerosol size and the branching angle. For that reason it becomes dominant at the upper respiratory system and it is important mainly for particles with $d_{ae}>2\mu m$. However, since turbulent flow affects this type of deposition, inertial impaction may also occur locally in the area between the cartilaginous rings that line the respiratory tract. Fluid motion at these regions affects mostly particles of geometric diameter $d_g<0.5\mu m$ and can enhance deposition by diffusion processes [Martonen et al. (2000)].

Brownian Diffusion

The random Brownian motion of particles due to collisions with fluid molecules can also lead to particle deposition. This type of deposition is particularly evident in fluids of gaseous form, where molecules move more vigorously, and it depends both on particle size and on residence time in the respiratory tract. The smaller the particle the more it is affected by molecular collisions and the longer it remains in the lung the more likely it is

to come in contact with the bronchial walls. The probability of deposition by diffusion (P_{diff}) reflects this:

$$P_{diff} \propto \sqrt{\frac{T}{d_{ae}}} \quad (3.29).$$

Brownian diffusion is important for the peripheral parts of the lung like the bronchioles and the acini. In addition, this process is particularly significant for particles with $d_{ae} < 1\mu m$.

Electrostatic Forces

Another factor that may affect the deposition of particles in the respiratory tract is the electrostatic features of the inhaled aerosols. There are two types of electric charge effects that are of significance for this deposition mechanism. The first is the image force. When an electrically charged particle approaches the airway wall, which is uncharged but electrically conducting, an image charge of opposite polarity will be induced on the wall. This will attract the particle according to the rule

$$F \propto \left(\frac{q}{mr}\right)^2 \quad (3.30),$$

where F is the attraction force, q and m are the charge and the mass of the particle respectively and r is its distance from the airway wall. The particle probability to deposit (P_{elec}) is given by the equation

$$P_{elec} \propto \sqrt[3]{\frac{q^2}{d}} \quad (3.31),$$

with q and d being the particle charge and diameter [Sauret PhD thesis (2000) citing Melandri et al.].

The second type of electrostatic effect is called the space charge force. It is more evident when there are high concentrations of similarly polarized

charged particles, in which case mutual repulsion forces appear between them that may result to their coming in contact with the walls of the respiratory tract. Both types of electrostatic effects are mainly evident in the alveolar regions where the particles are closer to the walls than in any other part of the lung. According to Martonen et al. (2000), the available information suggests that the image forces are stronger than space charge forces and thus affect more the motion and deposition of aerosol particles.

Interception, Cloud Settling And Other Forces

Deposition by interception occurs when the particle remains in the fluid stream even at bifurcation points but its size and shape are such that the particle still comes in contact with the airway wall. For an arbitrary particle that would mean that its aerodynamic diameter is higher than the airway diameter. Interception, however, becomes increasingly effective for particles of elongated shapes, which may play critical role to targeted inhalation therapy.

Another mechanism that is worth mentioning is what is characterized as cloud settling. When there are high particle concentrations then the aerosol may behave as a single entity, masking the characteristics of its individual constituent particles. Martonen et al. (2000) citing his previous work suggested that the critical concentration for this phenomenon to occur is in the area of $5x10^{-8}$ g/cm^3.

Other forces that may be present in the lung, such as magnetic, acoustic or thermal, are of no particular significance and are usually ignored.

3.5.3 Aerosol Deposition Models

Modeling aerosol deposition in the airways of the human respiratory tract comprises of three major elements: A morphometric model of the bronchial tree, a set of equations describing the deposition mechanisms at different airways and a process for particle transport to different areas of the lung.

There are many models that combine those elements in order to make accurate predictions of particle deposition in the human lung. The first such model was proposed by Findeisen (1936) [also described by Landahl (1950)], who compartmentalized the lung into nine regions and then derived expressions on deposition efficiency based on particle mechanics principles. This was rather successful compared to earlier measurements and has been formally used in predicting the regional deposition of aerosol particles in the respiratory system by the International Commission on Radiological Protection [ICRP Task Group (1966)]. However, this model assumes a steady breathing cycle and instant gas mixing. Taulbee and Yu (1975) and Yu and Diu (1982) tried to rectify this by applying particle deposition mechanisms to the trumpet model (Section 3.3.1) and creating a transport model adjustable to different breathing patterns. A similar approach was taken by Egan and Nixon (1984).

Gerrity et al. (1979), Yeh and Schum (1980) and Koblinger and Hofmann (1990) also based their calculations on Findeisen's model, Gerrity using the Weibel "model A" morphometric model, Yeh and Schum developing their own established on the Lovelace data and Koblinger and Hofmann using the stochastic model developed by their own group in 1985. Finlay et al. (1996), during their study of transport and deposition of hygroscopic aerosols, based their calculations on the stochastic model proposed by Phillips et al. (1994a, b) and the acinar data provided by Haefeli-Bleuer and Weibel (1988). Furthermore, Martonen (1992) presented a model that uses a consistent set of particle deposition equations derived by Martonen (1982) in order to systematically describe hygroscopic particle deposition without the irregularities present in the equations used in previous studies. Finally,

Mitsakou et al. (2005) developed a dynamic model of aerosol deposition based on an Eulerian approach. This was done by numerically solving the particle general dynamics equations in a mechanistic fashion within a modified trumpet morphometric model.

3.6 Summary And Conclusion

In this chapter, a review of the most important medical imaging modalities with respect to their applicability for lung measurements was made. This was done in order to investigate the best method of utilizing the imaging data available for this study. Furthermore, several morphometric models of the human airway tree were presented and analyzed, with the main purpose of exploring their strengths and limitations as well as setting the foundations for the development of an improved model. The main principles of flow dynamics that exist in tubular branching systems were also discussed with reference to the gas transport occurring in the human respiratory tract. Many of the equations explained there form the basis of many literature models and will be used for the creation of the main model described in this thesis. Finally, the main particle deposition mechanisms that are found to exist in the human tracheobronchial tree were shown and some particle deposition models presented in the literature were briefly discussed.

It becomes obvious that since medical imaging is currently unable to provide information on the human airway tree beyond a certain depth even when performed *ex-vivo*, mathematical models of the tree structure have to be applied to fill in the missing information. It is also apparent that aerosol deposition studies and, therefore, targeted inhalation therapy applications are dependent on the accuracy and quality of the predictions of the specific morphometric models employed. Although several anatomical models exist in the literature, the need for better precision of lung airway location and for more comparative data for validation purposes is still driving the field. The next chapter will be concerned with the development of a generalistic model

that was created with the specific purpose of it being immediately applicable in combination with radionuclide imaging protocols such as SPECT, the Hybrid Conceptual Model. This model, which is an improvement over the Conceptual Model published by Fleming et al. (1995), will also be used as a validation benchmark for the deterministic model that will be described in further chapters.

Chapter 4

The Hybrid Conceptual Model of the human lung airways

4.1 Introduction

The purpose of this chapter is the development and discussion of an improved version of the conceptual model, which was named the Hybrid Conceptual Model (HCM) for reasons that will become apparent in the subsequent sections. Although the original conceptual model was briefly described in Section 3.3.1, a more detailed explanation of its basic rules and conclusions must be given before proceeding to the creation of a new algorithm. Each step of the new Hybrid Conceptual Model algorithm will then be presented and the algorithm's results will be discussed. An effort will also be made for the validation of these results with reference to previous studies. Finally, improvements and further work on the algorithm will be related, along with an overview of its suggested functions.

4.2 The Conceptual Model Of The Human Lung Airways

As mentioned in Section 3.3.1, the conceptual model [Fleming et al. (1995)] was developed in order to describe air volume per generation at different lung regions and it was intended for immediate application to image analysis as described by Perring et al. (1994). The model derives its name from the fact that there is no information on the explicit spatial location of individual airways. In this section a more detailed look on its workings and conclusions, which form the foundation of the hybrid conceptual model, is given.

created with
nitro^PDF professional
download the free trial online at nitropdf.com/professional

In the conceptual model the spatial distribution of the airway network is described in relation to a hemispherical transform of the lung. The lung space, obtained from either MRI or CT scans, is described as a three-dimensional matrix comprised of cubic voxels. Each lung is treated separately to avoid ambiguities. For each voxel in the lung space, a straight line connecting it to the hilum was extended toward the periphery of the lung and the corresponding lung surface voxel was found. The fractional radial distance was then calculated as the ratio of the distance of the voxel under examination from the hilum, d_v, divided by the distance of the extrapolated surface point from the hilum, d_{vs}. The lung space is then divided in 10 hemispherical regions called shells based on the fractional distance ratio

$$FDR = \frac{d_v}{d_{vs}} \quad (4.1).$$

The results of a hemispherical transform on a human lung space can be observed in Figure 4-1. Since $d_{vs} \geq d_v$, the first decimal point of the ratio defines in which shell each voxel belongs to. It must be noted that the radial transform process may affect the accuracy of the model. A more detailed explanation of an algorithm that performs this function and its evaluation will be given in a subsequent section.
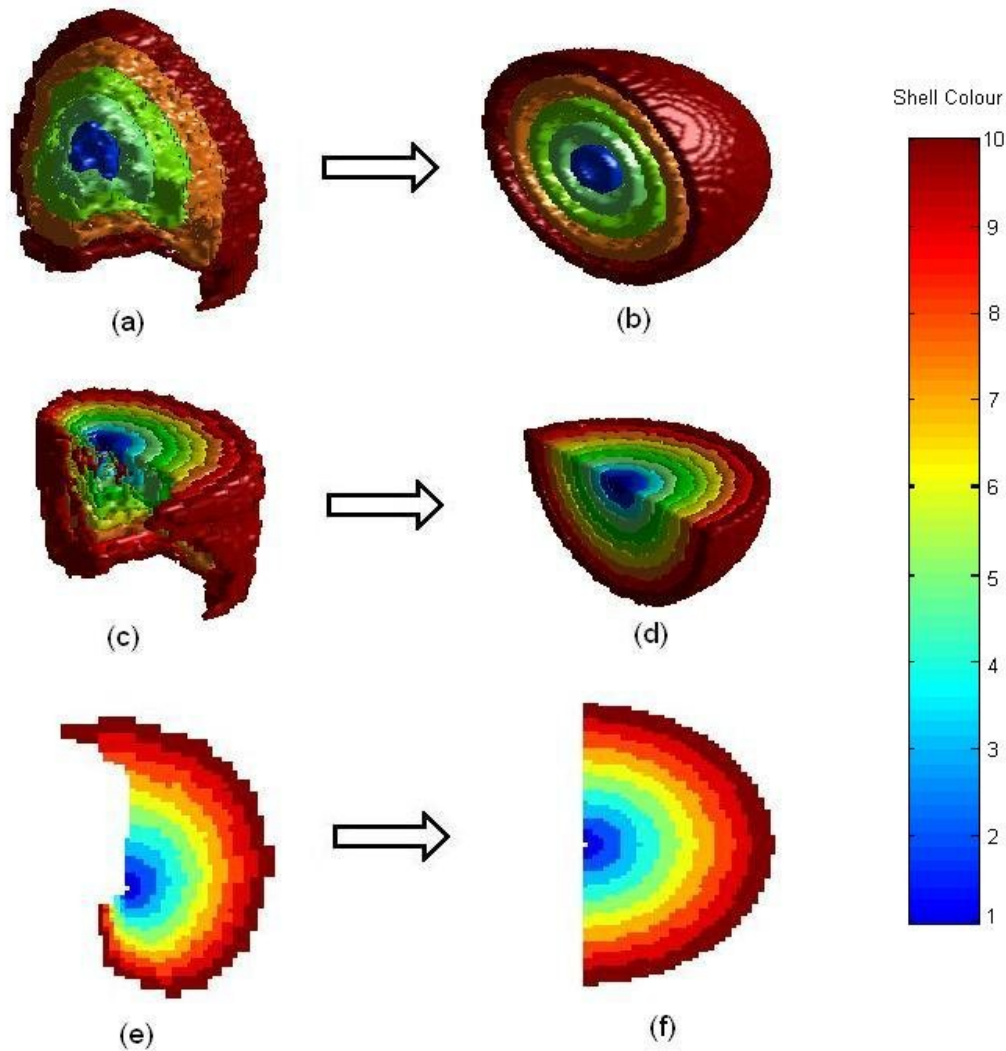
Figure 4-1: Transformation of the right lung shape to a series of concentric hemispherical shells. Similar shells have the same colours, defined by the colorbar on the right. (a), (c) and (d) show different visualizations of the lung space while (b), (d) and (f) display the corresponding hemispherical transformation visual representations.

The model then is required to assign the volume of each generation, denoted with symbol j, in each shell, i, designated V_{ij}. To accommodate the lack of structural airway tree data in distal regions of the lung, only the first 14 generations (with trachea being generation 0) are regarded as conducting airways while the remaining generations (15-23) are treated as acini. There are two major assumptions that form the basis of the conceptual model. The first is that the conducting airways follow paths that extend radially outwards from the hilum and terminate in an acinus. The model assumes that there is a

85

smooth gradation of each airway path through the generations, since there is considered to be an equal number of airway paths in each conducting airway generation 1-14. This is an approximation to the realistic case where very short paths to acini that tend to occupy some space in areas close to the hilum exist. The conceptual model allows for this in that it assumes there are acini from shell 2 outwards. The second major assumption is that the acini fill the remaining volume uniformly, which means that the number of airways terminating in a shell must be equal to the number of acini in that shell. Thus the conceptual model divides the airway paths into ten groups, one for each shell.

There are some other important conditions that have to be applied, expressing some important anatomical characteristics of the airway tree, for the model to be functional. First of all, shell 1 is considered to obtain no acini as no such short path to acinar structures can be observed. Furthermore, no conducting path can terminate to the distal part of shell ten, which contains the areas of the lung closest to its surface, due to the finite space occupied by an acinar unit. This implies that all voxels with $0.95 < FDR < 1.00$ contain no conducting airways but only acini. In addition to that, the hilum coordinates are calculated accurately at the position where the main bronchi penetrate into the lung. Finally, the airway morphometric data used for the development of the model are those published by Weibel (1991a). Some of these assumptions are improvements over time of some of the initial model conditions and were developed in a study by Fleming et al. (2004a) with the purpose for creating an advanced form of the conceptual model before validating it.

Following the assumptions stated above and using previously published data, the number of acini in each shell can be defined. V_{ij} can then be evaluated using information on the actual lengths and diameters of airways. The final result is a matrix of the volume of each generation in each shell, for generations 1-14, plus the acinar volume in each shell. The advanced conceptual model V_{ij} matrix, normalised to a standard Functional Residual Capacity (FRC, see Section 2.4) of 3.3l is given in Table 4.1. Based on that, 15

three-dimensional matrices of the lung space can be constructed, each voxel of each matrix representing the airway volume for each generation that is included in the specific voxel of the specific shell. This is calculated by spreading the estimated V_{ij} homogeneously over each shell using the relationship

$$VVoxel_{ij} = \frac{V_{ij}}{V_i} \quad (4.2).$$

The advanced conceptual model was shown to compare well with previously published models both in the aspect of total generation airway volume per generation and with respect to the calculated mean airway position within the lung. One important advantage of this model is the fact that it can be adapted easily to fit any probable lung shape, which is a fundamental requirement for any model used for medical image analysis, along with its three-dimensional nature. However, it has some inherent disadvantages. The rest of this chapter tries to overcome these with the introduction of the Hybrid Conceptual Model.

Generation number	Shell Number										Total
	1	2	3	4	5	6	7	8	9	10	
1											
2	2.73	1.51									4.24
3	0.05	1.41	1.29								2.76
4		0.26	1.20	0.93							2.40
5		0.10	0.41	1.37	1.46						3.33
6		0.05	0.19	0.65	1.22	1.53					3.64
7		0.02	0.12	0.31	0.81	1.41	1.10				3.79
8		0.02	0.05	0.22	0.53	0.72	1.51	0.55			3.59
9			0.05	0.12	0.26	0.74	1.15	1.22			3.55
10			0.05	0.14	0.29	0.46	0.74	1.63	0.89		4.19
11			0.02	0.14	0.41	0.60	0.91	1.32	1.80		5.20
12			0.02	0.10	0.22	0.69	1.25	1.73	2.66		6.66
13			0.02	0.12	0.26	0.55	0.93	1.46	2.16	2.90	8.41
14			0.02	0.12	0.29	0.60	1.01	1.58	2.18	3.11	8.92
Acini		7.88	29.4	80.67	158.29	278.69	408.63	572.31	746.92	956.5	3239

Table 4.1: Matrix showing the volume of each generation in each shell in ml.

4.3   The Hybrid Conceptual Model Of The Human Lung Airways

As mentioned previously there are some inherent disadvantages to the use of the conceptual model. First of all, it was shown that even the advanced conceptual model introduces some errors in assessing deposition per generation from imaging data. These errors could be significantly reduced if an individual's airway anatomy was used for the analysis of aerosol deposition per generation instead of a generic model. Since it is possible to determine the airway tree structure down to about generation 8 using CT scanning, an effort is made for such data to be integrated to the conceptual model. Since the location of the airways of the first few generations is now explicitly stated, the model cannot be referred to as conceptual but is more like a hybrid, hence the new model's name. Moreover, the conceptual model considers the airways to be evenly distributed throughout each shell, an

assumption obviously incorrect. For that reason, a method for a more realistic distribution of the airways in a shell structure will also be investigated in this chapter. This will be done by utilizing the data obtained in the literature to interpolate lung voxel values with respect to fractional distance ratios. The hybrid model will also be compared to previously published data in order to examine the accuracy of the results.

The medical imaging data used in this project were supplied by Professor J. S. Fleming, Department of Medical Physics and Bioengineering, Southampton University Hospital NHS Trust. The images were acquired as part of a previous research study for which permission was obtained from the Local Research Ethics committee. The data include MRI images of one human subject volunteer providing us with the lung outline. CT scan data of the same subject's airway tree were also made available, representing the first 5 generations (0-5) of the bronchial tree, along with the airway volume per generation per shell data presented in Table 4.1. The MRI scan data were previously manually aligned to the CT images so no registration process was necessary in this part of our study. After the alignment, computerised image analysis provided the exact location of the hila, which are considered to be at the points where the main bronchi infiltrate the lungs. More precisely, the hilum will be defined as the midpoint of the cylindrical tube representation of the main bronchus at the exact point where the main bronchus intersects the lung. The lung volume of the MRI and CT images is considered to be comprised of cubic voxels with 2.6mm linear dimension, given in 128x128x128 matrices. The program to be used for image analysis and algorithm implementation throughout this study is MATLAB version 6.5. Finally, each lung is treated separately in order to enable the comparison between them.

The process used for the creation of the hybrid conceptual model can be summarised in the following diagram.

INPUT: MRI and CT images, Vij tabulated data

↓

Shell creation and fractional distance ratio calculation

Vij recalculation

Data interpolation with respect to fractional distances

↓

OUTPUT: 15 3D matrices of the human lung space, each voxel of each matrix showing airway density
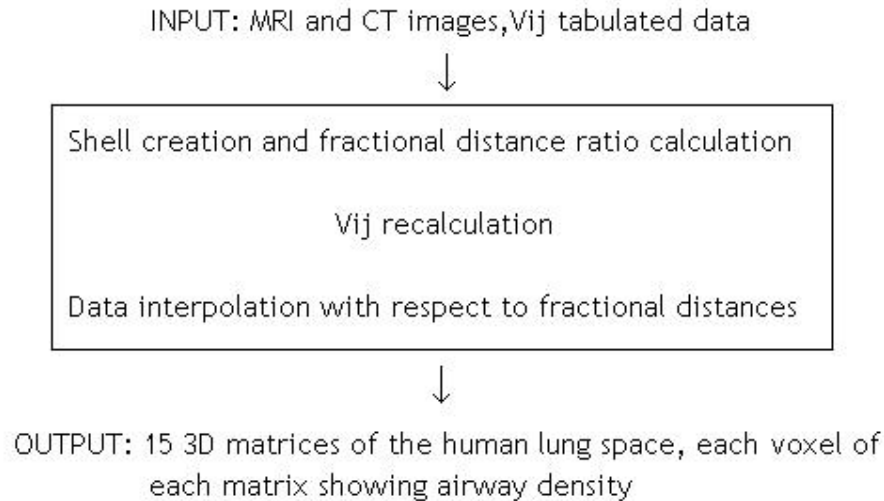
4.3.1 Image Data Inputting And Verification

Before proceeding with the hemispherical transformation of the lung space, the CT and MRI scan data must be stored to the system in a readily usable form and, if necessary, also be rearranged or realigned. The MRI scan displays the lung space in a binary 128x128x128 matrix, with each voxel obtaining the value 1 if it belongs to the lung space and the value 0 if it doesn't. The lungs are viewed from a position as if the subject was in a supine position facing up and the imaging perspective is from the direction of the feet. The dataset can be reconstructed in 3D using interpolation algorithms to fill in the missing information between transverse slices. A two dimensional representation of the MRI data of both lungs, displayed as a series of 2D slices in a 16x8 matrix can be seen in Figure 4-2(a), along with the 3D reconstruction based on these images in Figure 4-2(b). The surface of the reconstructed lungs has also been smoothed using filtering processes in order to obtain a more accurate anatomical representation of the organ.

The CT scan data represent the first 5 generations of the human airway tree, with the trachea being generation 0. They have previously been segmented [Sauret PhD thesis (2000)] using a thresholding algorithmic technique and are divided into 5 separate datafiles, one per generation. Every voxel of each generation can take up values in the range 0-64, each value representing air

90

volume of the airways of the generation contained in the voxel in question. The air volume is connected to the voxel values through the relationship

$$V_i = 0.000347 C_i \quad (4.3),$$

where C_i is the voxel value contained in each file. The maximum air volume allowed in a voxel can be 0.0222ml.

A two- and three-dimensional reconstruction of the data follows using the same process as for the MRI images. Before being applied to the coordinate system defined by the MRI scan, the airway data needed to be rotated by 180° along the z-axis. After this rotation was performed (final airway system is displayed in 2 and 3D in Figure 4-2(c) and (d) respectively), the resulting airway tree was superimposed to the lung data. Since the coordinates of the hila locations were available, the proper alignment of the two datasets was confirmed. If the lung surface is made transparent, the alignment of the two systems can also be visually confirmed (Figure 4-3). It is now possible to proceed to the next stage which is the hemispherical transform of the lung space.
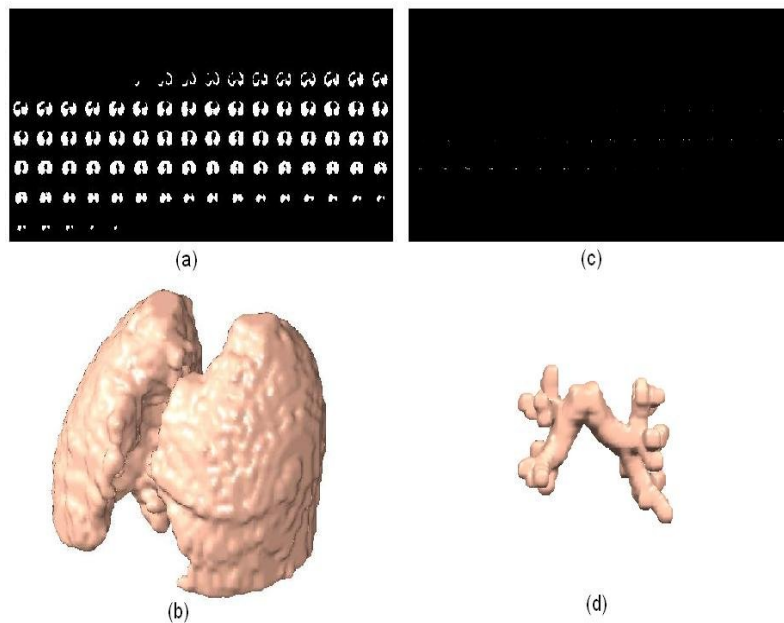
Figure 4-2: (a) MRI scan of the lung, (b) its 3D reconstruction, (c) CT scan of the airway tree and (d) its 3D reconstruction.
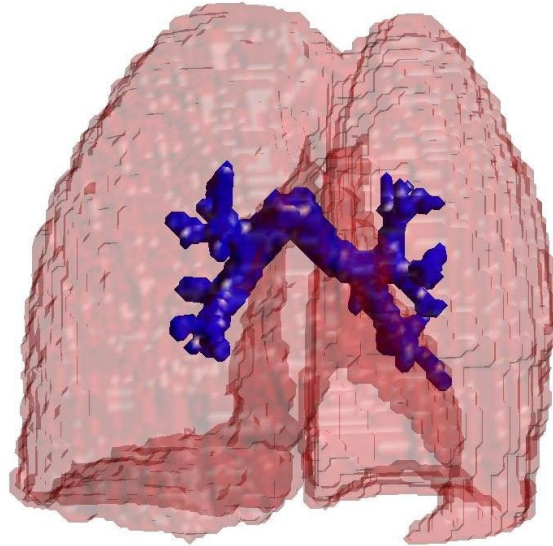
Figure 4-3: Airway tree superimposed on the lung data. The lung surface is transparent to allow visual contact with the bronchi.

4.3.2 Shell Creation Algorithm

Methods

The ultimate goal of this process is to uniquely map each voxel in the lung space to a voxel in a hemisphere with the same volume as the lung (Figure 4-1). The mapping will occur with respect to the fractional distance from the hilum, which is also considered to be at the centre of the hemisphere, to the extrapolated periphery of the lung as displayed in Figure 4-4. For the fractional distance ratio of a voxel to be calculated, a straight line connecting it to the hilum has to be extended to the lung surface, thus associating the voxel under investigation to a surface voxel. The constraints imposed on the line generation process are:

➢ The line must be continuous.

- It must extend all the way to the surface.
- It must be discrete in implementation.

The corresponding distance of the examined voxel with coordinates (x_v, y_v, z_v) and the surface voxel can then be used to calculate the necessary ratio. The process must be applied iteratively to include all lung space voxels.

A 3D straight line generation algorithm was first developed. Every line in 3D can be defined using an origin point and two angles, the azimuth and the elevation. In a three-dimensional Cartesian coordinate system where axes x, y and z define length, depth and height respectively, the azimuth is defined as a polar angle in the x-y plane while elevation is the angle above or below the x-y plane (Figure 4-5). Obviously, the elevation can be identified with reference to either the x or the y axis. In the case where the coordinates of each voxel can easily be obtained and the origin-point (hilum) is known, every angle in the lung space can be calculated with the help of the equations:
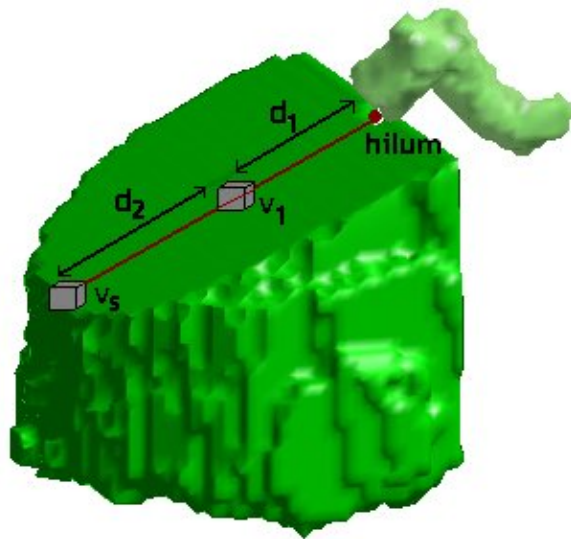
Figure 4-4: The shell creation process. A straight line, passing through the voxel v_1, extends from the hilum to the edge of the lung, denoted by voxel v_2, and the corresponding distances are calculated.
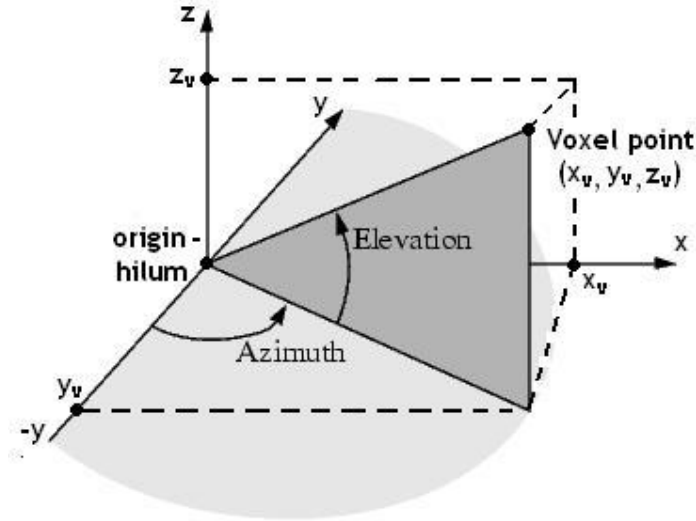
Figure 4-5: The azimuth and elevation angles of a voxel defined with reference to the point of origin (hilum).

$$\begin{cases} \theta = \tan(azimuth) = \dfrac{x_v - x_{hilum}}{y_v - y_{hilum}} \\[2ex] \omega = \tan(elevation) = \dfrac{z_v - z_{hilum}}{\sqrt{(x_v - x_{hilum})^2 + (y_v - y_{hilum})^2}} \end{cases} \quad (4.4).$$

It is now possible to identify the discrete line elements, i.e. the voxels of the system that belong to the straight line which is defined by the examined voxel and the hilum. The mathematical representation of a continuous straight 3D line is used:

$$\begin{cases} y = \tan(azimuth)x + b \\ z = \tan(elevation_x)x + c \end{cases} \quad (4.5),$$

where b and c are constants and elevation$_{xz}$ is the element of the elevation on the x-z plane. The voxel coordinates (x_v, y_v, z_v) are used to solve the equation system for b and c. The equations are then utilized for the calculation of consecutive y and z values based on an iteration of integer x values. The computed values of y and z coordinates are then rounded to the closest integer value and stored along with the x coordinates. To reduce

94

computer power expenditure and avoid ambiguities in edge detection, directionality will be induced to the system by implementing the line with vector characteristics. This will result in the x iterating through pre-specified ranges depending on the examined voxel location in the lung space.

A problem that may occur is what may be referred to as the discretization or pixel effect. This has as a consequence that the discrete line generated may be discontinuous, i.e. that a line voxel may have no neighbouring voxels that also belong to the line. This is overcome by comparing consecutive line voxel coordinate values and estimating the voxel coordinates between them that are missing from the line. The whole process of line generating the straight line finishes when one of the line element coordinates exceeds the dimension range set by the MRI image matrix. All the line element coordinates are finally tabulated and stored.

A simple edge detection method will also be applied for the location of the lung surface voxels. A 3D low-pass Gaussian filter is employed on the image data and the fact that only voxels at the edges lose their original values is exploited. The implementation of the filter is a simple 9x9 cubic structure with a one at the centre of the matrix and elements between zero and one in the periphery, with their values decreasing the closer we get to the periphery.

A generated line may pass through several surface voxels, thus causing difficulties to the selection of the appropriate surface voxel with reference to which the fractional distance ratio will be calculated. This is avoided by computing the distance of all such voxels from the hilum and choosing the voxel with the longest such distance to be the extrapolated voxel at the lung edge. After the surface voxel is selected, the calculation of the fractional distance ratio becomes possible, based on equation (4.1). The process is repeated for all voxels in the lung space and the ratios are stored in a 3D initially blank matrix, each ratio in the voxel with the same coordinates as the voxel under examination throughout each iteration. The shell matrix is

just an adaptation of the fractional distance ratio matrix, where each voxel is assigned a shell value equal to the first decimal number of the ratio.

Results

Since the dataset is discrete in nature, there may be certain discrepancies between the theoretical and the experimental results of the shell creation method described above. These discrepancies may account for some of the inconsistencies between the advanced, hybrid conceptual model and other models. For that reason, the shell algorithm is applied both on the lungs (Figure 4-6) and on an experimental hemisphere of the same volume as the lung. The quantities measured are the percentages of volume per shell as compared to the total volume of the space investigated. Furthermore, the algorithm results are compared to the shell creation method employed by Fleming et al. (2004a). Finally, a mathematical analysis of a purely theoretical hemisphere with unit radius per shell is made and the volumetric percentages are related. This is done by employing the sphere volume calculation formula

$$Vsphere_k = \frac{4}{3}\pi r_k^3 \quad (4.6)$$

where r_k is the radius of the hemisphere including shell k and the volume of each shell is given by subtracting the volume of the hemisphere that includes the previous shell,

$$Vk = Vsphere_k - Vsphere_{k-1} \quad (4.7).$$

The data are presented in Table 4.2, on which the graph of Figure 4.7 is also based.

Figure 4-7 displays the differences between the shell creation processes based on comparisons between the volumetric percentages per shell for the whole lung. It can be observed that the highest divergence between shell volumes as percentages of total lung volumes occurs in shell 10. The

algorithm shows similar results for both the lung and the experimental hemisphere. There is a 2.5% difference in shell volume in the 10th shell between the two models and a 4% difference between the hybrid model and the theoretical hemisphere shells. All four models can be observed to follow the same general form resembling roughly a square law.

Shell number	Hybrid model on the average of both lungs	Hybrid model on experimental hemisphere	Advanced conceptual model	Theoretical hemisphere with unit radius
1	0.095	0.12	0.03	0.1
2	0.65	0.76	0.3	0.7
3	1.61	1.79	0.97	1.9
4	3.475	3.64	2.57	3.7
5	6.03	6.44	4.95	6.1
6	7.725	8.11	8.65	9.1
7	12.095	12.08	12.64	12.7
8	16.13	15.84	17.67	16.9
9	20.985	20.4	22.98	21.7
10	31.06	30.8	29.24	27.1

Table 4.2: The ratios of volume per shell to total object volume calculated for the shell creation algorithm of the hybrid conceptual model on the lung image data and an experimental hemisphere, the data of the shell creation algorithm of the advanced conceptual model and the ratios of a mathematical analysis on a theoretical hemisphere.

(a)   (b)
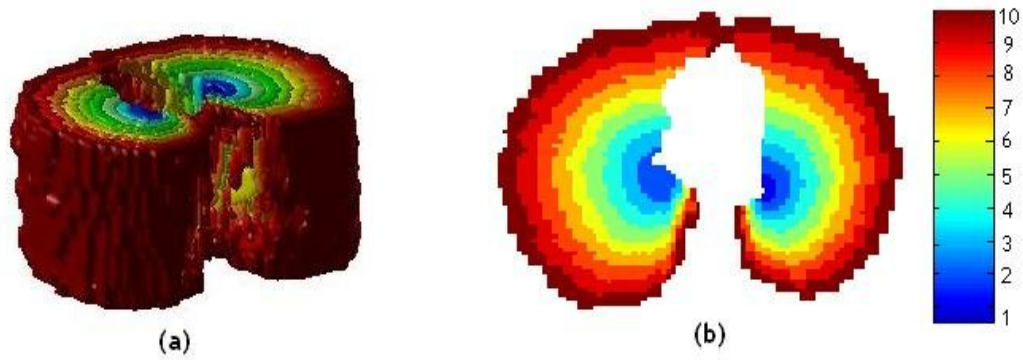
Figure 4-6: (a) A three-dimensional representation of the shells on both lungs and (b) the top transverse slice of the 3D matrix presented in (a) shown in two dimensions. The colorbar denotes which region belongs to which shell.
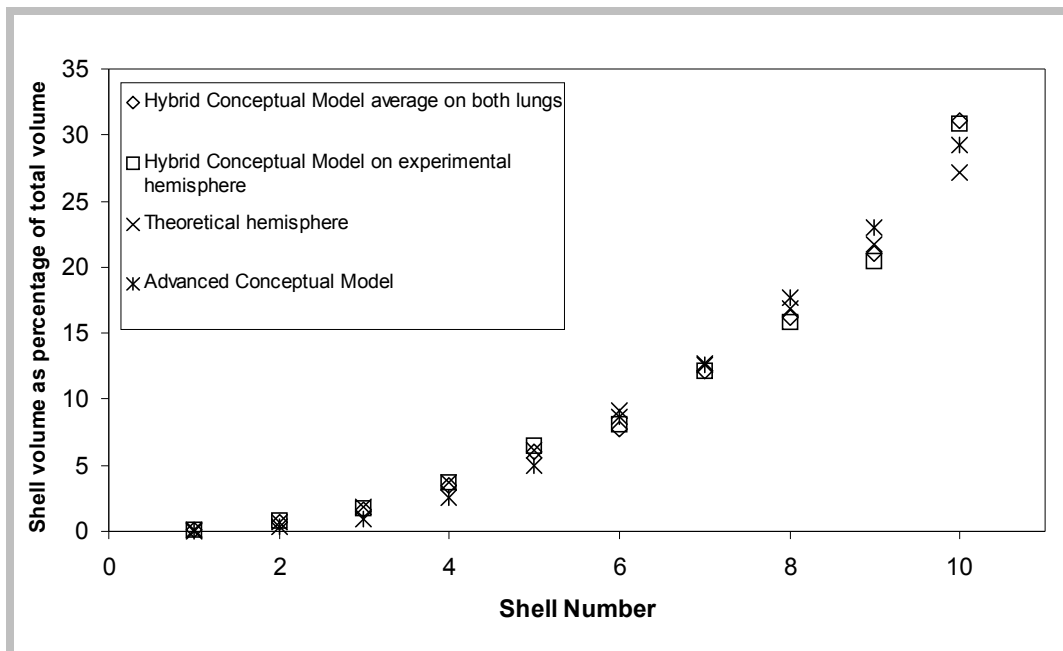
Figure 4-7: Plot of the shell volume to total object volume ratios of the processes described in the graph legend.

Discussion

The graph of Figure 4-7 displays certain differences between different shell creation processes. These differences increase in magnitude in larger shell numbers, which is logical since discrepancies will tend to occur in areas consisting of high numbers of voxels, i.e. areas with higher volumes. The highest divergence between shell volumes as percentages of total lung volumes occurs in shell 10. This indicates that the shell creation process used in this study produces a larger shell 10 than both the theoretical hemisphere and the algorithm used in the previous conceptual models, which has as a result the generation of lower air volume per voxel at this part of the lung. If this 4% difference is translated to absolute values, then a drop of 15% for airways in shell 10 is estimated. Therefore, this effect has to be taken into account when the hybrid conceptual model is created in the following sections, since it affects the estimate of the acini density at the periphery of the lung, which is now also reduced. It also has to be mentioned that this 4% difference that is present in the 10th shell seems to lead to a consistent but small underestimation of all the previous shell volume ratios for the hybrid conceptual model shell creation algorithm, which is logical since the volume ratios compared have to be equal to the total object volume when summed.

This variation reflects the difference in the shell definition algorithms used for the advanced conceptual model and the hybrid conceptual model and suggests that special care must be given to the consistency of the of the different methods employed for shell analysis with respect to the shell volumes that are produced. Moreover, the discrete nature of the datasets used may increase these effects. However, no considerable differences are present neither in absolute values nor in the form of the graphs produced. Hence, the algorithm developed in this section can be used with great confidence for shell analysis of the lung space.

4.3.3 Calculation Of Volume Per Generation Per Shell (V_{ij})

Methods

The next step in the development of the hybrid conceptual model is the incorporation of the CT airway data to the model structure of the lung space and the recalculation of the volume per generation per shell, which is now modified. The first 5 generation distinct airways that are provided by the CT dataset are superimposed to the lung space, which has previously been divided into shells, and the volume of each generation is measured with reference to the corresponding shells. The CT images have already been shown to be in alignment with the MRI images (Figure 4-3) so no further registration is necessary. The process is again performed for each lung separately.

Table 4.1 now needs to be adjusted to reflect the existence of the new data involved in the process. The information on the first five generations is omitted and then renormalisation of the remaining data takes place. The original dataset had been normalised to a standard 3.3l FRC for comparison and validation purposes. However, since current work is carried out on each lung individually, the dataset has to be renormalized to produce two tables, one for the left and one for the right lung. For this to become possible the portion of the organ comprised of the left and the right lung needs to be calculated. The tabulated data are multiplied with the two factors representing the volume of each lung as a percentage of total organ volume and then they are stored into two individual tables. The first 5 generation data are then filled in to complete the datasets. The results are displayed in Table 4.3(a) and (b), and they are validated with the help of the graphs in Figures 4-8, 4-9 and 4-10.

Generation number	Shell number										Total
	1	2	3	4	5	6	7	8	9	10	
1	0.21	0.06									0.27
2	0.68	0.48									1.16
3	0.01	1.14	0.67								1.83
4			0.78	0.33	0.03						1.14
5		0.1	1.75	0.61	0.09	0.01					2.56
6		0.02	0.09	0.3	0.56	0.70					1.68
7		0.01	0.06	0.14	0.37	0.65	0.51				1.74
8		0.01	0.02	0.10	0.24	0.33	0.7	0.25			1.66
9			0.02	0.06	0.12	0.34	0.53	0.56			1.63
10			0.02	0.06	0.13	0.21	0.34	0.75	0.41		1.93
11			0.01	0.06	0.19	0.28	0.42	0.61	0.83		2.39
12			0.01	0.05	0.1	0.32	0.58	0.8	1.22		3.07
13			0.01	0.06	0.12	0.25	0.43	0.67	0.99	1.34	3.86
14			0.01	0.06	0.13	0.28	0.47	0.73	1.00	1.43	4.1
Acini		3.6	13.5	37.1	72.9	128.3	188.1	263.4	343.8	440.2	1490.8

(a)

Generation number	Shell number										Total
	1	2	3	4	5	6	7	8	9	10	
1	0.29	0.27	0.11	0.1	0.06					0.08	0.93
2	1.14	0.06	0.08	0.02							2.4
3		0.21	0.57	0.04							0.82
4		0.13	0.83	0.54	0.06						1.56
5			0.26	0.94	0.34						1.54
6		0.03	0.1	0.35	0.66	0.83					1.96
7		0.01	0.07	0.17	0.45	0.76	0.6				2.03
8		0.01	0.03	0.12	0.29	0.39	0.81	0.3			1.94
9			0.03	0.07	0.14	0.4	0.62	0.66			1.91
10			0.03	0.08	0.16	0.25	0.4	0.88	0.48		2.27
11			0.01	0.08	0.22	0.32	0.49	0.71	0.97		2.81
12			0.01	0.05	0.12	0.37	0.67	0.93	1.44		3.6
13			0.01	0.07	0.14	0.3	0.5	0.79	1.17	1.56	4.53
14			0.01	0.07	0.16	0.32	0.55	0.85	1.18	1.68	4.81
Acini		4.2	15.8	43.5	85.4	150.3	220.4	308.7	402.8	515.9	1747

(b)

Table 4.3: The volume per generation per shell (V_{ij}) with real anatomical data in the first 5 generations for (a) the left and (b) the right lung. All values are in ml.

Results

The space contained within each lung was first measured with reference to the number of the voxels included in the lung area, which is calculated through examination of the MRI dataset. The left lung was found to occupy 43.4% of the total lung volume while the right lung occupied the rest 56.6%. These values fit the profile of lung anatomy described in the 2nd Chapter, according to which the right lung must be larger in size than the left one.

Figure 4-8 illustrates the total volume per generation corrected for lung size for the advanced conceptual model, the hybrid conceptual model algorithm presented above and compares them with data obtained from a CT scan on a lung cast. The CT scan data of the lung cast were obtained from Sauret et al. (2002) and were provided to us by Professor J. S. Fleming, Department of Medical Physics and Bioengineering, Southampton University Hospital NHS Trust. Since only the first 8 generations of the airway tree cast were available, the outer boundary of the lung was defined as the cast envelope dilated by 5mm to allow for the alveolated airway information missing from the dataset. All values were also normalised to the standard 3.3l FRC. It can be seen that only hybrid model provides information for the first generation, i.e. the quantity of the main bronchi that penetrate into the lung pace. It is also obvious that the hybrid model follows closely the average model from generations 6-12, with only small differences in the order of a few hundredths of an ml. This is because the values of volume per generation per shell derived by the advanced conceptual model were used as a foundation for this algorithm. However, considerable differences, in the order of 1ml, are present in the first 5 generations between the two models and the CT cast data. It can easily be observed that the CT airway data provide almost consistently higher values throughout their range of availability. Furthermore, the variation between the two models is much greater in the first three generations, where the *in-vivo* data are being implemented.
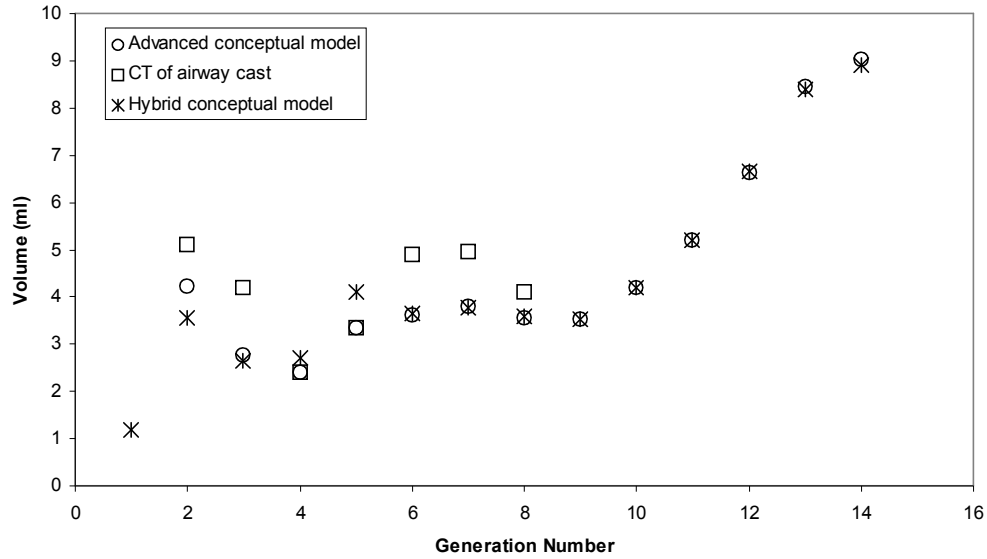
Figure 4-8: Volume per generation for the advanced conceptual model, the hybrid conceptual model and a CT scan of the airways of a lung cast.
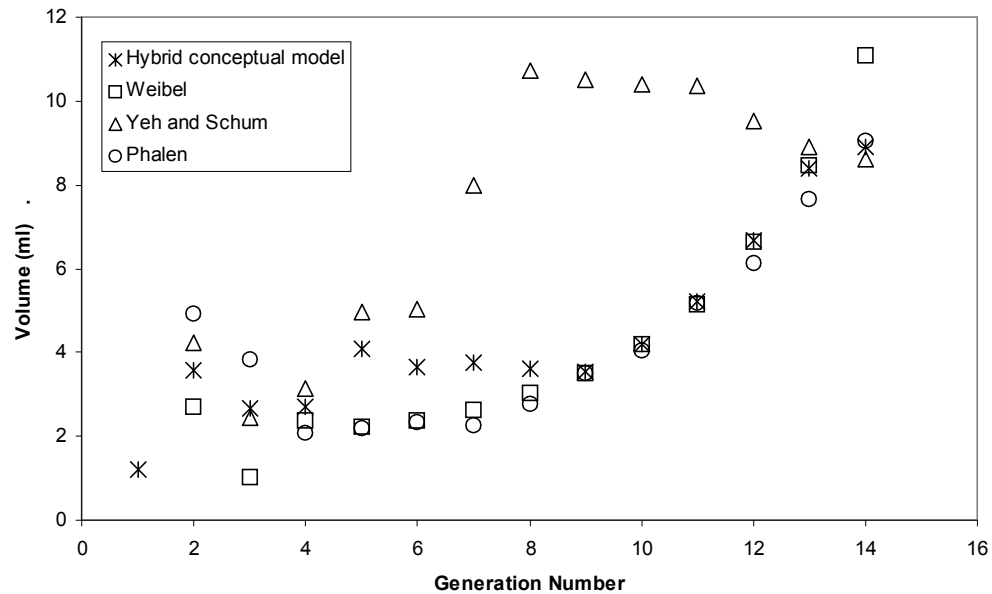
Figure 4-9: Comparison of volume per generation for the hybrid conceptual model and the models presented by Weibel (1991a), Yeh and Schum (1980) and Phalen et al (1978).
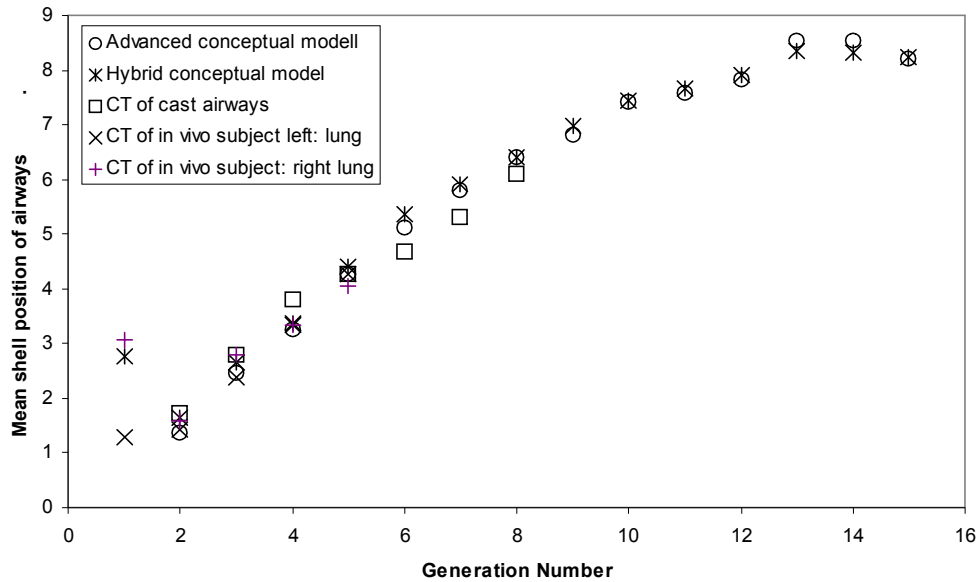
Figure 4-10: The mean shell position of airways for the advanced conceptual model, the hybrid conceptual model, the airways of the CT scan of the lung cast, the *in-vivo* input CT data of the left and the right lung.

The volume per generation corrected for lung size for various models described in the literature is compared to the hybrid conceptual model in the graphs of Figure 4-9. The Phalen et al. (1978) and Weibel (1991a) models are similar for the airway generation range 5-12 whereas the Yeh and Schum (1980) data are quite different, having considerably increased volumes between generations 7 and 12. The hybrid conceptual model follows very closely the Weibel model from generations 8-13 but the first 6 generations, which include the *in-vivo* data, correspond better to the Yeh and Schum model. Still, huge differences in the order of several ml exist between the Yeh and Schum model and the other three models.

Finally, Figure 4-10 illustrates the variation of mean shell position with generation for the hybrid and the advanced conceptual models and the CT cast data. In addition, the *in-vivo* CT scan airway data that were analysed in the previous section were investigated to find the exact physical mean shell position of the first 5 airway generations. To obtain a larger sample, the results of the left and the right lung are again displayed separately. Except

104

for the first generation, which has really diverse mean shell position values, the similarity between the models, the *in-vivo* and the cast CT data is striking.

Discussion

The inter-subject variation in generation volume is demonstrated in Figure 4-8. It is mentioned above that, though the hybrid model follows closely the advanced model from generation 6-14, there are certain differences in the first five generations, where the *in-vivo* data of the hybrid model are used. These differences, though not particularly big, indicate a strong inter-subject variability factor that must be taken into account when modelling the lungs. This factor is even more pronounced when comparing the CT scanned cast data with the data generated by the other two models. The fact that the hybrid model makes use of real airway anatomical data enables it to represent this inter-subject variability much more accurately than the average model. This is one of the great improvements of the hybrid model over the advanced conceptual model.

The comparison of values for volume per generation of the conducting airways for the hybrid model, the advanced model and the other three literature models shows that only the hybrid model can provide information on the amount of generation 1 volume that lies within the lung space. This constitutes an important advantage of the hybrid model as the previous conceptual models either over- or underestimated generation 1. In addition, it is shown in Figure 4-9 that the hybrid model tracks the Phalen and the Weibel models in high numbered generations of the conducting airways but the *in-vivo* data are closer to the Yeh and Schum values. It is difficult to speculate whether this represents typical inter-subject variation or not. This question can only be answered after the comparison of several in-vivo CT scans of the human airway tree, even though these will only provide information on generations 1-9 and it is generations 9-Acini that that the variability is the greatest.

When the mean shell position of each generation is compared between the hybrid and advanced conceptual model and the CT scan of the cast data, the only important discrepancies exist around generation 1. Other than that, the data of all methods follow similar patterns and the values of mean shell position are very close to each other. This implies that though neither of the models includes information about the spatial location of individual airways after generation 5, they can be safely employed in applications demanding accuracy in the calculation of airway depth in the lung. The large disparities in the first generation can be attributed to uncertainties introduced during the determination of the hilum position in the advanced model, the most important of which is the incorrect assumption that the hilum occurs at the bifurcation of the main bronchi.

4.3.4 Interpolated Airway Distribution

Methods

As mentioned earlier, both the original and the advanced conceptual model assumed an even distribution of each volume per generation per shell V_{ij} throughout each shell. The next goal of this study is to produce a better, more realistic distribution of the values of V_{ij} in every shell for the generations where no real anatomical data exist. First, the volume of each generation contained by the voxels of each shell (VVoxel$_{ij}$) has to be calculated. This is done by applying equation (4.2) to all voxels in the space of each lung using the values obtained in Tables 4.3(a) and (b). The current distribution resulted in abrupt and, therefore, abnormal changes in air distribution at shell boundaries. To obviate this, an interpolation scheme that employs the fractional distance ratios calculated earlier is devised and used for all subsequent computations.

According to this method, the only voxel values calculated with the help of equation (4.2) were the voxels with fractional distance ratios representing the middle of each of the 10 shells, i.e. with R=(0.05, 0.15, 0.25 … 0.95). It has to be noted that, since the dataset is discrete, it is possible that no such

created with
nitro^PDF professional
download the free trial online at nitropdf.com/professional

actual voxels exist. What is done here is essentially the association of an airway volume for a specific generation to a fractional distance ratio (Figure 4-11(a)). After that, a separate graph is produced for each generation, matching the airway volumes in all voxels to the voxels' values of FDR in a discrete manner. In this sense, the air volume is considered to be a function of fractional distance $V_j(R)$ and this is used to implement the interpolation process. Two algorithms, one producing linear and one producing spline interpolation, are applied to these graphs to make the final dataset continuous in nature. These two graphs are displayed in Figure 4-11(b) and (c) respectively.

Some important assumptions have to be pointed out here. First all generations are considered to have zero volume at zero fractional distance, except for generation 1 which must have maximum volume. Also, the distal part of shell 10, i.e. voxels of the lung space with fractional ratios R>0.95, is assumed to contain only acinar structures. The acini voxel volume densities at voxels on the lung surface (R=1) are calculated using the calculated mean acini airway density of the 4 voxels in the middle of the previous 4 shells. This is given by the equation

$$V_{15}(1) = \frac{V_{15}(0.65) + V_{15}(0.75) + V_{15}(0.85) + V_{15}(0.95)}{4} \quad (4.8).$$

Negative voxel volumes generated by the spline interpolation algorithm are avoided by converting the graphs to their absolute value equivalents. It was decided that, for the purposes of this study, the linear implementation of the method produced the better results and, for that reason, the rest of the process was based only on linear interpolation.

The fractional distance of every lung voxel was then compared to the graph for each airway generation and the voxel was assigned the estimated value of airway density per generation based on the graph results. These voxel values are then stored to independent 3D matrices with dimensions equal to the input data at voxels with the same coordinates as the voxel in question. Thus 10 versions of the lung are filled with the interpolated airway generation

volumes. The initial 5 generations of the CT data do not need to undergo this process as their locations are already known.

Results

The graphs of Figure 4-11 display the interpolation process of airway values for the whole range of fractional distance ratios. It can be observed in graph (c), which represents the spline interpolation algorithm results for the airways of generation 11, that there are some peaks between 0 and 0.25 fractional distance, where no presence of generation 11 airways is anticipated. A similar effect occurs at the range between 0.95 and 1, which represents the distal part of the lung where only acini are expected to exist. These two effects show that the interpolation is based on a rather sparse dataset, which is the reason why linear interpolation is selected as the algorithm of choice.
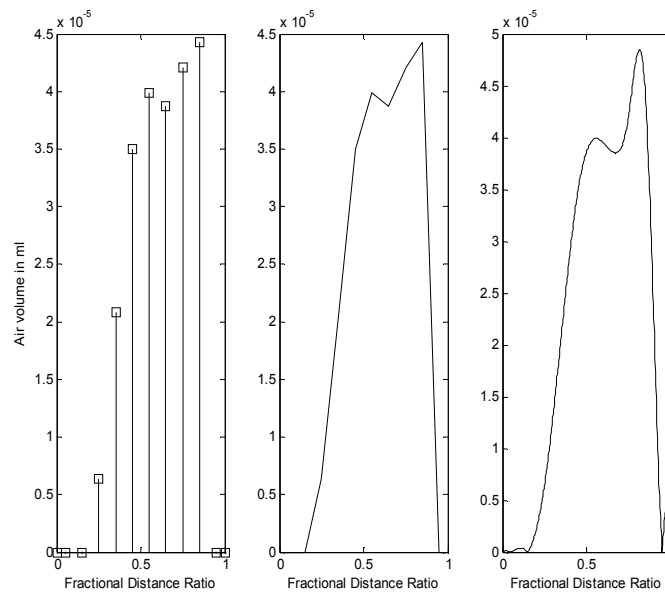
Figure 4-11: The three graphs representing the interpolation process of the air volumes of generation 11 airways in the whole organ space. Image (a) shows the calculation of the mid-shell theoretical airway values while (b) and (c) display the linear and the spline interpolation respectively.
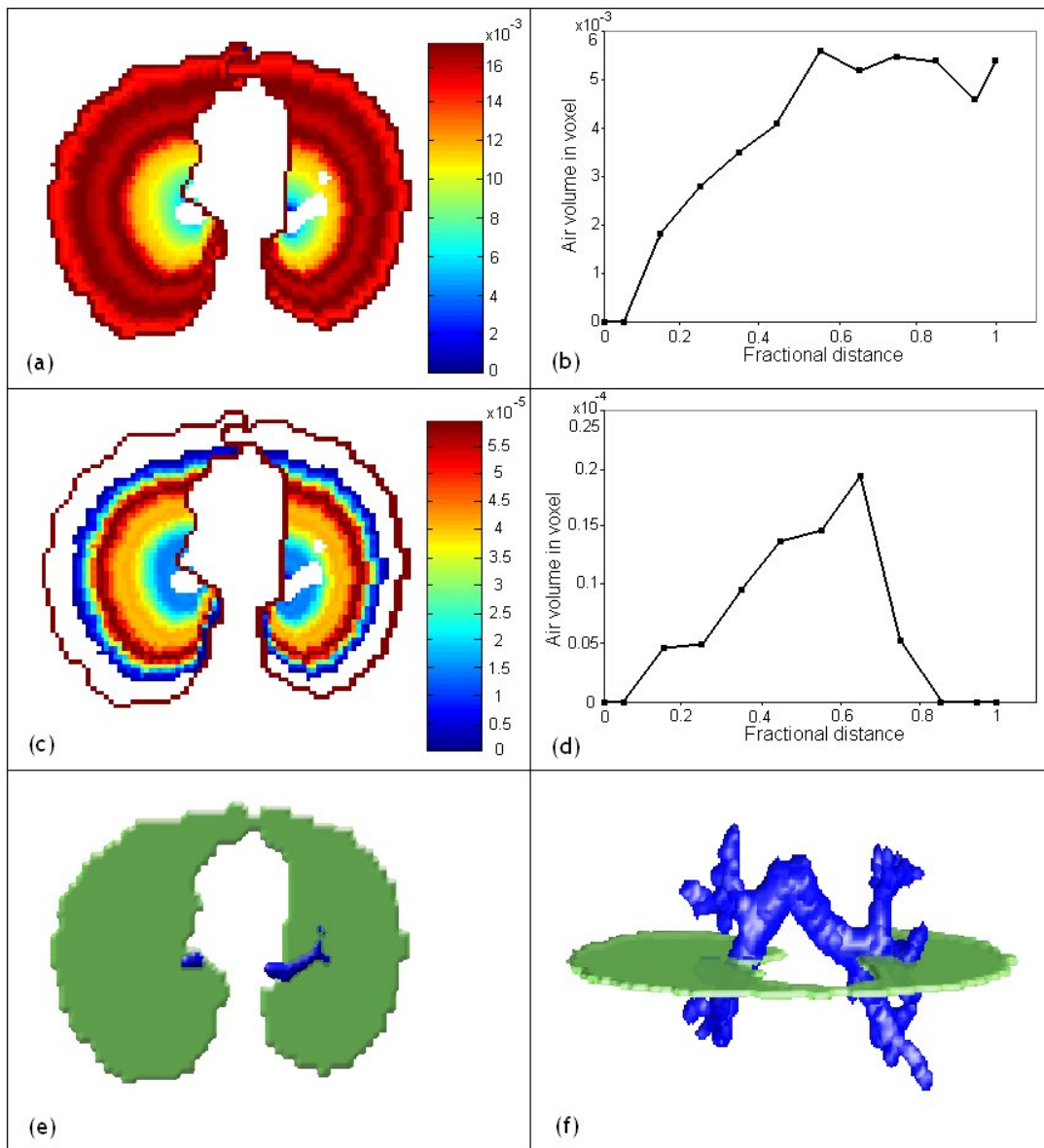
Figure 4-12: A 2D representation of the hybrid conceptual model. Images (a) and (c) display a transverse slice of the calculated acinar and generation 8 airway volume, associated to the fractional distance ratio through the graphs in (b) and (d) respectively. Images (e) and (f) display the treatment of the known airway generations in the model.

Figure 4-12(a), (c) and (e) show a colored representation of the hybrid conceptual model for a single transverse slice of the lung space. The slice where the hilum of the left lung occurs is selected for this representation. The first two images display the acinar and generation 8 airways respectively, while image (c) shows a single transverse slice of the lung space with airways obtained from the CT data superimposed on it. A 3D illustration of this can be seen in Figure 4-12(f). The space occupied by the first 5 generations is left blank in images (a) and (c) since the voxels that are included in the composition of the physical airways of the model cannot contain air volumes that belong to the bronchi of other generations. The colorbars on the right of these images associate color with air volumes, calculated in ml. Finally, images (b) and (d) are the interpolated graphs related to the acini and generation 8 respectively. A small drop in the air volume per voxel is displayed at the position with fractional distance ratio 0.95 in graph (b), which is of the magnitude of 15% as suggested during the discussion of Section 4.3.2.

Discussion

Generic models of the lung are useful in providing estimates of airway anatomy. However, it is widely accepted that there is considerable individual to individual variation in lung morphology, which is demonstrated in the results of Section 4.3.3. Therefore, there are inevitable limitations on the accuracy of generic models. This section has demonstrated a method of adopting an existing generic model to a specific individual using measurement data on the actual airway structure of the first few generations.

Generally speaking, the hybrid conceptual model has two major advantages over its predecessor. The first one is that it uses real anatomical data provided by CT scans to customize it according to the anatomy of each subject. The second major advantage is the improvement of the airway volume distribution throughout the part of the lung space where no real anatomical data exist. This addition gives the model a more lifelike quality,

created with
nitro^PDF professional
download the free trial online at nitropdf.com/professional

thus increasing its usability in clinical applications and its compatibility to other, mostly deterministic, models.

The next step in this line of research, as far as the hybrid conceptual model is concerned, is the validation of the model's results with the help of radionuclide imaging. This has to be done in order for the hybrid model's practicality to be completely established with respect to aerosol deposition in the lungs. Another goal that should be pursued is the enhancement of the accuracy of the model by trying to incorporate more generations of real airways to its structure. Finally, further work should include efforts for the better localization of the interpolated airway generation volumes. It can be seen from Figure 4-12 that the airway volumes, though more elaborately dispersed within the lung volume, still follow a radial distribution pattern. This pattern could be improved with the implementation of the process described in this chapter on subspaces of the lung, such as the lobes or the segments, thus producing a more lifelike and, therefore, more useful generic representation of the human airway tree.

4.4 Conclusion

This chapter introduced a different approach in the implementation of the conceptual model, improving the airway distribution between different shells and introducing in vivo data in the realization of the model. Methods for the generation of the model were presented and their results were shown to compare well. In relative terms, the generation volume of the hybrid conceptual model is very similar to the advanced model and, indeed, with the ICRP model of 1994. However, the improved modeling of generations 0-5 should lead to reduced errors when using it to estimate deposition per generation. Still, the hybrid model provides data in a different form than the average conceptual model. It describes each generation by a 3D distribution of volume rather than of discrete volume in each shell. This will require new

algorithms to be developed for the derivation of deposition per generation values.

The hybrid model can be used instead of the advanced conceptual model and in conjunction with radionuclide imaging to give good measurements of deposition per airway generation in the lung. As CT scanning techniques advance, it will be possible to integrate even more in-vivo airway data in the model, thus improving its performance and reducing the discrepancies involved in its application. However, the hybrid model remains generic in nature and, hence, inappropriate for use in certain applications. The creation of a fully 3D deterministic model of the human airway tree will be the matter of investigation in the following chapters. Still, prior to that, and for reasons that will become apparent in the next chapter, a method for dividing the lung into its constituting subspaces (bronchopulmonary segments) will have to be created and the Hybrid Conceptual Model will have to be adjusted to the new lung space, thus forming the Segmental model of the lung space and the resulting Segmental Hybrid Conceptual Model.

Chapter 5
Division of the lung into segmental subspaces

5.1 Introduction

The objective of this chapter is the development of a method for the purpose of dividing the lung space into realistically spaced and shaped subspaces, which can then be used as a template for the development of new deterministic airway tree models. This course of action becomes necessary for two main reasons: Primarily, to increase the accuracy of the newly developed models since a more localised airway tree geometry has to be followed and satisfied for the new template and, secondarily, to economise on the available resources such as computer power and time. Additional advantages of this approach are its originality, since, to the best of our knowledge, only larger templates have been used in the literature so far, and the development of the method for dividing the space in itself, since, again, the literature is extremely lacking in such efforts [Sauret PhD Thesis, 2000, Fleming et al. (2004b), Busayarat et al. (2007)]. Given that, as seen in Chapter 2, the lung is already divided in biological subspaces such as the bronchopulmonary lobes and segments, the algorithm described in this chapter will have as a goal to describe the subdivision into bronchopulmonary segments, thus forming the Segmental Model of the lungs.

In the rest of this chapter, first the lung morphology will be briefly revisited and the bronchopulmonary segments introduced. Each step of the new Segmental Model algorithm will then be presented and the algorithm's results will be discussed. Following that, some of the disadvantages inherent to the new algorithm will be addressed with the creation of a descriptive morphometric Segmental Atlas. Finally, the Hybrid Conceptual Model generated in Chapter 4 will be modified to fit the new segmental space division, this resulting to the formation of the Segmental Hybrid Conceptual Model (SHCM).

5.2 Lung Morphometry Revisited

As seen in Section 2.3, the human lungs are divided in some discrete spatial units, the bronchopulmonary lobes. These are surrounded by pleural tissue and can readily be identified in-vivo via CT imaging. The right lung consists of 3 lobes, the Right Upper (RU), Right Middle (RM) and Right Lower (RL), while the left lung consists of only 2 lobes, the Left Upper (LU) and Left Lower (LL). The lobes, in turn, can be further sub-divided into bronchopulmonary segments, 10 in number for each lung. These cannot be readily identified in-vivo since they are not surrounded by any material envelope. Hence, in clinical applications where the localisation of pathology is necessary, the identification of the segment contours is usually done by experts who detect proximate segmental bronchi through knowledge of the lobes and the lobar bronchi, since these characteristics usually define segment location and orientation, as well as with the use of empirical knowledge.

The segments of both lungs can be observed in the image of Figure 5-1, which exhibits a resin cast of the human lung with the different segments, as identified by expert biologists, displayed in different colours. This lung cast, henceforth referred to as the departmental cast, consists of the first 10 generations of the airway tree and access to it was provided by Professor J.S. Fleming, Department of Medical Physics and Bioengineering, Southampton University Hospital NHS Trust. For the right lung , the RU lobe consists of 3 segments, the Apical (S1, brown), the Posterior (S2, cyan) and the Anterior (S3, pink), the RM lobe contains the Lateral or Superior Lingular (S4, red) and the Medial or Inferior Lingular (S5, black) segments, while the RL lobe comprises of 5 segments: The Superior (S6, green), the Medial Basal (S7, yellow), the Anterior Basal (S8, orange), the Lateral Basal (S9, alcohol blue) and the Posterior Basal (S10, cabbage green). For the left lung both lobes consist of 5 segments, since the two segments that belong in the RM lobe (S4 and S5) are now an integral part of the LU lobe and are given the name Superior Lingular and Inferior Lingular. It has to be noted that, in the left

created with
nitro^{PDF} professional
download the free trial online at nitropdf.com/professional

lung, the pairs of S1 and S2, as well as S7 and S8, are, on occasion, considered to form a single segmental unit.

Figure 5-1: Photograph of the cast with the segmented airways in painted in different colours.

5.3   Segmental Model Algorithm Step By Step

From visual observations of the segmented lung cast, it is obvious that, although there is great variability of size and shape between different segments, they tend to maintain a roughly conical form. The algorithm presented in this section is designed to take advantage of this common characteristic. Furthermore, previous models of the segmental space have all been, in essence, simulations of the "fight for space" process that is believed to take place in the pre-natal stages of lung development. Both Sauret (PhD thesis, 2000) and Busayarat et al. (2007) make an effort to locate the "ignition" position from which to perform a dilation (space-filling) procedure.

created with
nitro PDF professional
download the free trial online at nitropdf.com/professional

Both previous efforts also use as initial conditions an MRI and a CT dataset in order to define the constraints imposed on lung space and the first few generations of the tracheobronchial tree. The Segmental Model algorithm described here is basically an adaptation of these methods.

The data necessary for the development of the Segmental Model, were again supplied by Professor J. S. Fleming, Department of Medical Physics and Bioengineering, Southampton University Hospital NHS Trust. For more information see Section 4.3. These data are, as stated in the previous paragraph, a CT scan of the airways and an MRI scan of the lung space of a human subject. In addition, a space erosion process was initially carried out on the results of the CT scan and the skeleton version of the CT data was also provided along with the raw data of the scan. The algorithmic process used for the creation of the Segmental Model can be broken down into 4 discrete steps: First, the data need to be properly aligned and formalised. Then the segmental root airways are introduced and investigated with respect to their relative positions in the CT dataset. An extension of these airways in performed towards the edge of the lung and the line generated is then used for a space filling process. This process can be summarised in the following diagram:

INPUT: MRI and CT images, skeletonised form of the CT data.

↓

Airway data alignment and tabulation

Segmental root airway detection

Lung edge detection

Space-filling application

↓

OUTPUT: One 3D matrix of the human lung space, each voxel in the matrix displaying affiliation to specific segment

116
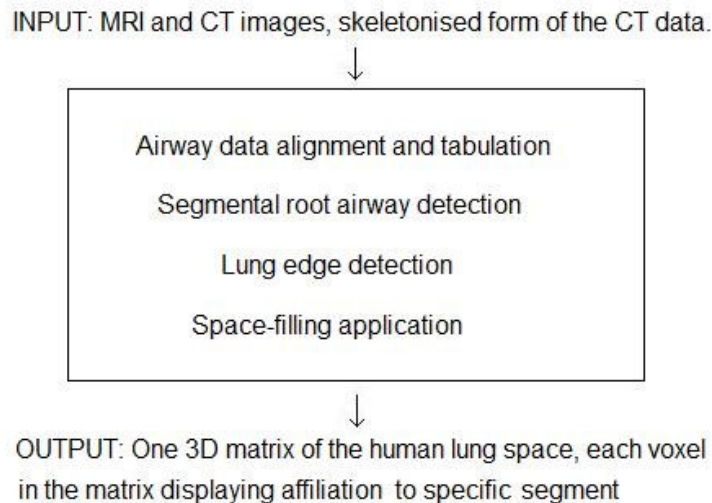
5.3.1 Airway Data Alignment And Classification

The first step of the algorithmic procedure is, essentially, a preprocessing step, since it involves the formalisation of the available input data. As mentioned in Section 4.3.1, the CT data come in the form of 5 3D matrices with 128 elements in each linear dimension, each element representing the air volume of the airways of the generation contained in the voxel in question (Figure 4-2 (c) and (d)). On the other hand, the skeletonised form of the CT dataset comes in as a set of coordinates in the following arrangement:

ID number	Generation number	x_{start}	y_{start}	z_{start}	x_{end}	y_{end}	z_{end}	Diameter, (mm)

where the ID number is a binary number that consists of a number of elements equal to the generation number of the airway plus 1 and is unique for each airway, and the $(x_{start}, y_{start}, z_{start})$ and $(x_{end}, y_{end}, z_{end})$ are the coordinates of the start and end nodes of each airway. Since, as shown in Chapter 4, the CT airway data and the MRI lung space data are already aligned (Figure 4-3), any use of a misaligned skeleton set would render the rest of the process problematic. For that reason, the proper alignment of all available data has to be ensured before the process continues.

The original data position and size can be observed in the image of Figure 5-2. It is obvious from this image that both resizing and displacement of one of the two datasets is necessary. The dataset on which the operations were performed was the skeleton coordinates because it is easier to manipulate than the voxel elements. The method used was to try and find a relationship between the CT data coordinate system and the skeleton coordinate system. In order for this to become possible, a correlation of at least 3 points between the two systems has to be made. The biggest issue in this method is that, though the node coordinates for the skeleton are conclusive, similar coordinates are not available for the CT scan, mainly because of the discrete nature of the data, which allows for several different airways to occupy portions of the same voxels, thus introducing ambiguities.

created with
nitro^{PDF} professional
download the free trial online at nitropdf.com/professional

In order to counteract this, the common voxels between consecutive generations were located and the air volume of both generations in these voxels was calculated. The branching point between the two consecutive airway generations is selected as the voxel which satisfies two conditions: The airway volume of the voxel must be shared in equal proportions by both airway generations and, at the same time, the voxel must contain the highest overall volume possible, which is 64 (see Section 4.3.1 for more details). Although an automatic method for fulfilling these criteria would be preferable, the optimal detection method would entail the application of fuzzy logic or neural network systems, hence a less time-consuming manual approach was selected. An example of how this selection is done can be seen in Table 5.1 (the selected voxel displayed in red).
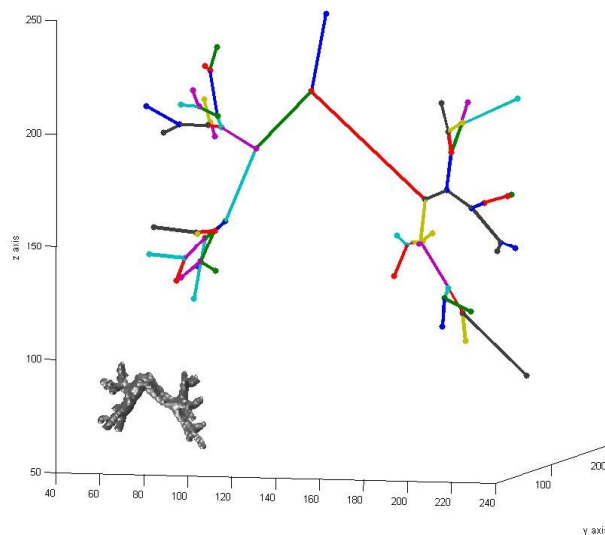
Figure 5-2: The original skeleton and CT datasets. The eroded airways are displayed in different colours for easier distinction between them.

118

Three points are necessary for the investigation on the fitting of the two datasets, one used as the origin point from which all measurements will take place and two more points, preferably as instantly recognizable as possible. The three points selected to perform these roles were the node connecting the trachea to generation 1 airways and the two nodes connecting generations 1 and 2.

Volume in Generation 1	Volume in Generation 2	x coord.	y coord.	z coord.
11	34	59	60	81
7	57	59	61	81
36	17	60	60	81
30	34	60	61	81
23	41	60	62	81
44	4	61	60	81
54	10	61	61	81

Table 5.1: The nodal voxel selection process. A list of candidate voxels is given and the selected voxel is displayed in red. The maximum volume in each voxel cannot exceed number 64.
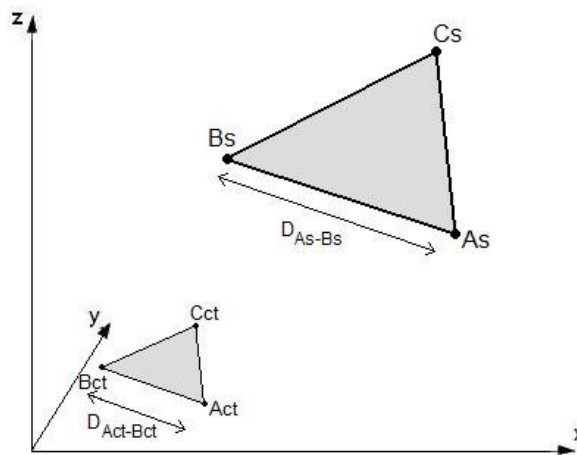
Figure 5-3: The calculation of the resizing factor in the alignment process is based on the two triangles formed that have as edges the nodes of generation one airways.

Two triangles connecting these points were formed, one for the skeleton (triangle $A_SB_SC_S$) and one for the CT data (triangle $A_{Ct}B_{Ct}C_{Ct}$, Figure 5-3). The distances D_{As-Bs} and $D_{Act-Bct}$ between these points were then calculated and a resizing factor

$$F = \frac{D_{As-Bs}}{D_{Act-Bct}} \quad (5.1),$$

expressing the difference in size between the two datasets was estimated. The whole skeleton coordinate system is then divided by this resizing factor in order to bring the eroded airway network to a size comparable to the airways represented by the CT data. The points forming the skeleton triangle then migrate to the coordinates given by the equation

$$\left(As_{new}, B_{Snew}, C_{Snew}\right) = \frac{(A_S, B_S, C_S)}{F} \quad (5.2).$$
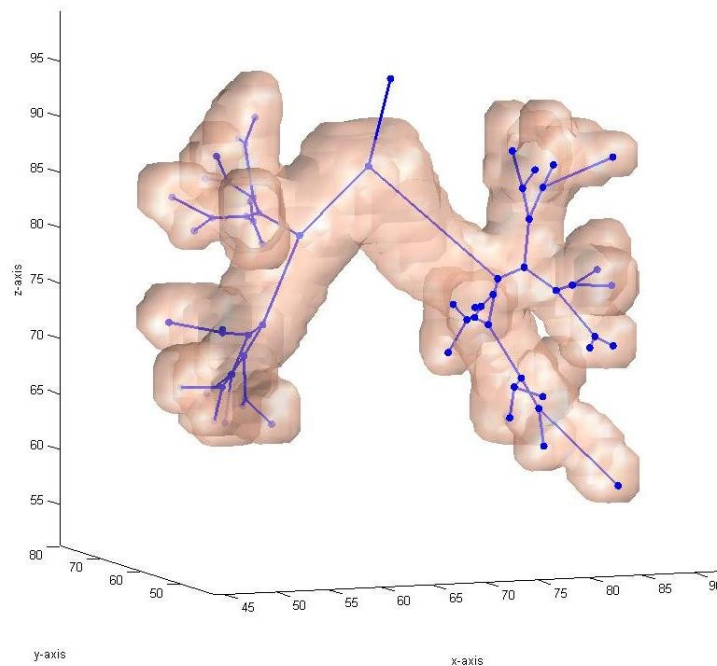
Figure 5-4: The first 5 generations of the human airway tree as displayed with the help of CT data and its skeletonised form. The blue dots represent the branching nodes.

The next part of the alignment process is the calculation of displacement factors of the skeleton set, one factor for each dimension. Two samples per dimension need to be used in order to achieve more accurate results:

$$\begin{cases} \Delta x = \dfrac{(x_{Act}+x_{Bct})}{2} - \dfrac{(x_{Asnew}+x_{Bsnew})}{2} \\[2mm] \Delta y = \dfrac{(y_{Act}+y_{Bct})}{2} - \dfrac{(y_{Asnew}+y_{Bsnew})}{2} \\[2mm] \Delta z = \dfrac{(z_{Act}+z_{Bct})}{2} - \dfrac{(z_{Asnew}+z_{Bsnew})}{2} \end{cases} \quad (5.3).$$

The resized skeleton system is then displaced to its final coordinate position by adding the displacement factors to the coordinates of each dimension separately. The final results of the alignment process are displayed in Figure 5-4. It is obvious that the skeleton follows with very good accuracy the centreline of the airways represented by the CT data, which was the goal of this section. The method described above is relatively easy to follow and uses simple principles to tackle a relatively complex problem. Increased accuracy could be achieved by increasing both the skeleton data points in order to induce the effects of curvature, as well as by increasing the samples used for the calculation of the displacement factors.

Having performed the data alignment, it is now possible to proceed to the next step of the algorithm.

5.3.2 Segmental Root-Airway Detection

This section is concerned with the qualification and quantification of which portions of both available airway datasets (CT and skeleton) are constituent parts of which segments. This is done not only because the segmental bronchi define the orientation and position of the whole segmental space but also because our method for selecting the initial conditions for the implementation of the space-filling process, which is the subject of the next two sections, is heavily dependent on the positioning of the segmental airways.

created with
nitro PDF professional
download the free trial online at nitropdf.com/professional

The segmental airways are defined as all the airways that individually penetrate into the segmental space. These airways are daughters of the first, second or third degree of the lobar airways and form the roots of the sub-tree structures that fill up the segmental sub-spaces of the lung. Since there are 10 segments in each lung, the segmental roots may be airways of the 3rd, 4th or 5th generation, with the trachea considered generation 0. This type of variation makes automatic identification of segmental roots very difficult. For that reason, an alternative approach was selected.

The detection of the segmental-root airways in the CT and skeleton data was performed based on the relative positioning of the skeleton with reference to the departmental cast (shown in Figure 5-1). Therefore, there are two criteria for determining if an airway of the CT data is, in fact, the root of a segment. The first one is the generation it belongs to and the second one is its position, mainly relative the lung space and secondarily with respect to the tree structure. For example, the Right Upper Anterior segment (S3, pink), as displayed in the departmental cast, must begin with an airway in generation 3. Furthermore, the root must have an orientation toward the upper and frontal part of the lung, which is the region of the lung the specific segment supplies. Extrapolation of these conditions on the airway datasets made the selection of the root airway S3 possible. The same type of extrapolation was repeated for all segments of both lungs and the CT airways were associated with the relevant segments. The results of this process are displayed in the image of Figure 5-5, where the segmental airways and their daughters are pictured in colours relevant to the ones linked to each segment in Section 5.2.

Figure 5-5: The skeleton of the airway tree divided into segments. The blue lines in the skeleton are pre-segmental airways, i.e. airways that don't belong to a segment.

5.3.3 Lung Edge Detection And The Implementation Of A Space-Filling Method

One of the greatest difficulties imposed when trying to model the bronchopulmonary segments with the use of space-dilation techniques is the selection of the initial positions where the "fight-for-space" has to begin from. The logical position of these initial points would be the centres-of-mass of each segment. However, the selection of centres-of-mass has two inherent disadvantages: Primarily, they are only available through the use of anatomical atlases which, due to the huge variability in the location and size of the lung structures, make them inappropriate for the generation of accurate, patient-specific models. In addition, the lung segments are not only space- but also shape-restricted, since they have to maintain a conical form. This cannot be accomplished with the use of singular points as initial conditions for the space-filling process.

123

created with
nitro^PDF professional
download the free trial online at nitropdf.com/professional

Sauret (PhD thesis, 2000) selected as such initial conditions the spaces already known to be occupied by the segments. This was done with the help of the airways extracted from a CT scan and their allocation to specific segments. Busayarat et al. (2007) used a similar method that also used the segmental airways. The method described in this section only makes use of the segmental roots, already identified in the previous section, and the confining surface of the lungs, found via MRI imaging.

The initial positions with respect to which space dilation is implemented are selected as follows: First, for each segmental root airway a vector

$$\vec{v} = [end\ point] - [start\ point]\ (5.4),$$

beginning at the start point with coordinates (x_{start} y_{start} z_{start}) (Section 5.3.1), is calculated (Figure 5-6 (a)). A line following the vector's direction is then extended toward the edge of the lung. This line has as starting point the end-point of the relevant segmental root and is, in itself, an accumulation of equally spaced samples. The samples **s** are taken in the same direction as the vector $\vec{v}$ and are calculated as the addition of a portion of the unit vector $\vec{u}$ to the vector $\vec{v}$. The mathematical expression of the above operation is

$$\vec{s_j} = [x_{end}, y_{end}, z_{end}] + \frac{\vec{v}}{|\vec{v}|} * n * j \quad (5.5),$$

where j is the number of the samples taken, n is a constant defining the distance between consecutive samples and unit vector $\vec{u} = \frac{\vec{v}}{|\vec{v}|}$.

124
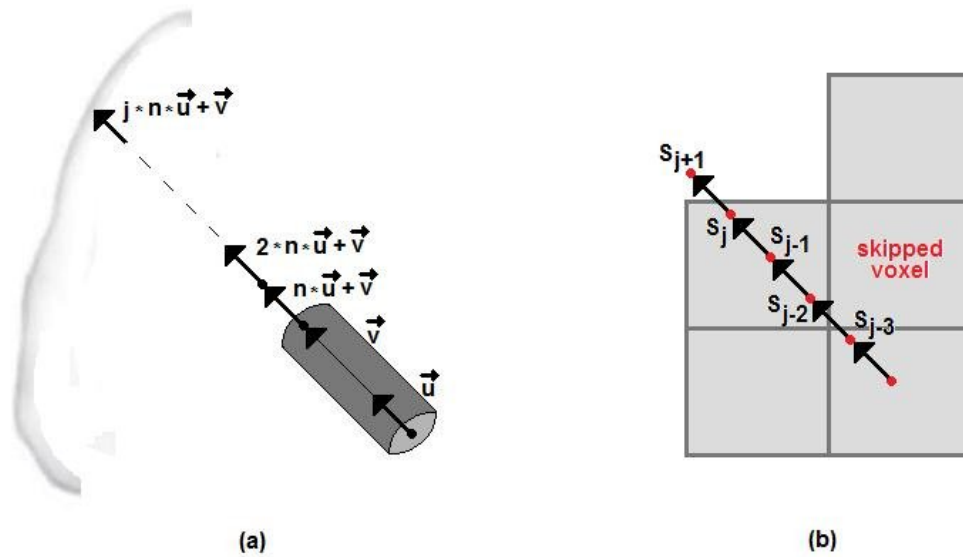
Figure 5-6: The edge detection process. (a) The vectors are calculated with respect to the skeleton line of the airway and samples are taken along the line until the edge of the confining space is reached. (b) Edge detection via abrupt change in voxel numerical value between consecutive samples **s**. A voxel that lies along the path of the extended line could be skipped if the distance between consecutive samples is too big.

Using the samples along the line, the edge of the lung space can now be obtained. This is done by detecting abrupt changes in the numerical values of the voxels defining two consecutive samples (Figure 5.6 (b)). Because of the discrete nature of this type of edge detection, a trade-off between the number of the samples and the certainty that all voxels in the path of the line have been taken into account has to be made. An increased sample rate would increase the certainty but would also be more computationally expensive. Since the voxel size of the MRI dataset is 2.8mm per linear dimension, a sample every 0.2mm is considered to produce sufficiently accurate results. The outcome of the edge-detection process can be observed in Figure 5.7.
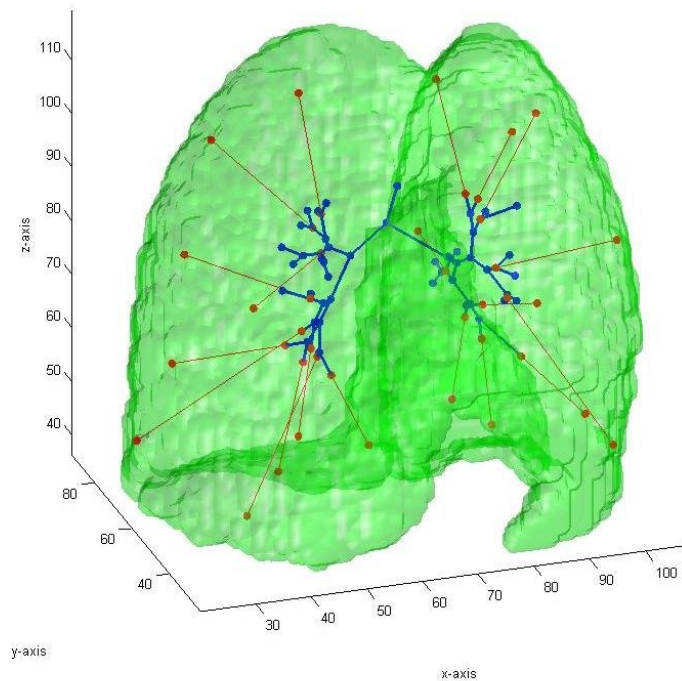
Figure 5-7: Results of the edge detection process. The airway skeleton is displayed with the blue lines, the segmental airways line extensions are shown in red and the red dots represent the selected points on the lung surface.

(a)   **(b)**
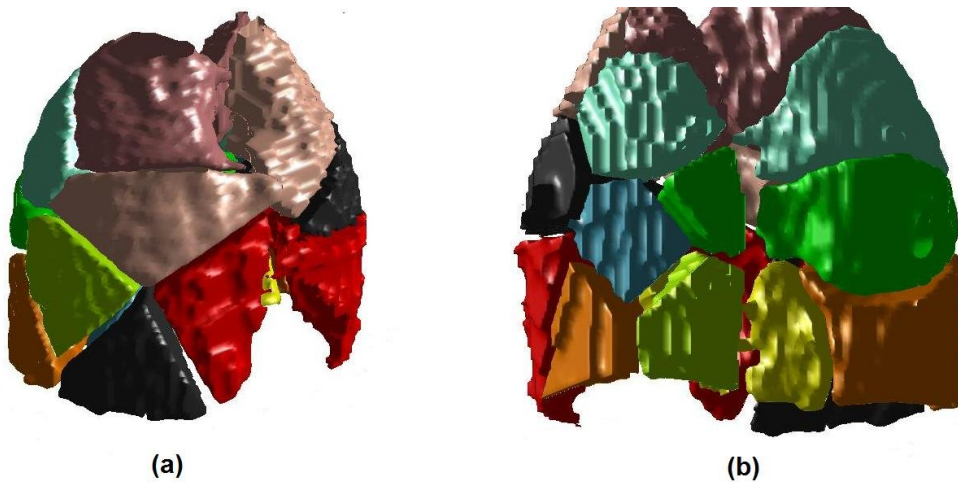
Figure 5-8: The Segmental Model of the human lungs. Two opposite views of the 3D model can be seen, (a) From the front and towards the right side and (b) from the back and towards the left side. The segments are colour-coded according to the association made in Section 5.2.

It was mentioned above that the bronchopulmonary segments maintain a, roughly, conical shape, which cannot be achieved in a model if space expansion is performed from singular points, since such methods are revealed to produce spherically-shaped spaces. However, if instead of a set of segmental points a set of properly oriented segmental lines is used, the optimal segment shape can be shown to be reasonably approximated. For that reason, a simultaneous space-filling process is performed with respect to the 10 segmental-root extension lines. Because these extensions are digital in nature, again a trade-off between number of samples and accuracy has to be made. After experimentation, 21 equidistant points along each extension line, including the segmental root end-point, were found to be adequate for the purposes of this study. Furthermore, these sample-points only need to extend to the line middle-point, since no rigid restrictions on shape are necessary for the distal regions of the lung. Using these sets of points, 21 for each of the 10 segments of each lung, a simple space-filling process is applied, where the distances between all voxels in the lung space and all the line samples are measured, and the voxels with the lowest distance to the sample of a specific segmental extension line is assigned a number representing a unique segment. The final results of the process can be seen in Figure 5.8.

5.3.4 Results And Discussion

The output of the segmentation process described in the previous sections of this chapter comes in the form of a 3D matrix with dimensions equal to the resolution of the original MRI data, which, in this case, are available in a 128x128x128 matrix. This resolution was considered to be optimal in a trade-off between the accuracy of the image and the resources necessary for its processing. Each voxel in the matrix of the model contains a number in the range between 0-20, each number from 1 to 20 representing the association of the voxel with a unique segment while number 0 stands for voxels outside the lung space. Because this format is very similar to the original MRI data, the Segmental Model can be immediately utilised in a number of applications

in which MRI scans of the lung were necessary. This can be done either in the model's current form or after its adaptation to a binary format, in which case each modelled segment has to be labelled and stored separately.

The image of Figure 5-8 allows visual comparisons between the predicted topology of the 20 modelled segments, the "real" segments that can be seen in the departmental cast (Figure 5-1) and topology as predicted by general atlases of the lung space. It can be observed that the Segmental Model follows very closely the positioning and orientation of the lung cast and is also in good agreement with a number of atlases of the segmental space. This is especially true for the Upper Lobes and segments S6 of both lungs, which seem to occupy regions of similar positioning and orientation. Additional validation of the topological accuracy of the model would include comparisons of the coordinate locations of the segments' centres of mass and evaluation of the mean outer-surface position in different segmental datasets. However, the huge inter- and intra-subject variability apparent in the human lungs, in addition to the lack of such data in the literature, made these types of comparison impossible.
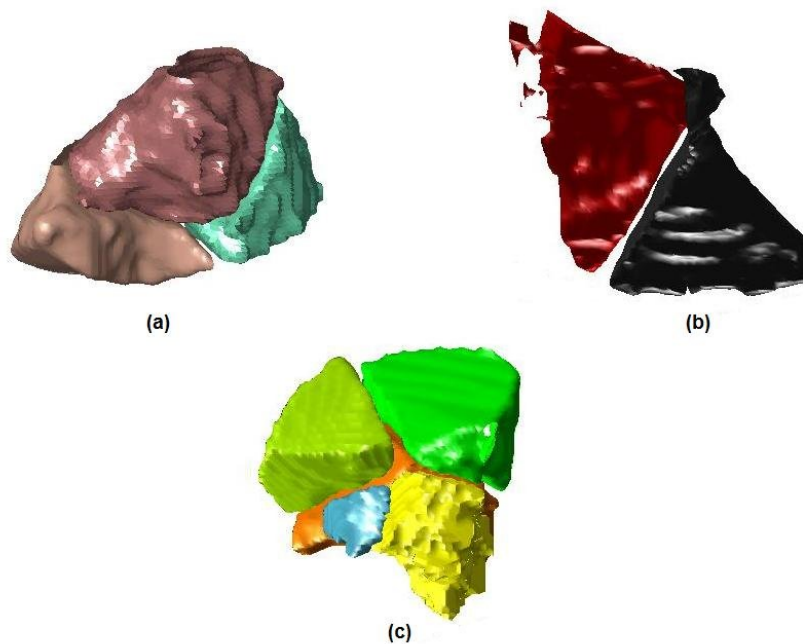
Figure 5-9: The modelled bronchopulmonary segments of the right lung in lobar groupings, (a) RU lobe, (b) RM lobe and (c) RL lobe.

Furthermore, visual comparisons are the only method available for comparisons on shape and morphology of relative segments between different datasets. Figure 5-9 displays the segments of the right lung in lobar groups in an effort to establish the form and shape of each segment. It can easily be observed that the predicted shapes are very much conical in shape in the positions where the segmental airways penetrate into the segments and their contours get more spherical in the more distal regions of the lung. Furthermore, the predicted segments are shown to be robust and continuous, with the exception of the red and black segments in the RM lobe. The discontinuities displayed in the red segment are an effect of the digital nature of the dataset while the long bottle-neck apparent in the black segment is present due to the low-accuracy initial-condition data. Even with these two relative deformations, the shapes achieved by the Segmental Model are shown to be very close approximations to the outlines of natural bronchopulmonary segments, both in their shapes and in their relative topologies.

Even though the qualities of the Segmental Model spaces can only be visually investigated, it is possible for these sub-spaces to be quantified as percentages of total lung volume and for comparisons with previous models and generalistic atlases to be made. Table 5.2 displays the relative sizes of the segments for the Segmental Model, 3 different applications of the model suggested by Sauret (PhD thesis, 2000), implemented on the airway data of 3 CT scans, one on the first 6 generations of a healthy human volunteer and two on the first 6 and 9 generations of two lung casts, and, finally, the data used in an atlas utilised in the Southampton General Hospital (SGH) (Fleming et al. (2004b). In Models A, B and C, as well as in the atlas, it was impossible to uniquely identify some segments. For that reason, the combined volume of all the unidentified segments that belonged to the same lobe was used to extract the relevant percentages (for example, RL lobe, segments S7-S10). The relevant histogram can be observed in Figure 5-10. In segmental groups where unique segment percentages are missing, the volume is equally divided between the segments that occupy the space.

Lobe	Si	Segmental Model	Sauret Model A	Sauret Model B	Sauret Model C	SGH atlas
RU	S1 (brown)	8.9	5.2	5.8	6.8	0.5
	S2 (cyan)	6.9	3.9	6.3	6.3	3.8
	S3 (pink)	6.8	8.8	7.2	6.3	5.8
RM	S4 (red)	5.0	2.2	3.2	6.5	1.2
	S5 (black)	4.8	5.0	7.5	4.2	4.1
RL	S6 (green)	6.4	11.6	9.0	6.0	5.7
	S7 (yellow)	2.9			1.5	4.4
	S8 (orange)	8.7			2.2	11.7
	S9 (alcohol)	1.0	15.1	13.2	12.6	2.0
	S10 (cabbage)	5.0				11.4
LU	S1 (brown)	3.1	2.2	4.9	3.2	1.5
	S2 (cyan)	3.6	4.2	2.0	4.1	1.0
	S3 (pink)	7.5	8	5.4	6.6	5.1
	S4 (red)	8.0	9.8	11.3	7.4	4.4
	S5 (black)	6.2	2.5	0.9	3.1	4.1
LL	S6 (green)	2.7	5.0	7.2	7.9	6.8
	S7 (yellow)	3.0	11.5	6.6	8.8	11.6
	S8 (orange)	2.5				
	S9 (alcohol)	2.4	2.9	5.9	4.8	3.6
	S10 (cabbage)	3.5	2.1	3.3	1.5	10.7

Table 5.2: Relative size of the segments in % of total lung volume. Model A was based on the first 6 generations of the CT data on a human volunteer, Model B on the first 6 generations of a lung cast and Model C on the first 9 generations of a lung cast.
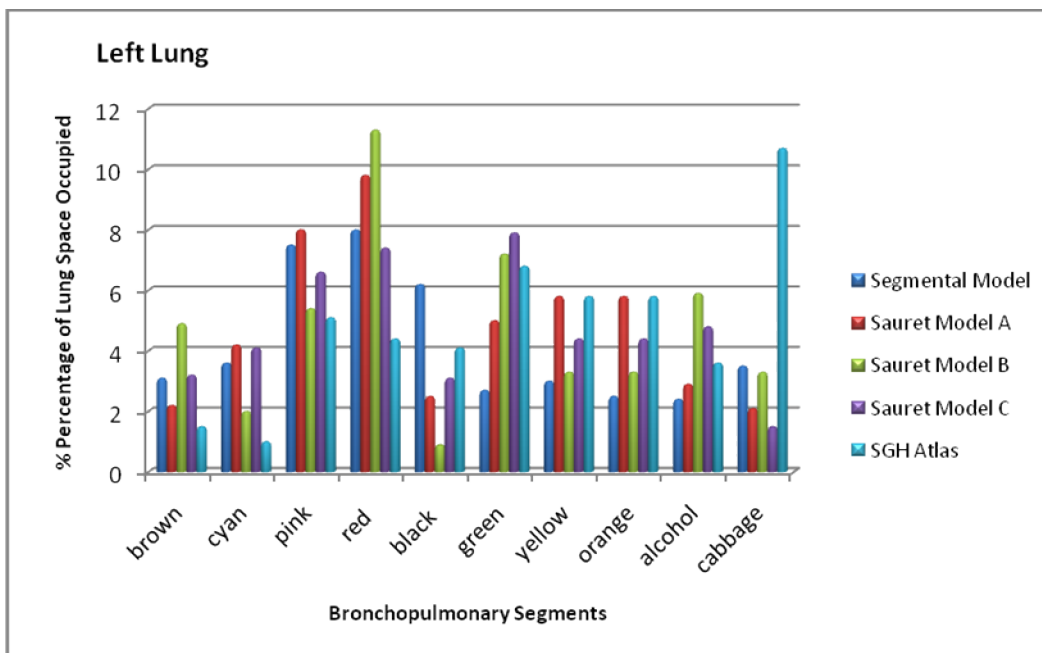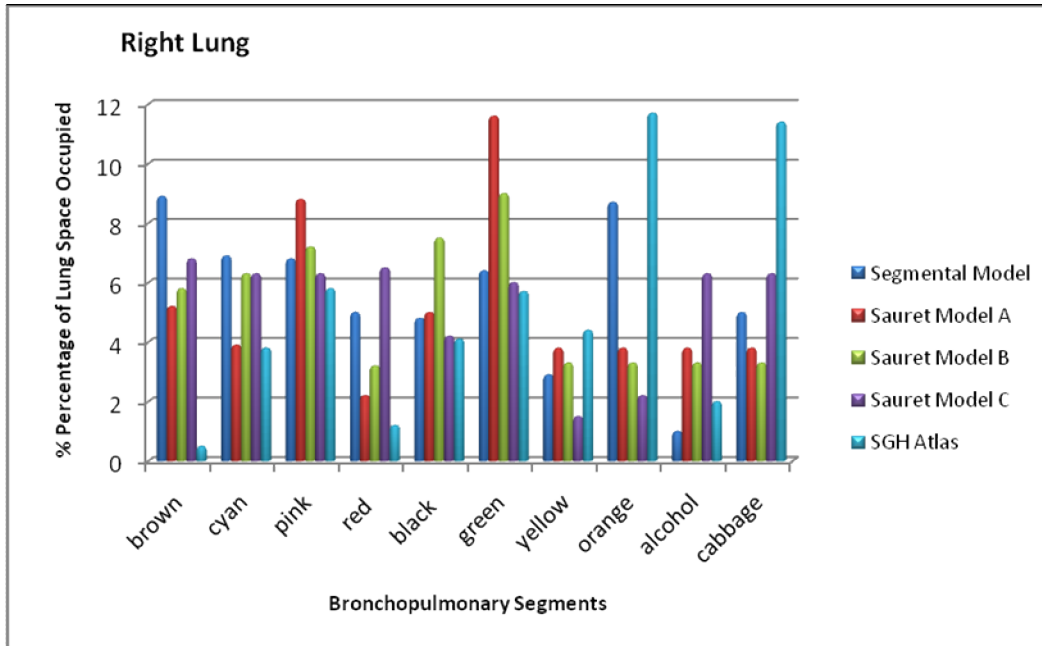
Figure 5-10: Histogram representations of the data available in Table 5.2. Percentages are taken with respect to the total lung space. The two lungs are treated separately.

It is obvious from the Table 5.2 and its histographic representation in Figure 5-10 that, even though some disagreement between the predictions made by different models doesn't cease to exist, the values calculated by the Segmental Model are well within the expected ranges. Furthermore, closer examination of all datasets shows that the Segmental Model follows the mean values of volume percentage per segment estimated by the other 4 available models. The existing discrepancies between different models can be attributed mostly to inter-subject variability and, where the atlas and some segmental groupings are concerned, to the generalistic nature of some data.

In conclusion, the Segmental Model presented in this chapter compares well with both the morphology and the morphometry of the human lung. The former is done by visual inspection while the latter is a product of an assessment made based on different available datasets that exist in the literature. The model has some distinct advantages. First of all, it retains a near-optimal shape and topology for the segments, a characteristic very important for any model that uses personalised data. In addition, the predicted segmental volumes lie well within the ranges estimated by previous algorithmic methods and general atlases. Most importantly, all 20 segments of the lung space are exclusively identified without ambiguities using a fair amount of initial condition data. On the other hand, the necessity for so extensive initial conditions is also the model's biggest disadvantage, a weakness that will be addressed in the next section.

5.4   Segmental Atlas

As mentioned above, the Segmental Model has many advantages. However, for the generation of the model the use of at least a CT scan of the lungs of a human subject is required in order to define the confining spaces and the the first 5 generations of the airway tree, which are necessary for the identification of the segmental roots. This renders the Segmental Model a bit unwieldy for clinical purposes since, in many occasions, the use of such multi-

purpose CT scans is either expensive or, simply, unnecessary. For that reason, the creation of a dynamically generated atlas of the initial conditions which are required for the implementation of the Segmental Model was thought to be an essential improvement. The input data necessary for this atlas are some space-constriction areas (possibly an MRI or CT of the lungs), and their relevant hilum positions.

The Segmental Atlas is created with the purpose of providing the extension lines which form the foundation for the space-filling process. The original line-extension vectors were defined with the help of the start- and end-points of the relevant segmental roots. However, these points are relatively close to each other. Therefore, small inclinations in airway directionality would heavily affect the orientation of the whole segment. To remove this possibility, the atlas is concerned with estimating a different set of points, always in a dynamic way and with respect to the confining lung space: The segmental airways' end-points and the centres of mass of the segments.

The choice of the centres of mass as points belonging to the extension line is an approximation made because of the conical shape of the segments. In a cone, the centre of mass is located on the line connecting the middle of the base to the edge. Even though some distortion is inevitably introduced to the creation of the segments this way, this approximation was found to hold in the vast majority of occasions, confirming the validity of the hypothesised choice of the vector-defining points.

The atlas can be considered an adaptation of the hemispherical transform introduced in Chapter 4 and used for the creation of the Hybrid Conceptual Model. The main difference with this transform is that, in addition to the Fractional Distance Ratio (FDR, equation (4.1)), two more angular ratios, one expressing azimuth and one expressing elevation (see Figure 4-5 for definition) need to be employed; namely, the Fractional Azimuth Ratio (FAR) and the Fractional Elevation Ratio (FER). All calculations are made with respect to an origin at the lung hilum and considering counter-clockwise

motion. First, the FDR of each point defining a modelled segment is calculated, using the method displayed in Figure 4-4. Then, the plane x-y is separated out of the restriction-space data (MRI of the lung) and two confining lines are manually drawn. These confining lines, named the primary and the secondary line, must divide the plane into two portions, the portion that includes the lung area under investigation and a region with empty pixels. For optimal results, the lines need to connect tangentially to the lung perimeter.

The calculation of the angles θ_T and θ_P (Figure 5-11), defined as the angles formed between the primary and the secondary line and between the primary line and the shadow of the segmental point under investigation on the azimuth plane respectively, is the next step of the process. Using these two angles,

$$FAR = \frac{\theta_P}{\theta_T} \quad (5.6)$$

may now be estimated. A similar process is then repeated on the elevation plane x-z for the

$$FER = \frac{\varphi_P}{\varphi_T} \quad (5.7),$$

where φ_P is the angle between the relevant primary line and the shadow of the point under investigation on the elevation plane and φ_T is the angle between primary and secondary line. An important point to be made here is that for the FER only the shadow of a point on the x-z plane is used and not the real elevation plane, defined as the angle of the point with respect to the x-z plane. This is done in order to simplify the process, since only one planar image of the lungs becomes necessary instead of 40 different planar images (two for each defining point of each segment).

created with
nitro PDF professional
download the free trial online at nitropdf.com/professional
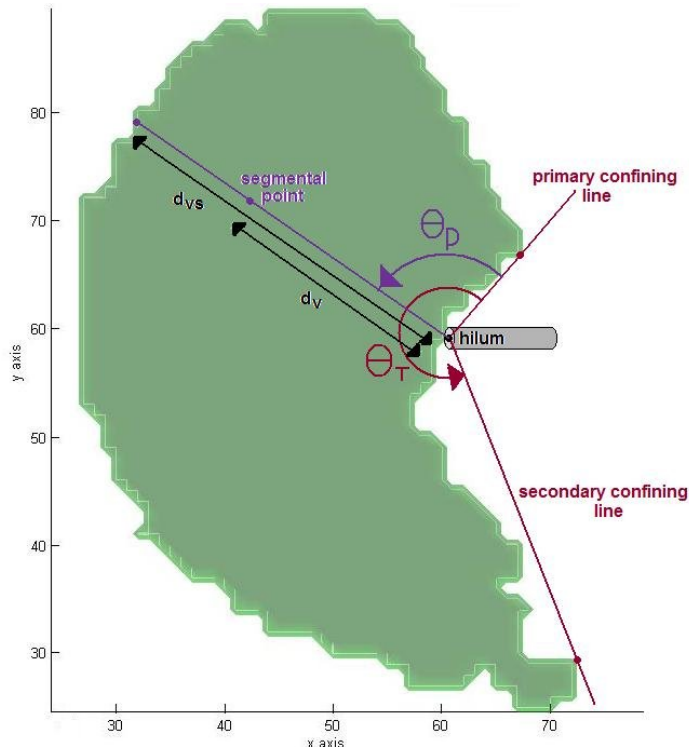
Figure 5-11: A 2D representation of the Segmental Atlas creation process.

The procedure described above is repeated for all 40 segment-defining points and a set of 3 ratios is extracted and stored for each point. A 2D version of the process is displayed in Figure 5-11 and the ratios calculated for the segmental roots and the centres of mass for each segment are displayed in Table 5.3. The use of the 2 angular and the one distance ratio makes possible the generation of a Segmental Model based only on information about the restrictions imposed from the limited volume of the lung space and the position of the hilum in that space. This is true because all 40 necessary points can now be calculated in any probable lung space simply by defining a set of confining lines in order to obtain θ_T and φ_T and then solving equations (5.6), (5.7) and (4.1) for θ_P, φ_P and d_{vs}. Additionally, the Segmental Atlas takes into account the total shape of the lung, which is a very important feature when trying to model the segmental sub-spaces. Even though this happens only 2-dimensionally, which is a limitation of this method, it retains most information of total lung shape pertinent to the creation of the modelled sub-spaces. Furthermore, the simplicity of the process and the

135

personalised nature of the data extracted constitute the Segmental Atlas a very useful alternative to the use of generalistic anatomical atlases when no available CT data of the human airway tree exist. Combined with the Segmental Model, the Atlas can be a very effective tool for applications demanding the utilisation of models of the lung segments.

Right Lung	Centre of Mass			Segment Roots		
	FDR	FAR	FER	FDR	FAR	FER
S1 (brown)	0.659	0.614	0.18	0.333	0.558	0.287
S2 (cyan)	0.614	0.36	0.338	0.284	0.452	0.287
S3 (pink)	0.634	0.755	0.439	0.239	0.631	0.421
S4 (red)	0.801	0.858	0.813	0.425	0.786	0.799
S5 (black)	0.755	0.72	0.755	0.395	0.724	0.79
S6 (green)	0.6	0.346	0.692	0.206	0.424	0.78
S7 (yellow)	0.644	0.452	0.908	0.5	0.525	0.84
S8 (orange)	0.667	0.325	0.777	0.395	0.476	0.804
S9 (alcohol)	0.852	0.664	0.789	0.5	0.687	0.783
S10 (cabbage)	0.721	0.601	0.635	0.401	0.636	0.763
Left Lung						
S1 (brown)	0.656	0.688	0.852	0.364	0.626	0.812
S2 (cyan)	0.705	0.62	0.668	0.387	0.6	0.735
S3 (pink)	0.674	0.188	0.356	0.312	0.374	0.763
S4 (red)	0.682	0.223	0.26	0.358	0.323	0.344
S5 (black)	0.667	0.275	0.553	0.269	0.34	0.479
S6 (green)	0.541	0.794	0.322	0.283	0.775	0.217
S7 (yellow)	0.745	0.161	0.072	0.444	0.508	0.162
S8 (orange)	0.721	0.441	0.222	0.563	0.468	0.227
S9 (alcohol)	0.761	0.594	0.33	0.439	0.626	0.228
S10 (cabbage)	0.663	0.768	0.105	0.377	0.683	0.158

Table 5.3: The Fractional Distance, Fractional Azimuth and Fractional Elevation Ratios.

Shells	Right Lung No. of voxels			Left Lung No. of voxels		
	Total Lung	Segmented Lung	% diff.	Total Lung	Segmented Lung	% diff.
1	83	85	-	105	92	-
2	566	580	0.02	688	710	0.02
3	1323	1291	0.04	1769	1771	0.02
4	2936	2787	0.18	3772	3509	0.24
5	4918	4985	0.1	6813	6667	0.13
6	6245	6074	0.17	8794	8450	0.31
7	9925	9539	0.4	13595	13130	0.42
8	13174	13230	0.15	18209	17829	0.34
9	17366	16834	0.6	23312	22897	0.37
10	26401	27516	1.4	33541	35561	1.83

Table 5.4: The volume of each shell calculated for the whole lung and for the segmented version of the lung. The volume percentage of each shell with respect to the lung volume is calculated and the differences between these percentages are also displayed.

5.5 The Segmental Hybrid Conceptual Model

With the creation of the Segmental Model it becomes possible to proceed to the construction of a fairly accurate deterministic description of the human airway tree. However, before proceeding to the next chapter, some reference as to how the Hybrid Conceptual Model (HCM), presented in the 4th Chapter, may be affected by the development of the Segmental Model, has to be made.

The process outlined for the generation of the HCM is now implemented on the lung sub-spaces defined by the Segmental Model and not on the MRI scan of the whole lung. This is feasible when two key modifications are applied. The first concerns the hilum positions, which are now replaced by the segmental hila, defined as the position where the segmental root airways penetrate into the segmental space. The second involves the adaptation of the V_{ij} quantity (volume of each generation in each shell, equation (4.2)) to fit the new spatial conditions. The resulting new model is referred to as the Segmental Hybrid Conceptual Model (SHCM).

created with
nitro^{PDF} professional
download the free trial online at nitropdf.com/professional
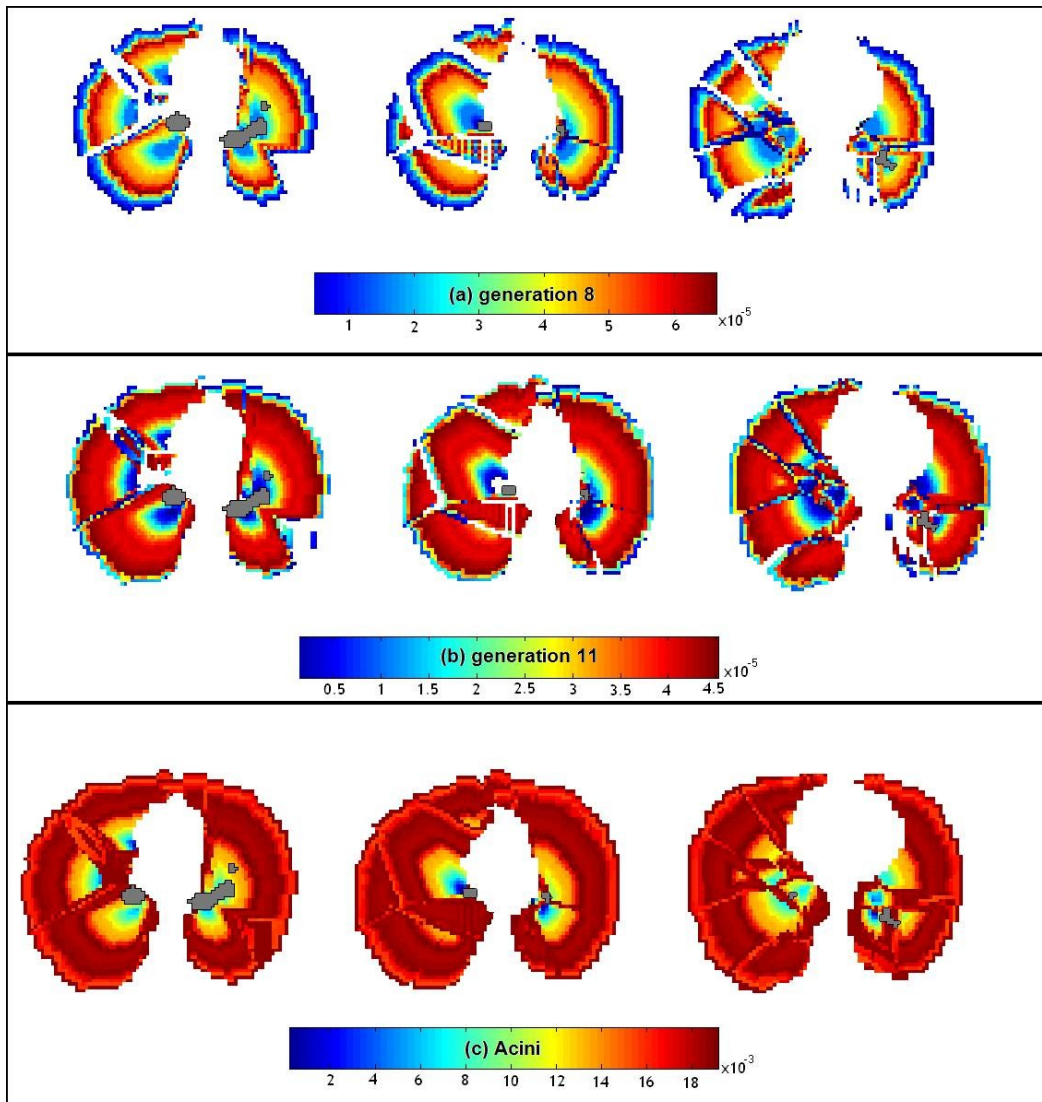
Figure 5-12: The Segmental Hybrid Conceptual Model implemented on (a) generation 8, (b) generation 11 and (c) the Acini. The interpolation process uses as edges the surfaces of the segments. Only the transverse slices 75, 80 and 65 are displayed, in a set of 128 transverse slices. The airways in generations 1-5 are shown in gray.

An important assumption needs to be made first. For simplicity's sake, the volume of a specific airway generation is considered to be divided between the segments proportionally to the relative volume of the segments with respect to the total lung volume. This is a very significant assumption as it renders possible the combination of the data already available in Table 4.3 and Table 5.2 in order to calculate the relevant V_{ij} per segment. Using Table 5.2 and the fact that, in the particular dataset used in this study the Right

created with nitro^PDF professional
download the free trial online at nitropdf.com/professional

Lung occupies 57% of the total lung space, with the rest being occupied by the Left Lung, a proportionality factor is calculated:

$$R_s = \frac{Vsegment_k}{Vlung} \quad (5.8),$$

where Vsegment$_k$ is the volume of segment Sk, $k = \mathbb{Z} \in \{1, 2 \ldots 10\}$, and Vlung is the volume of the lung the particular segment Sk is a constituent part of. Rs is then used to factor the V_{ij} data of Table 4.3. Finally, for each segment, the interpolation process discussed in Section 4.3.4 is utilised and each voxel of each segment obtains the 15 discrete V_{ij} values that characterise the HCM. An important note is that, during this process, the airways available through CT scans of the airway tree need to remain unaltered.

The results of this procedure performed for generations 8, 11 and the Acini can be observed in Figure 5-12. It can be seen that the conceptualised airway data are now even more naturally distributed in comparison to the display of Figure 4-12. More importantly, this redistribution doesn't affect the general volumetric balance of the different generations, as explored in the previous Chapter. This is central to the validity of the new model since a new definition of the hilum is used in the SHCM, thus modifying the meaning of the cells as presented in the previous chapter. Even with the use of the segmented instead of the whole lung space, the number of voxels-per-segment remains unchanged (Table 5.4), with only very small differences introduced mainly due to the digital nature of the data. This fact signifies that, even though the shells are arranged in different positions within the lung space, the volumes-per-shell calculated in Chapter 4 still retain their relative volumes-per-voxel, which in turn means that overestimation of the volume of an airway generation for a specific shell in one segment is accompanied by an underestimation of the volume of that specific generation in a different segment. An example of this would be that if shell 5 contains 1000 voxels, i.e. 50 voxels per segment, if in one segment there are only 30 voxels of shell 5 this means that the volume of all airway generations contained within shell 5 in the specific segment would be lower than the mean value. However, since the missing 20 voxels are divided along the rest of the segments, the overall volume for the airway generations that belong to shell 5 remains the same throughout the lung. For that reason, the SHCM can

be thought of as a more efficient way of distributing the shell configuration within the lung space, without adversely affecting the validity of the HCM and still maintaining its usefulness.

5.6   Conclusion

In this chapter the need for the segmentation of the human lung into realistic sub-spaces was addressed. The lung morphology was investigated and the suitability of the bronchopulmonary segments was established. Then a method of modelling these segments was suggested and discussed. The method, called the Segmental Model, was shown to produce good results both morphometrically and topologically. In addition to that, a technique for simulating the bronchopulmonary segment division in any confining space with very little initial information was investigated. Finally, a modification of the Hybrid Conceptual Model based on the findings of this chapter was introduced.

It can easily be seen that the literature is very lacking in efforts to accurately model the segmental space of the lungs. Hence, it is felt by the author that the model presented in this chapter and its products, such as the Segmental Atlas and the SHCM can be very important not only for clinical applications but, also, for any application that involves the division of large areas into smaller, more manageable sub-spaces. These sub-spaces, modelled by the Segmental Model, will be central in the effort to model the human bronchial tree, which is the theme of the next chapter.

created with
nitro^PDF professional
download the free trial online at nitropdf.com/professional

Chapter 6

A Deterministic Model of the human airway tree

6.1   Introduction

In the previous chapters the morphology, topology and biological necessities transcending the functionality of the lung were discussed and several models of the lung sub-structures were created. These models, though important, are peripheral to the purposes of this study and culminate into the creation of a fully deterministic model of the human tracheobronchial tree, which is presented in this chapter. In the subsequent sections, first the proper equations and statistical datasets characterising the relationships between the model's constituent parts will be identified and explored. Following that, the deterministic model itself will be broken down and presented in consecutive steps. Finally, the model's results will be presented and discussed and comparisons with previous modelling efforts and other related morphometric data will be performed.

6.2   Equation And Statistical Dataset Selection For The Development of the Model

The creation of an airway tree model, if made in a deterministic fashion, needs to include 4 different types of relationships, each one used for the estimation of the 4 morphometric features characterising the modelled airways: the length (l), the diameter (d), the branching angle (θ) and the planar rotation angle (φ). Definitions for each of these characteristics (especially the angular data) exist in Section 2.5.4. In this section, an investigation of the optimal relationships that serve the purposes of this study is made. The correlations to be examined are the length-to-diameter ratio, the parent-to-daughter diameter ratio, the branching angle-to-diameter ratio

and, finally, the planar rotation angle statistical evaluation with respect to airway generation number. Furthermore, a selection of relevant statistical datasets available in the literature will be made; these may be used for both the normalisation and the validation of the modelling results.

6.2.1 Length-to-Diameter Ratio

One of the most common morphometric relationships in the line of research concerning the human lung is the ratio between the length and the diameter of the airways. This is because it connects the two most commonly measured elements of the tracheobronchial tree morphometry. The rule of thumb for this ratio, established after the examination of many datasets that were available in the literature [Weibel (1963), Soong et al. (1979), Yeh and Schum (1980), ICRP (1994)], is that

$$\frac{l}{d} = 3 \quad (6.1),$$

with a Standard Deviation (STD) of 1 over a normal distribution. Similar values were also calculated by Sauret et al. (2002) and Tawhai et al. (2000) while Kitaoka et al. (1999) used the mean value of 3 for the generation of their deterministic model.

From the above it becomes obvious that $\frac{l}{d} = 3 + 1$ is a universally accepted relationship and, hence, it will be used for the creation of the deterministic model described in this chapter.

6.2.2 Parent-to-Daughter Diameter ratio

An easy method to calculate the diameter of a daughter airway based on the knowledge of the parent diameter is through the parent-to-daughter diameter ratio. As is shown in Section 2.5.4 (equations (2.1) and (2.2)) and Section 3.4.3 (equation (3.17)), the optimal value for this ratio in the case of a fully symmetric binary branching system is given by

$$\frac{d_{j+1}}{d_j} = 0.794 \quad (6.2),$$

where j is an integer number denoting the generation the airways belong to. In the case of asymmetry, the parent-to-daughter diameter ratio was calculated to be

$$\frac{d_{j+1}}{d_j} = 0.79 \pm 0.15 \ (6.3)$$

by both Tawhai et al. (2004) and Sauret et al (2002). Tawhai also investigated a relationship of minor and major daughter-to-parent diameter ratio, given by the following equations:

$$\begin{cases} \frac{d_{j+1\ major}}{d_j} = 0.88 \pm 0.14\ (a) \\ \frac{d_{j+1\ minor}}{d_j} = 0.69 \pm 0.06\ (b) \end{cases} \ (6.4).$$

Kitaoka et al. (1999) suggested the equations based on the Flow Dividing Ratio (FDR) (equations (3.21) and (3.22)). However, an examination of these equations on real data showed that the results of this equation are heavily dependent on the FDR and, when used backwards in order to calculate the FDR from already existing diameter values as estimated by equations (6.2, (6.3) and (6.4), did not provide valid results for the angular data (equation (3.24)). Furthermore, the use of equation (3.22), which is similar to (2.4), connecting the parent and daughter diameters with the help of the diameter exponent **n**, can be shown to produce a tree structure of relatively high asymmetry.

For these reasons, a combination of the two methods suggested by Tawhai and Kitaoka will be implemented. Equation (6.2) will be utilised in parts of the modelling algorithm where symmetry is required while in the case where asymmetry is necessary, equation (6.4 a) will be used for the calculation of the major daughter diameter and equation (3.22) will take the form

$$d_{j+1\ minor}^n = d_j^n - d_{j+1\ major}^n \ (6.5)$$

in order to estimate the minor daughter diameter, where j again represents the generation the airways are in and n is the diameter exponent which relates to the type of flow observed in the specific area of the lung according to the depth of generation j. Because the diameter exponent is dependent on

the airway generation number (for more information see Section 3.4.3), the linear equation (6.6) expressing this characteristic is used for its calculation instead of a mean value:

$$\begin{cases} n = 2.745, \ j < 5 \\ n = 0.0245 * j + 2.2625, \ 5 \leq gen \leq 15 \\ n = 2.9, \ gen > 15 \end{cases} \quad (6.6).$$

6.2.3 Branching Angle

The optimal branching angle for minimal volume and resistance in a symmetric binary branching system can be calculated to be $\theta_{opt}=37.28^o$ with the help of equations (3.10) and (6.2). A definition of the branching angle θ is given in Section 2.5.4 and can be seen in the image of Figure 2-6. Equation (3.10) represents a relationship connecting the branching angle to the diameters of the parent and the associated daughters.

The above optimal branching angle has been confirmed to be a valid result through many different morphometric studies. For example, Tawhai et al. (2004) estimated the branching angle (a) for the first 9 generations of a HRCT dataset and (b) for a full descriptive model to be respectively

$$\begin{cases} \theta = 36^o \pm 20.85^o \ (a) \\ \theta = 50.3^o \pm 28.3^o \ (b) \end{cases} \quad (6.7).$$

Equations (6.7) display a trend of the branching angle to increase according to the distance of the airways from the trachea. This has been shown to be true in the human airway tree and can be explained via the need for lower gas velocities, i.e. higher resistance to air flow, in parts of the lung where diffusion and not gas transfer is the major function. For that reason, Tawhai also investigated the branching angles of different diameter ranges, the results of which can be seen in Table 6.1. In addition, as mentioned in the previous section, the equation (3.24) used by Kitaoka et al. (1999) to provide the branching angle with reference to the FDR, could not seem to give valid results. Finally, equation (3.10), when applied to an asymmetric system, can

be shown to give relatively high asymmetry which is uncharacteristic of the human bronchial tree.

For these reasons, a combination of the results described by Tawhai et al. (2004) and shown in Table 6.1, the equation (3.1) and some of the statistical data per generation described in Section 6.2.5 will be used for the calculation of this particular feature of the model. However, the results of these calculations will only form a preliminary step for the development of a dynamic process used for the selection of values for the branching angle with respect to the local shape of the confining lung space. This process will be described and discussed in Section 6.3.2.

6.2.4 Planar Rotation Angle

The planar rotation angle φ is defined as the angle between two consecutive bifurcation planes and expresses the 3D orientation of the daughter branches with respect to the parent plane. Even though such an angle is very important for the generation of realistic airway tree models, not much data are available in the literature concerning its correlation to the other morphometric features. Martonen et al. (1995), which introduced the planar rotation angle as an integral morphometric characteristic of branching structures, assumed a steady value of $\varphi=90^o$. This hypothesis was confirmed by both Sauret et al. (2002), who found it to be $\varphi=76^o\pm41^o$ for the first 9 generations of a lung cast, and by Tawhai et al. (2004), who calculated it to be $\varphi=76^o\pm45.3^o$ for the first 9 generations of a HRCT scan and $\varphi=90^o\pm43^o$ for a full model of the airway tree.
A huge variation on the values taken by the planar rotation angle is apparent in these studies. For that reason an algorithm for the dynamic selection of the rotation angle with respect to the local lung shape was created. This algorithm is fully explained in Section 6.3.2.

6.2.5 Statistical Datasets

Even though several statistical datasets of the values of the morphometric characteristics of the lung are available in the literature, only two will be extensively used in this study, the sets provided by ICRP (1994) and Soong et al. (1979). The former is selected because the model proposed is constructed as a mean value of many previously suggested models and, therefore, it can be considered to be an aggregate model of the human lung. Soong's dataset has the advantage that it provides additional information on the standard deviations of the morphometric data presented, which makes comparisons on data ranges easier. Finally, both datasets, which are shown in Table 6.2, display mean morphometric values per generation up to at least generation 19 and these values have been normalised to a lung volume of 3.3l before their presentation.

$d_j \geq 4mm$	$\theta = 33.71^o$
$4mm > d_j \geq 3mm$	$\theta = 36.72^o$
$3mm > d_j \geq 2mm$	$\theta = 45.19^o$
$2mm > d_j \geq 1mm$	$\theta = 53.34^o$
$1mm > d_j$	?
l/d minor	2.88±94
l/d major	2.96±0.9
d_{minor}/d_{major}	0.81±0.17
d_{minor}/d_{parent}	0.69±0.6
d_{major}/d_{parent}	0.88±0.14
l_{minor}/l_{major}	0.68±0.2

Table 6.1: Morphometric data relationships investigated by Tawhai et al. (2004). Besides the mean branching angle value for different diameter ranges, the length-to-diameter ratio of both the major and the minor daughter, the relationship between diameters of the entire family of airways and the length ratio between major and minor daughter are also presented.

generation	ICRP (1994)			Soong et al. (1979)			
	d_{mean}	l_{mean}	θ_{mean}	d_{mean}	d_{std}	l_{mean}	l_{std}
6	2.9	6.6	34	2.45	0.67	7.87	3.93
7	2.4	6	48	2.1	0.68	6.65	3.8
8	2	5.3	53	1.63	0.57	5.6	3.64
9	1.65	4.4	54	1.35	0.57	4.72	3.3
10	1.35	3.62	51	1.14	0.57	4.02	3
11	1.1	3	46	0.95	0.54	3.41	2.78
12	0.88	2.5	47	0.83	0.55	2.89	2.34
13	0.72	2.1	48	0.72	0.47	2.36	1.83
14	0.6	1.7	52	0.65	0.39	2.01	1.45
15	0.53	1.4	45	0.58	0.29	1.75	1.14
16	0.51	1.1	45	0.52	0.21	1.44	0.72
17	0.46	0.92	45	0.47	0.14	1.23	0.49
18	0.41	0.76	45	0.44	0.1	1.02	0.31
19	0.38	0.63	45	0.41	0.06	0.87	0.195
20	0.35	0.52	45	0.39	0.05	0.73	0.13
21	0.33	0.43	45	0.38	0.04	0.61	0.09
22	0.31	0.36	45	0.36	0.03	0.52	0.06
23	0.3	0.3	45	0.36	0.03	0.44	0.04

Table 6.2: Statistical data available in literature. The diameter and length values are in mm while the angles are in degrees. Generations 1-5 are not required in this study.

6.3 Deterministic Model Algorithm Step By Step

Having selected the optimal relationships between the morphometric features that are necessary for the implementation of a mechanistic process that simulates the human lungs, it is now possible to proceed to the description of the main Deterministic Algorithm. The algorithm can be described as a dynamic space- and shape-fitting semi-iterative process and it is an attempt to combine all the advantageous characteristics of previous deterministic morphometric models that exist in the literature.

The implementation of the deterministic model may be subdivided into 4 distinct steps: First, a protocol for the formalisation and automatic selection of the input data needs to be created. Then, a routine for the generation of an airway-tree structure, where no space constraints are being imposed but some optimality conditions need to be satisfied, specifically for the selection of angles, is being created. The next step includes the identification and isolation of the unconstrained tree enveloping space. Finally, the iterative implementation of a shape-fitting (tree expansion-dilation) process is explored and presented. The 4 algorithmic steps forming the deterministic algorithm are shown in the following diagram:

INPUT: Segmental Model (or other constraining space), relevant skeleton airway tree data
↓

Automatic airway-data selection

Unconstrained tree development

→ Envelope space calculation

Tree structure Expansion-Dilation algorithm ←

↓

OUTPUT: A table with the nodal coordinates of each arway, its unique morphometry and ID binary number
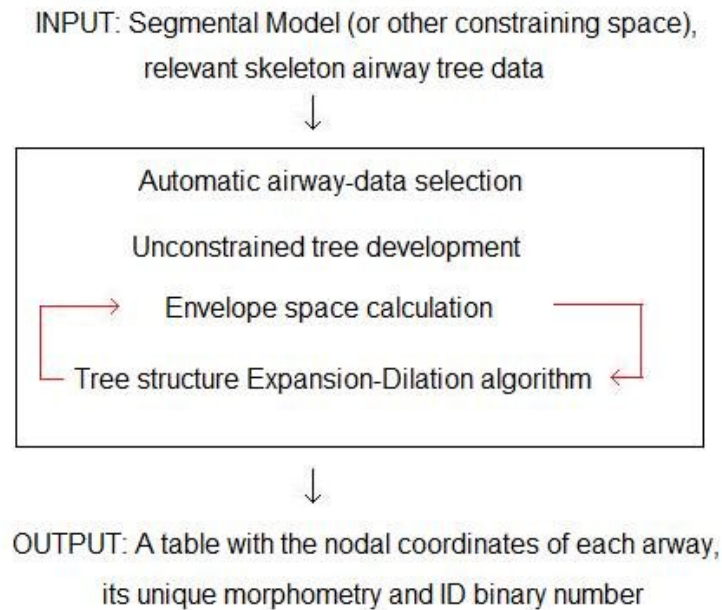
6.3.1 Input Data Formalisation And Data Automatic Selection

There are two types of input data necessary for the creation of the airway tree; the skeleton data of the available airways and their relevant constraining spaces. Since the Deterministic Model described in this study is implemented on a segmental level, the latter input must be the Segmental Model, the creation of which is discussed in the previous chapter and out of which a single segment needs to be isolated. The isolated segment must be given in a binary matrix of the same dimensions as the Segmental Model matrix.

148

The skeleton data are formalised in a table, called the full-generation table, with the following format:

ID number	x_{start}	y_{start}	z_{start}	x_{end}	y_{end}	z_{end}	Diameter, (mm)

Certain rules need to be followed during the creation of the full-generation table. First of all, each row needs to contain only data of a single airway. Furthermore, the airways that belong to similar generations need to be grouped together in consecutive rows, and the groups also need to be ordered successively, starting from the first available generation, which in our dataset is generation 0 (trachea) and ending at the last detected airway (generation 5). Moreover, daughter airways of the same parent need to occupy consecutive rows in the table. Finally, the parent and daughter row positions in the full-generation table must be connected via the formula

$$daughter\ row = \begin{cases} 2*parent\ row \\ 2*parent\ row + 1 \end{cases} \quad (6.8).$$

This relationship is valid only when all the elements of a single generation are accessible. If this is not the case, some vacuum rows, which need to be removed, might exist.

In addition to the above, a table of the same column format but having as rows only the segmental root data is created, namely the root table. Each segmental root dataset must be contained in the row whose integer number is associated with the respective segment in the Segmental Model. The unique ID number of the root of the segment is then used to automatically identify all the elements of the full-generation table that form a segmental sub-tree and all these elements are stored in a separate table, called the generation table, which follows the same format as the full-generation table. This generation table, along with the segmental constraining space, form the main inputs for the development of the unconstrained tree process.

149

6.3.2 Unconstrained Tree Creation

Methods

The first strictly algorithmic part of the Deterministic Algorithm consists of the development of an unconstrained tree. A method closely resembling the one described by Martonen et al. (1995) is followed here in the sense that no direct spatial constraints are imposed on the growth of the tree and the tree grows only as far as generation 15. However, there are a few major differences; most notably, the use of morphometric relationships and dynamic methods for the selection of airway characteristics based on the, already estimated, parent morphometry and the local shape of the lung. The latter is expressed with the use of the segmental subspaces in order to induce some measure of indirect control over the space occupied by the tree.

In more detail, the unconstrained tree algorithm is constructed as follows: First, the generation table, the creation of which is discussed in the previous section, is examined in order to identify the first possible parent airway that forms the root of the sub-tree under development. Two empty rows are then added in the end of the generation table and are associated to the parent airway. These new rows will host the coordinate data of the two daughter airways that are the result of the morphometric calculations taking place in the rest of the process. The association is made through the use of the ID numbers, which are stored in the first column of the table and are the first elements of the two offspring to be investigated. Since the ID numbers are binary in form, the daughter Ids are generated by adding a 0 or a 1 at the end of the associated parent's ID number. Markedly, the binary nature of this number also reveals the airway-tree generation each branch belongs to through the relationship

$$airway\ generation = ID\_number\_length - 1 \quad (6.9),$$

where ID_number_length is the number of elements forming the ID number. The next step in the algorithm is the creation of a routine handling the translation from airway morphometric values to real coordinate positions of

each branch in 3D. This can be done directly through the use of rotation matrices; however, this approach demands prior knowledge of the angular orientation in the final position of the daughter, which can be difficult to predict. For that reason, a simpler method involving the simultaneous calculation of the coordinates of both daughters is preferred. The important components of the translation process are displayed in Figure 6-1.
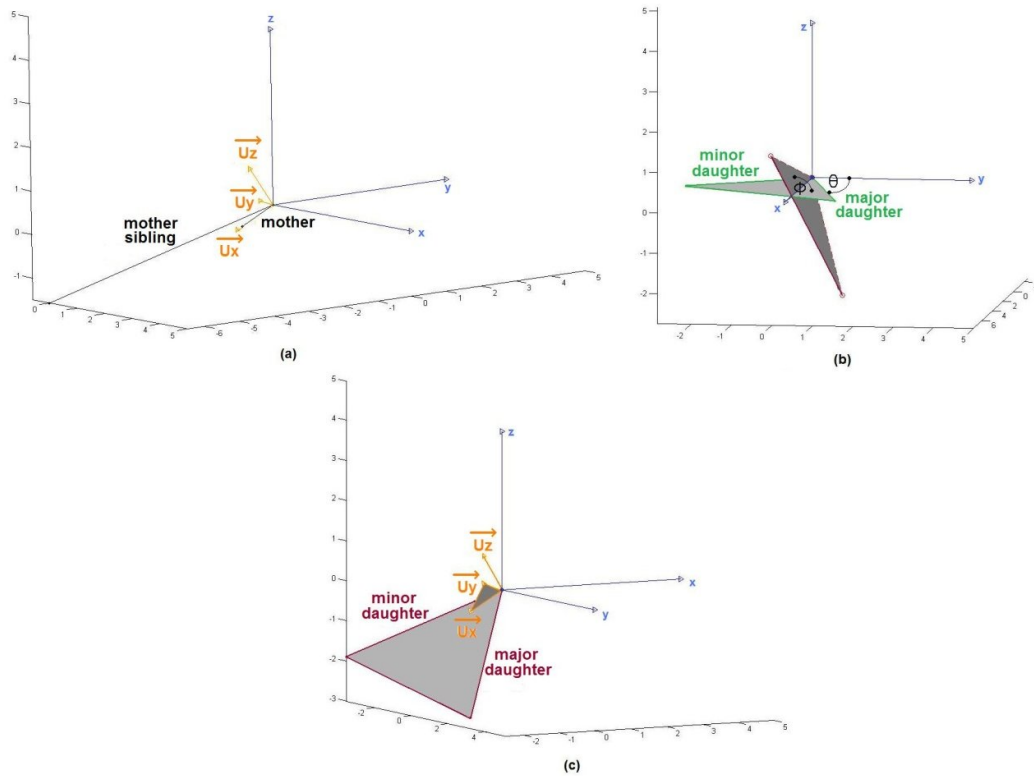

Figure 6-1: The morphometry-to-coordinates translation process. (a) The parent and its sibling (black) define a new axial (rotated) coordinate system (yellow). (b) The rotation of the daughter plane (daughters in green) by φ around the original x axis. (c) The final positioning of the daughter airways (deep red) with respect to the target coordinate system and the relevant planes.

The primary task here is to define the parent plane. This is done by transforming the parent airway into a vector,

$$\overrightarrow{parentA} = [end\ coordinates] - [start\ coordinates]\ (6.10),$$

and transferring its starting point at the origin of a normal Cartesian coordinate system in order to form the x axis of a rotated system. Then the parent airway's sibling needs to be located in the generation table and a second vector $\overrightarrow{parentB}$ is determined. Using these two vectors, the axes of a new, rotated orthogonal system are computed using vector calculus:

$$\begin{cases} \overrightarrow{Ux} = \dfrac{\overrightarrow{parentA}}{|\overrightarrow{parentA}|} & (a) \\ \overrightarrow{Uz} = \dfrac{\overrightarrow{parentA} \times \overrightarrow{parentB}}{|\overrightarrow{parentA} \times \overrightarrow{parentB}|} & (b) \\ \overrightarrow{Uy} = \overrightarrow{Uz} \times \overrightarrow{Uz} & (c) \end{cases} \quad (6.11),$$

where $\overrightarrow{Uz}$ is the normal of the parent plane and the vectors $\overrightarrow{Ux}$ and $\overrightarrow{Uy}$ are two orthogonal vectors on the plane itself. This new system, named the *rotated coordinate system*, defines the final daughter-pair positioning and orientation. The azimuths and elevations of the 3 orthogonal vectors are then calculated and stored.

Having identified the rotated coordinate system, a normal reconfiguration between polar and Cartesian coordinates is carried out for the pair of daughters. The coordinates of the daughter vectors are, at first, calculated without any rotations, i.e. on unrotated the x-y plane, using the relationship

$$\overrightarrow{daughter} = \begin{bmatrix} l * cos\theta \\ l * sin\theta \\ 0 \end{bmatrix}\ (6.12),$$

with l denoting the daughter length and θ being the branching angle. An initial rotation around the x axis of the normal Cartesian system is then performed on the $\overrightarrow{daughter}$ vector using the rotation matrix Rx and the planar rotation angle φ:

$$\overrightarrow{daughter_{new}} = \begin{bmatrix} 1 & 0 & 0 \\ 0 & cos\varphi & -sin\varphi \\ 0 & sin\varphi & cos\varphi \end{bmatrix} * \overrightarrow{daughter} = \begin{bmatrix} x_{new} \\ y_{new} \\ z_{new} \end{bmatrix} \quad (6.13).$$

The new daughter vector is then re-rotated to fit the rotated coordinate system. In order to do that, the $\overrightarrow{daughter_{new}}$ vector is broken up in 3 elementary vectors, each vector associated with one of the orthogonal axes of the target system. What follows is a simple rotation of these individual vectors, using the relevant azimuths and elevations calculated for the target system:

$$\begin{cases} \begin{bmatrix} x_1 \\ y_1 \\ z_1 \end{bmatrix} = \begin{bmatrix} x_{new} * \cos(elevation_x) * \cos(azimuth_x) \\ x_{new} * \cos(elevation_x) * \sin(azimuth_x) \\ x_{new} * \sin(elevation_x) \end{bmatrix} & (a) \\[2em] \begin{bmatrix} x_2 \\ y_2 \\ z_2 \end{bmatrix} = \begin{bmatrix} y_{new} * \cos(elevation_y) * \cos(azimuth_y) \\ y_{new} * \cos(elevation_y) * \sin(azimuth_y) \\ y_{new} * \sin(elevation_y) \end{bmatrix} & (b) \\[2em] \begin{bmatrix} x_3 \\ y_3 \\ z_3 \end{bmatrix} = \begin{bmatrix} z_{new} * \cos(elevation_z) * \cos(azimuth_z) \\ z_{new} * \cos(elevation_z) * \sin(azimuth_z) \\ z_{new} * \sin(elevation_z) \end{bmatrix} & (c) \end{cases} \quad (6.14).$$

It is now possible to calculate the final daughter vector by combining the rotated elementary vectors,

$$\overrightarrow{daughter_{final}} = \begin{bmatrix} x_1 + x_2 + x_3 \\ y_1 + y_2 + y_3 \\ z_1 + z_2 + z_3 \end{bmatrix} \quad (6.15),$$

and then displacing it to fit the original coordinate system of the parent:

$$daughter\ end\ coordinates = parent\ end\ coordinates + \overrightarrow{daughter_{final}} \quad (6.16).$$

With the morphometry-to-coordinate translation routine finalised, it is possible to proceed to the next component of the algorithm, which requires the creation of a provisional symmetric daughter pair. First the diameter is calculated using equations (6.2) and the length and branching angle follow with the help of equations (6.1) and (3.10) respectively. However, there is no relationship available for the calculation of the planar rotation angle; hence, in order to avoid utilising a Gaussian random value generator, a dynamic

method for the estimation of the planar rotation angle that is based on the optimisation of some important criteria was developed.
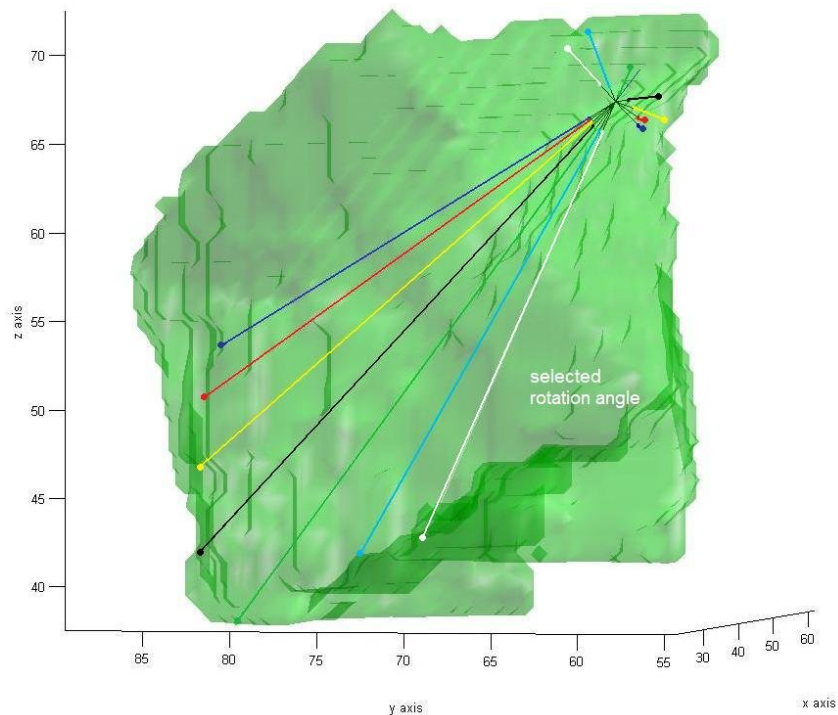

Figure 6-2: The planar rotation selection process within a single segment. The symmetric airways, shown as black skeleton lines, are taken in 20° intervals. The extension lines are in different colours, each colour defining a single pair of daughters.

The planar rotation angle is selected based on the principle that the two daughters have to supply equal volumes within the lung space. The planar rotation dynamic selection method employs the length and branching angle of a symmetric daughter pair as calculated in the previous paragraph. Using the translation routine described above, all possible symmetric daughter pairs with the specific length and branching angle morphometry but with the planar rotation angle varying within the range $\varphi \in \mathbb{Z}\{20, 21 \ldots 160\}$ are created. After that, the daughter vectors are obtained for each pair and a lung-edge detection process similar to the one described in Section 5.3.3 is implemented, with the major difference that the vector extension routine this time begins at the start-point of the daughters. This can be observed in the image of Figure 6-2. The distances between the daughter start points and

154

their respective edge points, which are used as an indication of the local lung shape, are calculated and stored in a table; then, the ratio between these distances is estimated for each pair.

The planar rotation angle can now be chosen as the angle associated with the ratio closest to 1, i.e. when the two sibling airways seem to supply roughly similar spaces in the lung volume. Furthermore, a distinction between which daughter should be major and which minor is made by evaluating which of the two daughters consistently provides with air larger regions of the lung. This is done simply by estimating the extension lengths throughout the angular range and comparing their mean values. The daughter with the highest mean extension length is selected to be the major daughter pair. An important note needs to be made at this point since, in case one of the airways lies outside the confining space, the process described earlier cannot be applied. Therefore, a random $\varphi=90^{o}\pm45^{o}$ with daughter symmetry is used for the development of the rest of the resulting sub-tree.
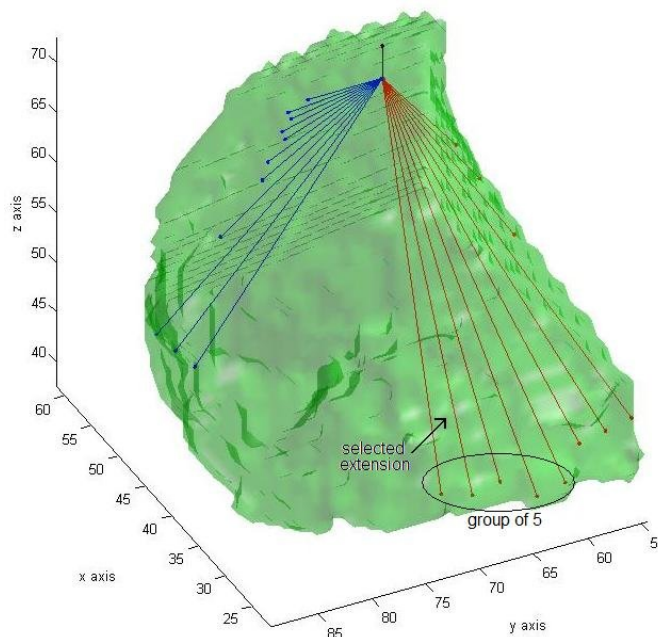

Figure 6-3: The branching angle selection process. All branching angles on a plane are used to create a family of extension vectors. Groups of 5 are then used to obtain mean extension lengths and the extension with length closest to the mean is used to identify the relevant branching angle.

In the case where the symmetric daughters lie outside the segmental confining space, the daughter-pair coordinates are stored in the relevant rows of the generation table and the process restarts for the next parent in the table. Otherwise, the algorithm continues with the calculation of the morphometric data for an asymmetric branching pair. Again, the diameters are calculated first, using equation (6.4a) for the major daughter and the combination of equations (6.5) and (6.6) for the minor daughter. The relationship (6.2) is utilised for the length while the planar rotation angle retains the value computed above. Since the values calculated by equation (3.10) reveal intensely asymmetric behaviour, a more comprehensive way, resembling the method used for the estimation of the planar rotation angle, is chosen for the exploration of the best possible branching angles. The values of the branching angle θ found by (3.10) are first normalised with the angular data obtained in the literature, namely the angular ICRP and Tawhai data, shown in Tables 6.1 and 6.2. Then, the angular ranges $\theta \pm 20^o$ are examined; for each daughter separately, a vectorised version is created and an edge-detection routine is applied on its extension vector (again see Section 5.3.3). The lengths of the extended vectors are stored in a table and are investigated in groupings of 5 consecutive values. The group with the highest group-mean-extension length is assumed to be optimally oriented for the purpose of supplying with oxygen as large a region of the lung as possible. Therefore, the branching angle of the group that is most closely associated to the highest mean extension-length found is selected as the optimal branching angle for the specific airway. Parts of this process can be observed in Figure 6-3.

After the final morphometric features of both sibling airways have been obtained, the translation routine is applied for the generation of the finalised daughter pair. The start- and end-coordinates of the newly estimated airways are stored in their respective columns in the generation table. Furthermore, a second table is created to store the conclusive morphometric values used for this branching pair. The process is then repeated for the next parent airway in the generation table until all airways up to generation 15 are

created. A detailed flow chart describing this algorithm is available in Appendix A1.
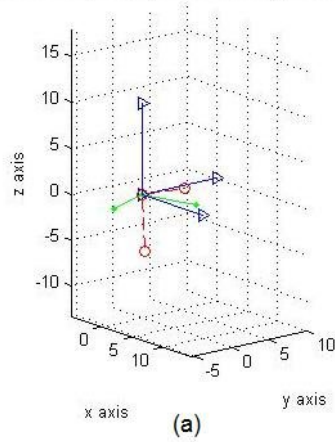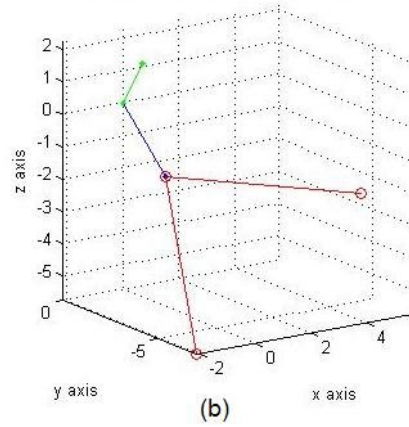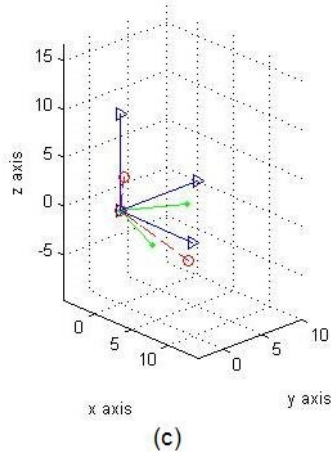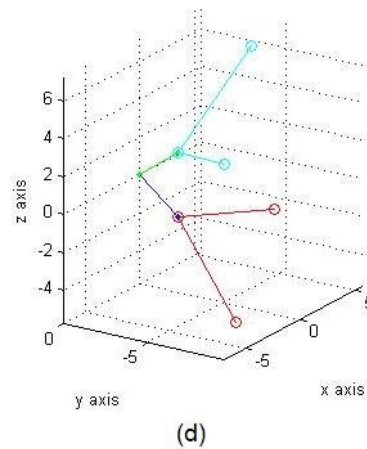
Figure 6-4: The morphometry-to-coordinates translation process. (a) and (c) display the preliminary rotation, with the blue lines being the normal axes, the green lines being the airways on the x-y plane and the red doted lines being the same airways rotated around the normal x axis. (b) and (d) show the final results, with the blue and green lines showing the parents and the red and cyan the resulting daughters.

Results

Figure 6-4 presents a display of the morphometry-to-coordinates translation routine. It is obvious from the (a) and (c) images that the relative angles in the family of airways remain equal throughout the process. More specifically, vector calculus is used to estimate the branching angle after the rotations are performed in order to confirm that no distortion is introduced to the general morphometry due to the implementation. The blue lines denote the axes of a normal orthogonal Cartesian system, while the green lines and the red dotted lines represent the skeleton of the daughters on the x-y plane and the rotated daughter plane respectively. Furthermore, no plane-tilting or misplacement behaviours are noted in the final results shown in (b) and (d). The same conclusion can be reached through observations of Figure 6-1 images of the axial and planar orientations of the normal and the target coordinate system.

Examples of the full results of the unconstrained-tree creation algorithm are shown in Figure 6-5. Four different segments with characteristic shapes, as computed by the Segmental Model, are displayed in this figure, two for the Right and two for the Left lung. The images are also shown using the same camera orientation to enable comparisons about shape and space. In all images, the tendency of the generated tree to obtain a spherical shape is obvious, especially in images (b), (c) and (d). However, in (b) and (d) whole sections of the created subtrees fall outside the segmental space, while in (a) and (c) the subtrees lie roughly inside their associated spaces. Furthermore, the fact that the sub-tree structures are purposefully constructed to follow the local shape of the segments for as many iterations of the algorithm as possible is clearly evident in image (a), where the upper part of the tree displays a relative flat airway configuration, and in image (b), where some of the airways in higher generations are uncharacteristically elongated in an effort to fit the space occupied by the segment more efficiently.
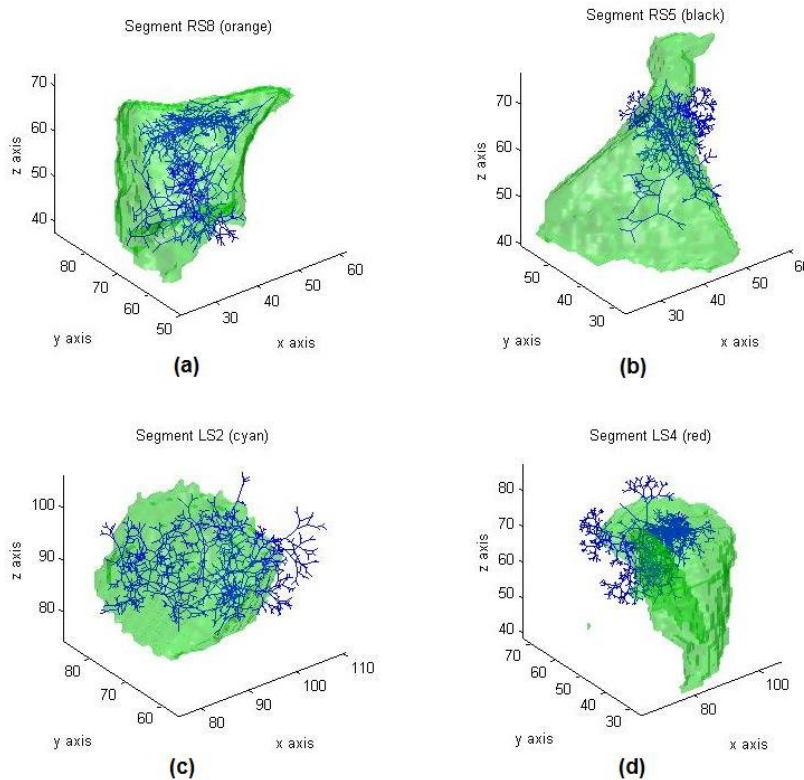
Figure 6-5: The unconstrained tree for 4 different segments.

Figure 6-6 displays 3 graphs expressing the computed morphometry of the unconstrained tree structure. The first graph shows the airway diameter per generation as calculated by the unconstrained tree algorithm for 4 randomly selected pulmonary segments. Comparisons can be made with some of the models available in the literature, such as the ICRP (1994) model and the model developed by Soong et al. (1979). The second graph represents the mean branching angle per generation for the same 4 segments as above and the ICRP model, while Figure 6-6 (c) contains the means and standard deviations for the planar rotation angles calculated for 5 segments of the unconstrained tree.
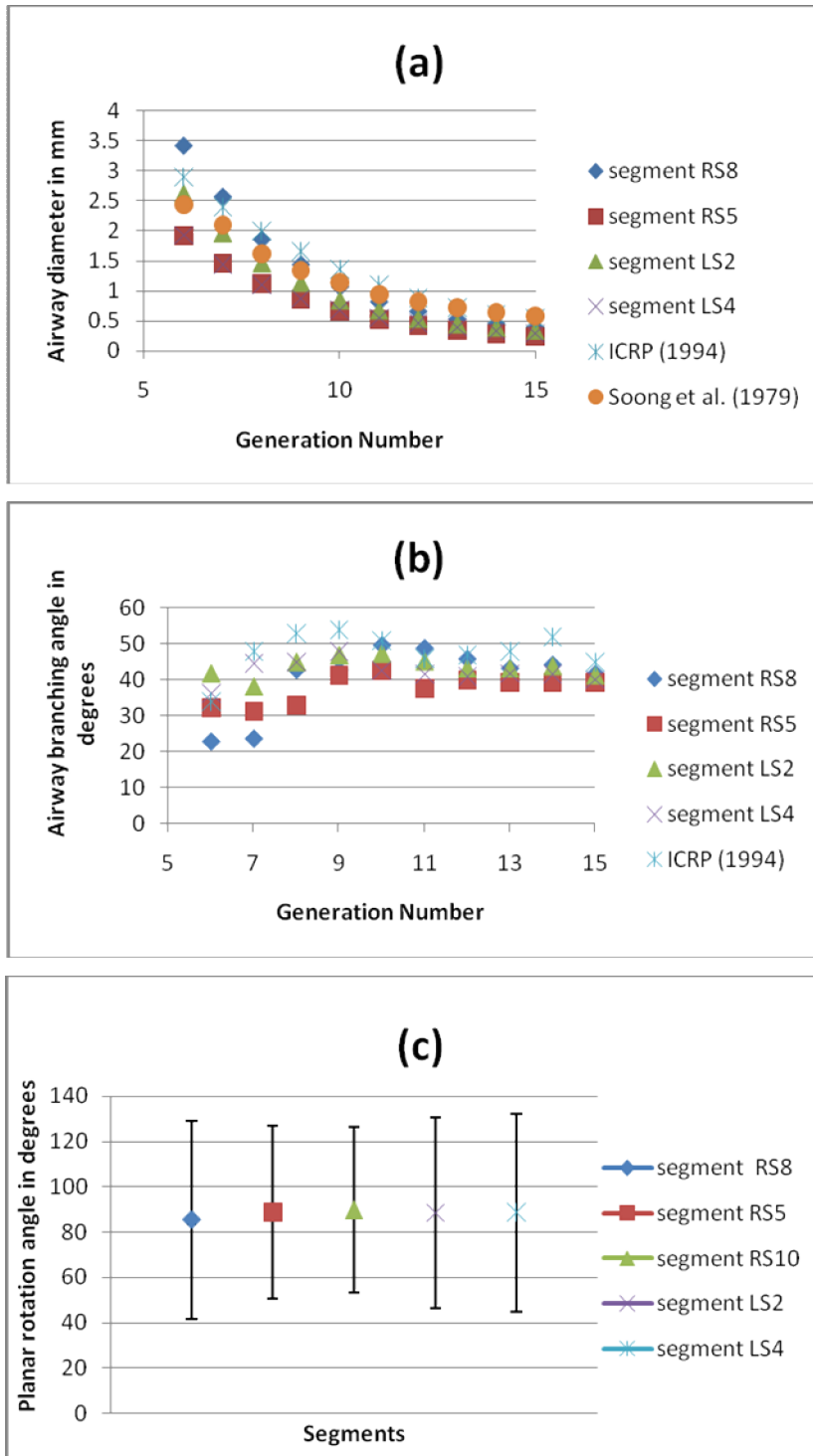
Figure 6-6: (a) The mean diameter per generation, (b) the mean branching angle per generation and (c) the mean value and standard deviation of the planar rotation angle for 5 segments in the unconstrained tree and some of the literature data.

It can be observed that the diameters calculated by the unconstrained-tree methods compare well not only between separate segments on which the process was applied but also with the literature data. With the exception of generations 6 and 7, segments RS5, LS2 and LS4 retain very close mean diameter values, something true for segment RS8 for airways after generation 11. Furthermore, the values determined by the two literature models seem to be consistently higher than the estimated segmental data of RS5, LS2 and LS4 (for the whole range of generations) and RS8 (after generation 11). However, even though some variation exists, all datasets follow similar patterns describing the decrease in diameter size relative to the airway depth in the lung.

The mean branching angles per generation (Figure 6-6 (b)) display a tendency for virtual stabilisation to values around 42°. This can be seen to be a valid assumption especially after generation 9. Even though variability within the range 20°-50° exists between the segmental and the literature data, with the ICRP branching angles almost consistently higher than the angles estimated by the unconstrained tree, there is again good agreement between the different datasets. The same is true for the planar rotation angles of Figure 6-6 (c), which are shown to compare well with the values calculated in the literature (Sauret et al. (2002), Tawhai et al. (2004)) and with the intuitive notion that the planar rotation must be close to 90°.

Discussion

In the two graphs of Figure 6-6 (a) and (b) it can be seen that the larger variations exist primarily prior to generation 9. Even though this can mostly be attributed to inter- and intra-subject variability, it can also be ascribed to the routines developed for the creation of region-specific, unique bronchial sub-trees. Furthermore, the unconstrained nature of the modelled airway tree and the methods for calculating morphometry once outside the confining segmental space in particular, are also an important factor for the relative fading of this variability in the more distal regions of the lung. Since the

airways generated outside the segmental space are considered to be symmetric, due to the lack of criteria for major and minor daughter selection, and their morphometry is unconnected to the local shape of the lung, i.e. their associated segment, the relevant calculations tend to conform to patterns specified by previous literature models. This has as a result that segments coming from different portions of the lung obtain similar morphometries after their trees start developing without even the indirect control imposed by the angular selection process.

Figure 6-5 reinforces the point made above. It can easily be seen that the sub-trees lying inside their designated segmental spaces maintain a unique structure closely related to the local lung shape while the ones outside these spaces are more symmetric and tend to obtain mostly spherical shapes. Even though the satisfaction of some conditions was necessary for the development of the tree, expressed mostly by the branching and planar rotation angle assessment routines, the main purpose of the unconstrained tree algorithm remains the generation of a bifurcating structure that can be readily modified in the subsequent sections to fit the lung space. The imposed indirect control, hence, is merely an effort to develop the tree in such a way as to reveal the general tendencies of the tree configuration in different portions of the lung, with the afterthought to reduce the resources necessary for the space-fitting process that takes place in Section 6.3.4. As such, the results disclose a reasonable level of variability and they also compare well with other datasets, confirming that the unconstrained tree algorithm functions as expected.

6.3.3 Envelope Space Calculation

In the previous section an unconstrained tree structure was developed. The main goal of the Deterministic Algorithm is to modify this structure spatially so as to fit the segmental space as efficiently as possible. For this to become possible, the space occupied by the unconstrained tree first needs to be identified before any shape-fitting may occur. The area covered by the

created with
nitro PDF professional
download the free trial online at nitropdf.com/professional

airway tree is referred to as the Envelope Space and its estimation is the aim of this section.

Methods

In order to assess the space covered by the modelled airways of the unconstrained tree, the surface of the volume containing these airways needs to be identified. This is done with the help of the branching points of the tree, given by the generation table calculated above; the volume of any 3D object can be defined with the help of a collection of points that belong within the space of the object, with the points adhering to a common coordinate system with a fixed origin point. Using these points, the minimum outward-bending surface enclosing such a volume, also known as the convex hull of the object, can be calculated using well-established algorithms that exist in the literature. The algorithm used for the computation of the convex hull (Barber et al. (1996)) is readily available as an integrated function of the MATLAB version 6.5 software package that was used throughout this study. A 2D example of the algorithm can be seen in Figure 6-7 for the results of a test function.
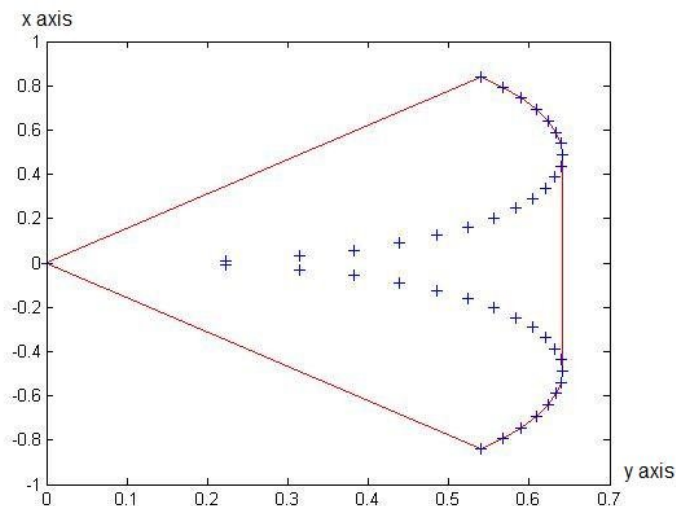
Figure 6-7: A 2D representation of the convex hull process. The dataset points are displayed in + while the red line defines the optimal region enclosed by these points.

The algorithm basically functions by identifying the outer-surface points of an object and their connectivity. For any concave 3D object, the most efficient way of doing this is by carving the surface into discrete triangular elements, each triangle having as edges the 3 dataset surface points that most accurately describe the local volume of the enclosed space. i.e. the 3 points closest to the centre of mass of the respective triangular facet. The output of the convex hull estimation process is an index table with dimensions mx3, with m being the number of facets forming the surface and with each column used for the storage of an index number that represents the position in the generation table the coordinates of the triangle edges are stored in. An application of the convex hull on the region identified by a segmental tree can be observed in Figure 6-8(a). Figure 6-8(b) displays more clearly the triangular form of the facets enclosing the segmental region of interest.
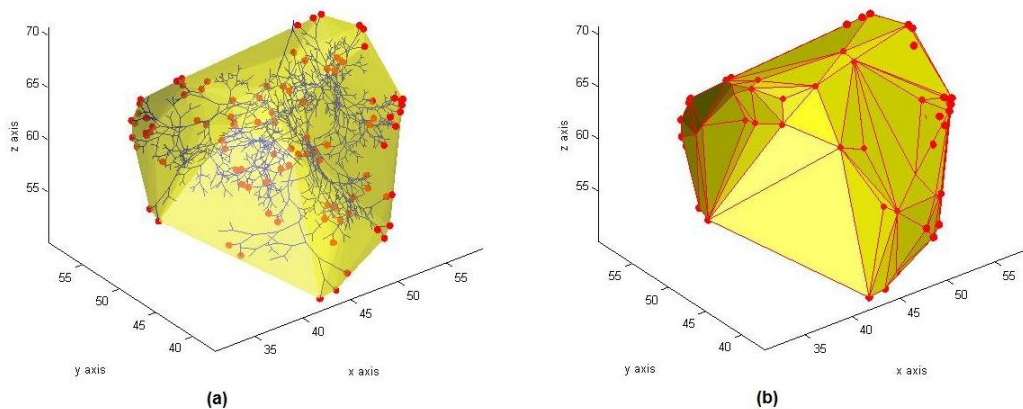
Figure 6-8: (a) The unconstrained tree skeleton and the relevant convex hull. (b) The convex hull and the vertices and edges of the triangle facets. Both images are shown from the same perspective and the red dots represent nodes connecting different triangles.

T

he result of the convex hull algorithm then needs to be transformed into a binary 3D matrix, similar to function and size to the matrices used to accumulate the segmental space data. In other words, a digitisation process needs to be performed on the surface triangles and the volume they enclose. A method was developed to achieve that, during which each surface element is treated separately. After the facet has been isolated and its edge coordinates located within the generation table, as shown in Figure 6-10(a), a similar triangle ABC is created on the x-y plane of an orthogonal Cartesian

164

coordinate system, with point A on the origin, edge B on the x axis and edge C on the first quadrant of the axial system. The linear equations expressing the vertices connecting the edges AC and BC are then identified and the height of the triangle (the distance of C to the x axis) is calculated. The height is then turned into a discrete number equal to the closest integer still within area enclosed by the triangle ABC. For each value of $y \epsilon \mathbb{Z}\{0, 1 \ldots height\}$, the points on the two lines defined by the points AC (x_{min}) and BC (x_{max}) are calculated and then transformed into their closest integer values (Figure 6-9 (b) and (c)). All points P(x,y), $x \epsilon \mathbb{Z}\{x_{min}, x_{min} + 1 \ldots x_{max}\}$ are then store in a separate table (Figure 6-10(b)).

After all the discrete points constituting the ABC surface have been computed, a rotation process similar to the morphometry-to-coordinates translation routine used in the previous section is performed on this new set of 2D surface points. The edges of the original surface facet are vectorised and a new axial system is identified through them, as displayed in Figure 6-10(c). The 2D point dataset is then rotated to become 3D and then its newly calculated elements are re-discretised to obtain their closest integer values for all dimensions. This results in the non-planar triangle of Figure 6-10(d). The last step of this process includes the displacement of the discrete 3D dataset to the original coordinate system of the convex hull, where the surface facet is now characterised by the new discrete dataset and not just the 3 edge points.

The points of the final dataset represent the coordinates of the surface voxels of the convex hull. For that reason, a 3D matrix of equal dimensions with the segmental-space matrix can now be created and all the voxels coinciding with the dataset points obtain the value of 1, thus forming a discrete binary surface for the envelope of the unconstrained tree. Even though the convex hull may now be considered to have obtained its final form, some major modifications need to occur before its results can be used in the main Deterministic Algorithm.

created with
nitro PDF professional
download the free trial online at nitropdf.com/professional
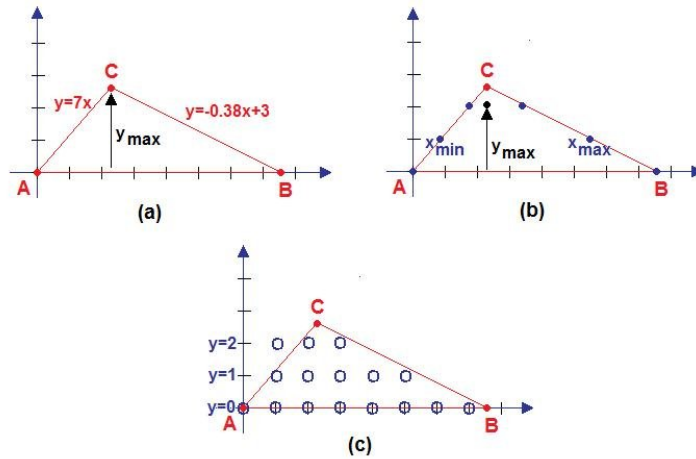
Figure 6-9: The 2D triangle surface digitisation process. (a) The original face is turned into a 2D triangle and the linear equations are identified. (b) The maximum and minimum are found for the ranges allowable for the discrete points. (c) The final discrete form of the 2D dataset (in blue circles).
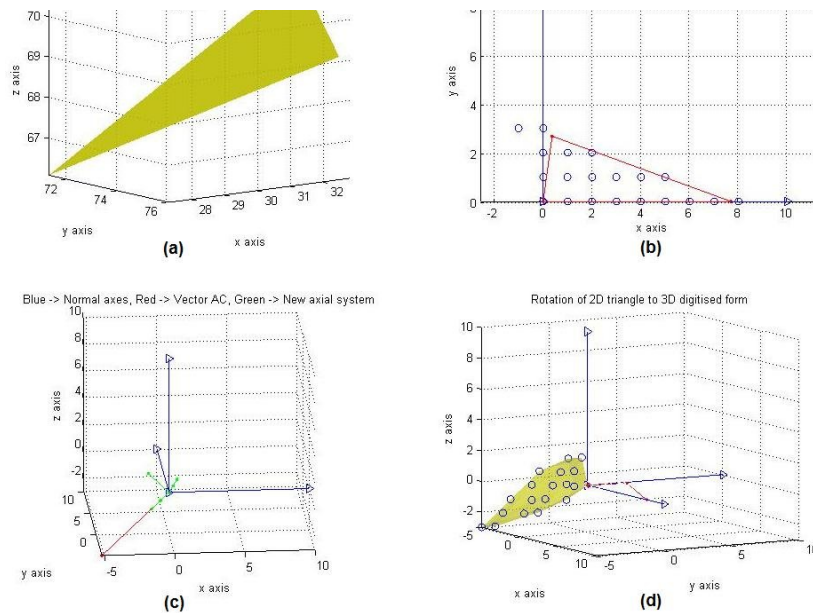
Figure 6-10: The discrete convex hull creation process. (a) The original surface facet. (b) The discrete points of the 2D triangle. (c) The axial system used for the rotation of the discrete 2D dataset (in green) and the x-axis forming line (rotated line AB in red). (d) The 2D planar form of the triangle and its rotated discrete 3D form along with its equivalent formation points.

166
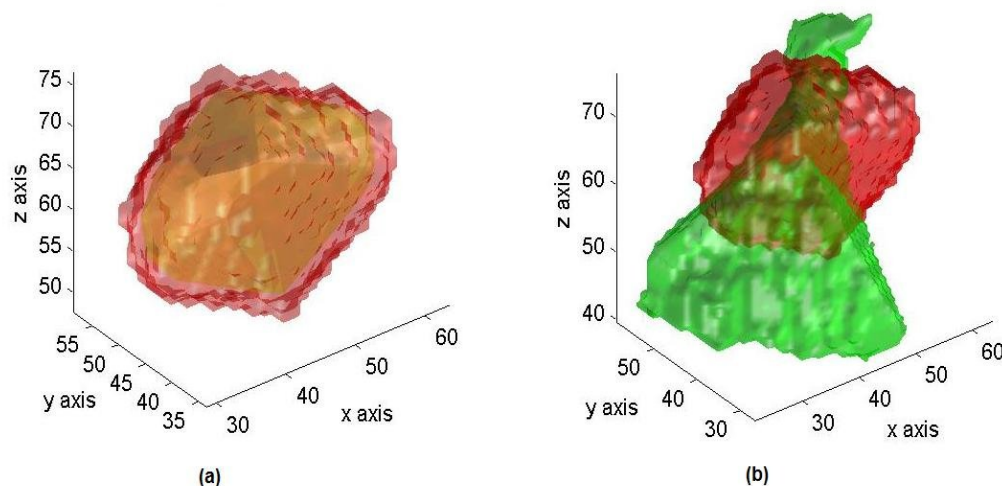
Figure 6-11: The results of the envelope space process. (a) The convex hull (yellow) and the resulting envelope space (red). The envelope space is the voxelised version of the convex hull space. (b) The envelope space (red) and the real segmental space (green).

Due to the discrete form of the calculated convex hull and, more specifically, because of the rounding of the coordinates of the points in order to obtain their relevant integer coordinate values, some surface voxels may have been omitted or overlooked, which results in an incomplete hull that cannot define a closed-space volume. Furthermore, some consideration needs to be given to the extra space necessary for the accommodation of the finite space used by the acini in the human tracheobronchial tree. Since the convex hull is estimated by considering only the first 15 generations of the tree, no such allowance was made initially, even though the acini, according to the data of Haefeli-Bleuer et al. (1988), have a mean diameter of at least 3.5mm if considered to be spherical in shape. Both these problems can be addressed with the application of a simple 3D cubic filter on the surface voxels. The filter is a 9x9x9 matrix which is convolved with the matrix containing the discrete convex hull, thus filling the hull voxels plus their two neighbouring voxels in every direction with non-zero values. The filtering process results in a robust outer surface for the unconstrained tree, which can now easily be filled in order to simulate the envelope space. The results of the filtering and the space-filling process are displayed in Figure 6-11, while a detailed flow-

created with
nitro PDF professional
download the free trial online at nitropdf.com/professional

chart of the process used for the estimation of the envelope space is available in Appendix A2.

Results And Discussion

Figure 6-8 displays the convex hull generated around a tree structure along with all the surface points selected by the hull algorithm. It is obvious from image (a) that parts of the tree configuration are more elongated, hence, on some occasions, there exist some "hollow" spaces (regions unoccupied by the airways) between sub-trees that lead to surface points. This effect becomes especially apparent where the convex hull is flatter than usual; these areas are characterised by very large triangular surface elements, such as the ones illustrated in Figure 6-8(b). Furthermore, it can be seen in Figure 6-11(a) that even though the process for transforming the convex hull into a discrete volume is relatively complex, the resulting space completely envelopes the theoretical surface of the tree, hence the name envelope space given to the final product of the procedures described in this section.

It could be argued that simpler techniques should be used for the exploration of the envelope space since, due to its complexity, the current one might require more resources than strictly necessary. Moreover, during the discretisation of the surface triangles (Figure 6-10(d)), some voxels may be overlooked, which constitutes the utilisation of a filtering routine essential to the creation of a robust, shapely and concave surface. However, this filtering has the effect that not only the voxels forming the hull but also their neighbours are selected to form the final space. Although this turns out to be an advantage in the specific process, as the accommodation of acinar regions has to be taken into account, the whole process might not be viable in applications where increased resolution, and hence increased accuracy, is required.

An alternative process would involve the direct implementation of simultaneous space-filling routines throughout the nodal composition of the

created with
nitro^PDF professional
download the free trial online at nitropdf.com/professional

tree structure. Nonetheless, such routines would have the distinct disadvantage of imprecise stopping conditions. Even more importantly, in regions where relatively high distances exist between sub-trees, there would be a high probability that the voxels situated in these areas might be ignored. These two problems are successfully addressed by the current algorithm. Furthermore, while complex, the execution of the procedure is based on well-established processes that consume considerably less time and computer power than expected. For these reasons, the algorithm developed for the identification of the envelope space is considered to produce valid and reproducible results that can be immediately used in the subsequent parts of the Deterministic Algorithm.

6.3.4 Expansion And Dilation Of The Unconstrained Tree

As seen in Figure 6-11(b), there is often considerable difference between the envelope space and the modelled segmental space. This section describes the development of a space- and shape-fitting algorithm that has as a goal to transform the unconstrained tree in order to fit the segment established on these spatial differences.

Methods

The space-fitting process is developed iteratively from the central airways towards the more distal parts of the lung. The inputs for this process are all the results of the algorithms discussed in the previous 2 sections, i.e. the generation table and the envelope space, plus the segment space as found by the Segmental Model. Starting from the first possible family of airways in the unconstrained tree structure (generation 5 parent plus its two generation 6 offspring in the current dataset) a straight line is extended from the parent tube and a routine similar to the one discussed in section 5.3.3 for the detection of the periphery of the constraining space is applied; however, two edges are now necessary, one for the segmental space (P_{seg}) and one for the envelope spacer (P_{env}). The distance between the branching node and these

created with
nitro PDF professional
download the free trial online at nitropdf.com/professional

two points (d_{seg} and d_{env} respectively) is then calculated. The difference between these two distances represents the spatial variation to which the two daughters need to adapt to.
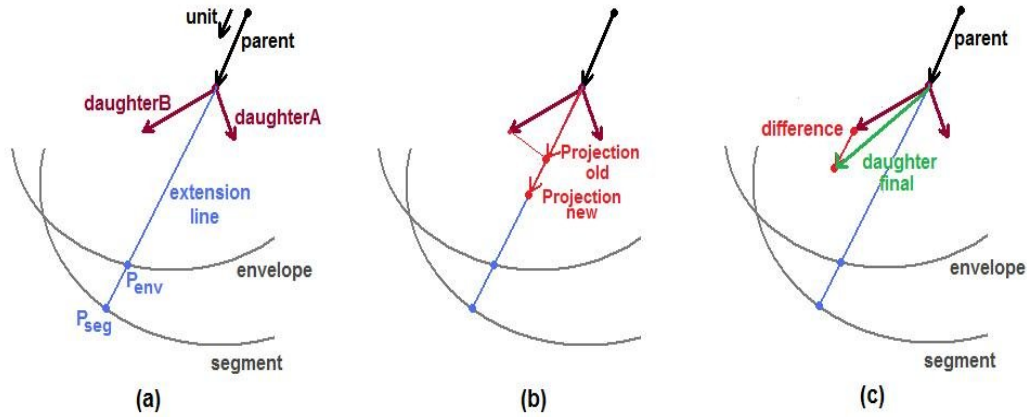
Figure 6-12: An iteration in the Expansion-Dilation algorithm. (a) The extension from the parent and the detection of the edge points. (b) The identification of the old projection vector and the calculation of the new projection vector. (c) The use of the difference vector to calculate the final daughter.

for each daughter ($\overrightarrow{daughterA}$ and $\overrightarrow{daughterB}$). The vector $\overrightarrow{parent}$ is normalised to produce a unit vector which maintains the same directionality,

$$\overrightarrow{unit} - \frac{\overrightarrow{parent}}{\left|\overrightarrow{parent}\right|} \text{ (6.17)}.$$

Each daughter vector is then projected on the extension line forming two new vectors, $\overrightarrow{projectionA_{old}}$ and $\overrightarrow{projectionB_{old}}$, whose lengths are estimated. These lengths are subsequently modified based on the difference between d_{seg} and d_{env}, which are used in the equation

$$\left|\overrightarrow{projectionA \text{ or } B_{new}}\right| = \left|\overrightarrow{projectionA \text{ or } B_{old}}\right| \frac{d_{seg}}{d_{env}} \text{ (6.18)},$$

and the difference vector between the new and the old projection is also calculated:

$$\overrightarrow{difference} = \left|\overrightarrow{projectionA \text{ or } B_{new}}\right| * \overrightarrow{unit} \quad \left|\overrightarrow{projectionA \text{ or } B_{old}}\right| * \overrightarrow{unit} \text{ (6.19)}.$$

This newly estimated $\overrightarrow{difference}$ vector is finally added to the daughters in order to generate the vector of the final daughter airways:

$$\overrightarrow{daughterA \ or \ B_{final}} = \overrightarrow{daughterA \ or \ B} + \overrightarrow{difference} \ (6.20).$$

Having identified the final vectors of the daughters, all morphometric information can be extracted for the new pair, i.e. their diameters, length and branching angles. Notably, the planar rotation angles remain the same as in the unconstrained tree. The consecutive steps of the above process can be seen in the images of Figure 6-12.

The new directionality of each of the daughter airways alters the orientation of the entire sub-tree originating at them, thus resulting in a new envelope space that should be used for further iterations of the Expansion-Dilation algorithm. For that reason a routine similar to the one employed for the creation of the unconstrained tree is utilised for the determination of the new tree structure, which replaces the existing structure in the generation table before the Envelope Space algorithm is applied on it. The new table and envelope space form the inputs for the next iteration of the procedure, which goes on with the next family of airways in the generation table. Each iteration stops only if one of three conditions is met; the first one requires the parent vector to lie inside the segmental space as no extension to the edge can be performed otherwise. The second condition characterises the necessity for some empty space at the distal parts of the lung in order to accommodate the acini. Hence, in cases where $d_{seg}<2mm$, the sub-tree originating at that parent is erased. The final constraint places a restriction to the size of the airways, as only the air-conducting portion of the airway tree is simulated by the Deterministic Algorithm. Therefore, when airways with diameters smaller than 0.35mm are reached, the iteration discontinues. All iterations that are bound to form sub-trees of the airways not meeting the aforementioned conditions are skipped. The algorithm finishes its operation when all airways in the generation table have been accounted for and no further modifications can occur.

created with
nitro PDF professional
download the free trial online at nitropdf.com/professional
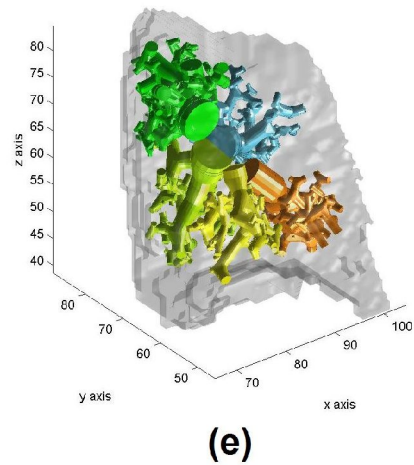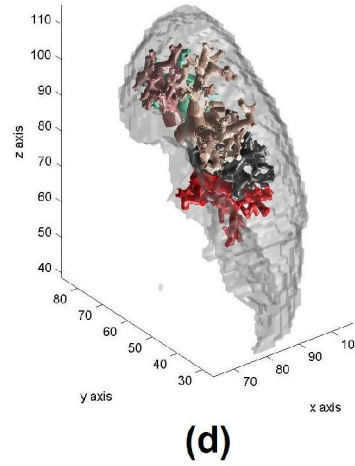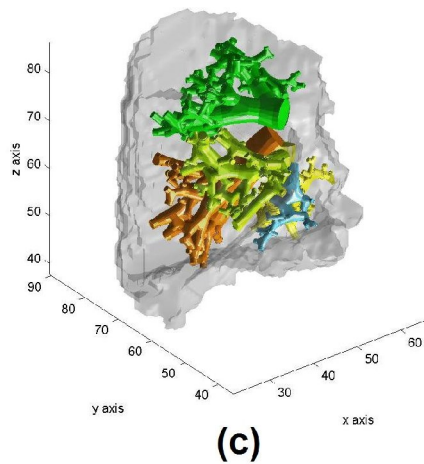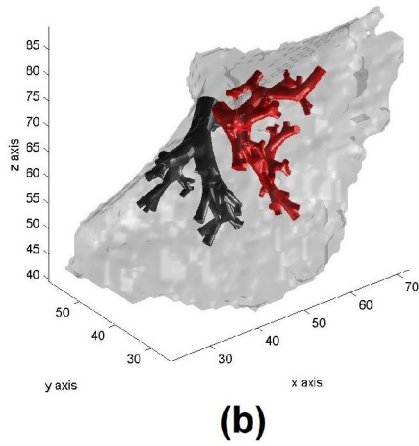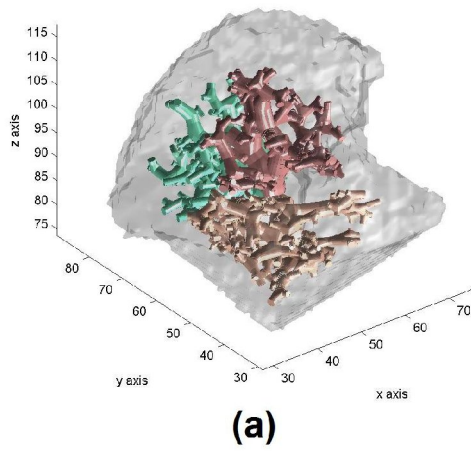
Figure 6-13: The airways of the first 11 generations of each segment as predicted by the Deterministic model. Each airway is represented by a single cylinder and all cylinders that belong to the same segment are shown in the same colour. The tubular systems are displayed in their lobar groupings: (a) RU Lobe, (b) RM Lobe, (c) RL Lobe, (d) LU Lobe and (e) RL Lobe.

Results

The images in Figure 6.13 show a 3D recreation of the airways between the segmental root and generation 11 of the airway tree as predicted after the implementation of all the steps of the Deterministic Model. The airways that belong to the same segment are displayed in the same color, and the colors are chosen based on the relevant selection of segmental colors described in Section 5.2 and shown in Figure 5-8. This allows the easy demarcation of the tree structural units. For reasons of convenience, the airways are displayed in lobar groupings. All lobes are shown from the same point of view in the 3D space and the axial system is included in the images for easy reference to the size and volume occupied by each segment in each lobe. The airways of each segment can be seen to cover the lung space almost homogeneously and the configuration of each sub-tree is clearly visible through these images. No extreme morphometries can be observed as a certain amount of symmetry and some moderate variability are apparent throughout the bifurcating structure. Furthermore, the binary configuration of the sub-trees is designed to follow the local shape of the lung, which seems to be the case in all the visible regions of the confining space.
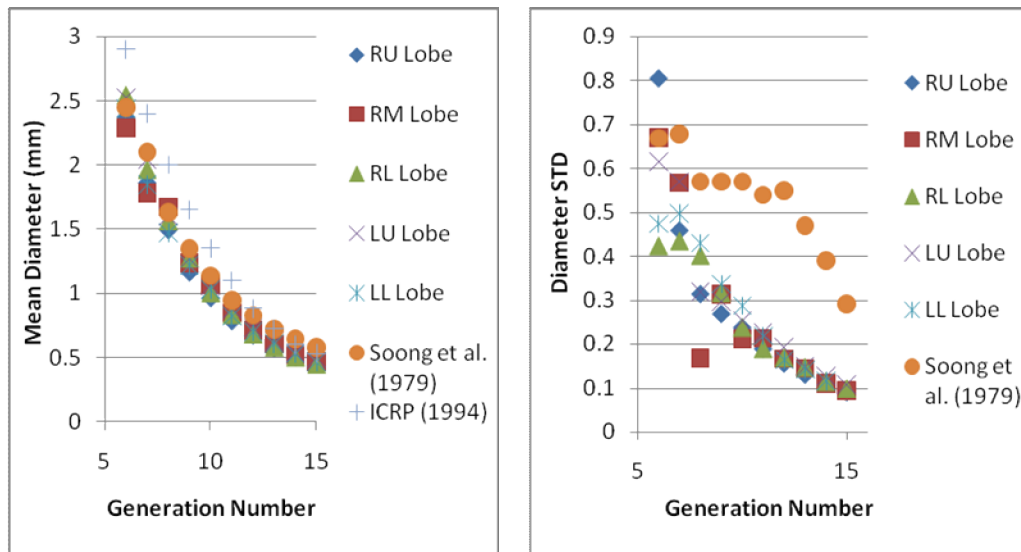
Figure 6-14: The diameter mean and standard deviation per generation per lobe for the Deterministic Model and the literature data of Soong et al. (1979) and the ICRP (1994).
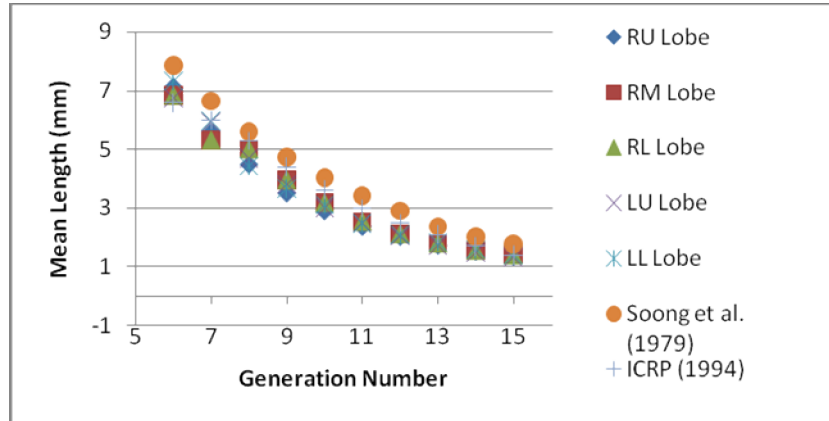
Figure 6-15: The mean length per generation per lobe for the Deterministic Model and the literature data of Soong et al. (1979) and the ICRP (1994).
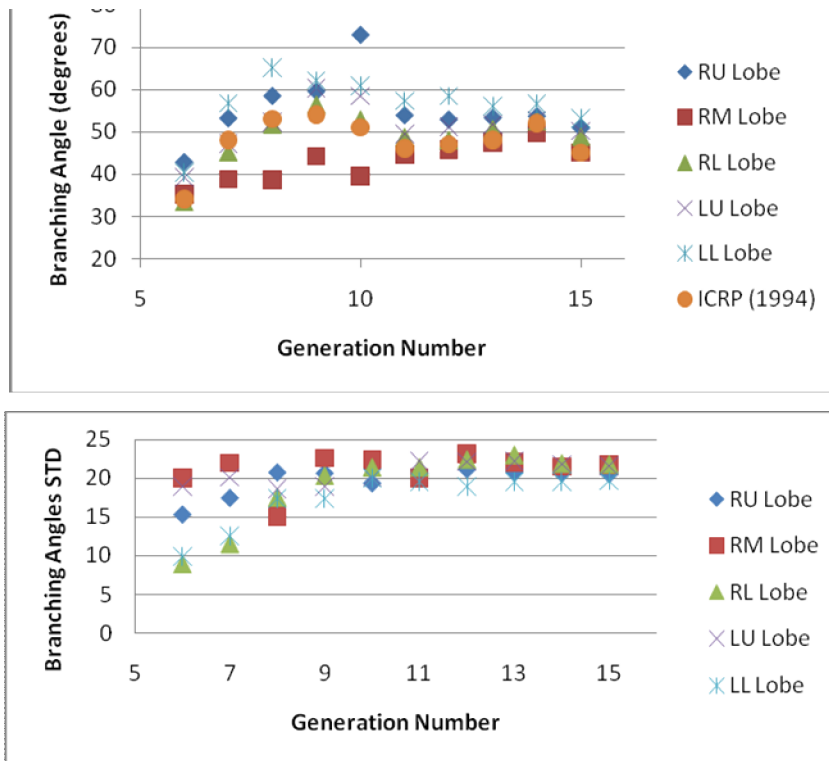
Figure 6-16: The mean branching angles and standard deviations per generation per lobe for the Deterministic Model and the literature data of ICRP (1994).
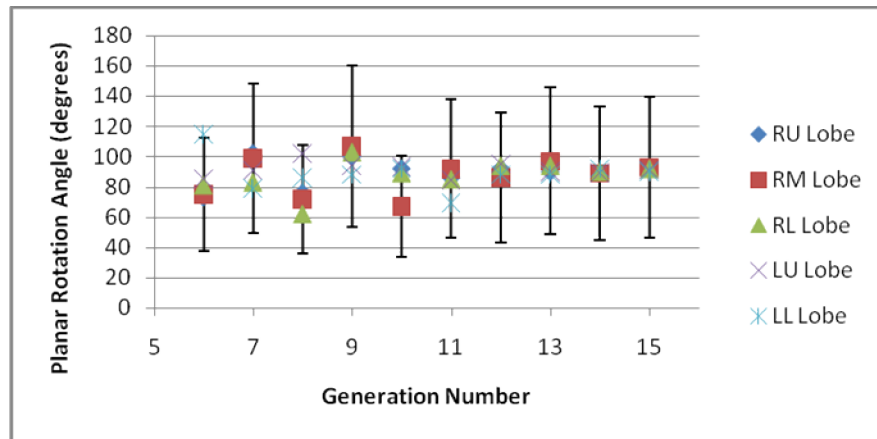
Figure 6-17: The mean planar rotation angle per generation per lobe
for the Deterministic Model. The standard deviation for the RM lobe
is also shown.

Figure 6-14 presents the mean values and standard deviations (STD) of the
diameter per generation per lobe for the Deterministic Model. For comparison
purposes, some literature data are also included in the graphs. It has to be
noted that, even though the morphometric data are available for each
segment separately, in this instance they are displayed in lobar groups in
order to enable visual comparisons. Furthermore, the diameter and length
values for the model are normalised to a lung volume of 3300ml to render the
evaluation of the data meaningful. It can easily be observed that the mean
diameters calculated by the Deterministic Model are slightly underestimated
in comparison to the literature data. This underestimation is in the order of
10-15% between the current model and the ICRP (1994) data and less than 5%
between the model and the Soong et al. study of 1979. The disparity becomes
less apparent the deeper the airways penetrate into the lung as the reduction
in diameter with respect to generation number follows the same pattern for
all datasets. However, important differences can be seen in the STD graph,
since the model STDs are considerably lower than the ones predicted by
Soong. The diameter standard deviations of the Deterministic Model seem to
follow a pattern of value reduction (with respect to the generation number)
similar to the one followed by the mean values, while Soong calculated
almost steady STDs between generations 7-11 and then approximately linear
decrease the deeper the airways penetrate into the lung. However, the mean

175

STD difference between the Deterministic and the literature model is close to 0.35mm, which is relatively small and only becomes important for airways close to the distal regions of the lung.

In Figure 6-15 the length per generation per lobe is displayed, again in comparison to two morphometric models that are available in the literature. The values predicted by all datasets are very close, with differences between maximum and minimum values of less than 15%. More notably, it can be observed that the ratio between length and diameter seems to confirm the rule of thumb stating that the length is roughly 3 times larger than the diameter.

The graphs of Figures 6-16 and 6-17 conclude the morphometric analysis of the Deterministic Model by presenting mean and STD values for the branching and the planar rotation angles of the developed bifurcating structure. It can be observed that the branching angles remain within the expected range between 30° and 60° with only two exceptions, the airways of generations 8-10 for the RU and LL lobes, which tend to obtain relatively high angles between 60 and 75 degrees. The angle values given by the ICRP remain close to the mean value per generation for all the lobes of the Deterministic Model. The STD values for the branching angles estimated by the current model also seem to increase from 10° to 20° between generations 6-9 and then the values remain close to 20° for the rest of the dataset. This seems to be in good agreement with the STDs calculated by Sauret (PhD thesis, 2000), who calculated them to be between 20 and 60% of the angle value for the generations 6-9 on a study made on a CT scan of the airways of a lung cast, with a mean value of 45%.

In addition to the above, the mean values of the planar rotation angles are within the range 60°-105°, with the mean value between different lobes starting at 80° in generation 6 and reaching 90° at generation 10, a value which then remains almost steady up to generation 15. The standard deviations for the RM lobe are also present in the graph of Figure 6-17, since

the planar rotation angle values in that lobe seem to be typical for the whole set. The STDs are between 35° in generation 10 and 55° in generation 9, with a general value of 45° throughout the dataset. Similar STD values were calculated for all the lobes. Again, this is in good agreement with previous morphometric studies and modelling efforts that considered a mean planar rotation angle value of 90° with an STD of 45° [Martonen et al. (1995), Sauret PhD thesis (2000), Tawhai et al. (2000)].

Finally, an effort to benchmark the results of the Deterministic Model with the help of the SHCM developed in Chapter 5 is presented with the help of the histograms of Figures 6-18 (a) and (b) and the 3D image of Figure 6-19. Due to space considerations, only two airway generations of the tracheobronchial tree are considered in this section, generations 8 and 11. These two generations were not chosen randomly since they are regarded to be constituent parts of the two typical groupings of airways generated by the Deterministic Model, generation 8 being well inside the air conducting part of the lung and generation 11 being one of the first generations that tends to exhibit any significant alveolation. For the comparison to take place in a meaningful way, the airways needed to be transformed from their cylindrical form to the discrete form in which the SHCM is represented. For that reason, the cylinders were digitised and their volume was stored in 15 separate 3D matrices with linear dimensions equal to the matrix containing the lung space in our dataset (128x128x128). After a shell analysis was performed on the Segmental Model of the lung space, the voxels of the 3D matrices were accumulated per shell for each segment and stored in a volume (V) per shell (i) per generation (j) table (V_{ij} table). The results of this process can be shown on all levels, from whole lung to the segmental level; however, for convenience reasons, they are made available here for the whole of the right and the left lung separately.

Figure 6-18 (a) displays the results of the analysis described above for the table V_{i8}. Special care is given to the fact that the calculated volumes refer to dissimilar number of airways, since the SHCM considers 2^8 conducting

177

airways in generation 8 while the Deterministic Model predicts the existence of only 224 bronchi (Table 6.3 shows the number of airways per generation in each lobe for all airway generations of the Deterministic Model). Furthermore, all volumes have been normalised to a 3300ml lung space. It can easily be seen that both models estimate equivalent volume values up to shell 6. However, the SHCM estimates much higher volumes for both lungs at shell 7 ($500mm^3$ for the right and $200mm^3$ for the left lung) and for the right lung only at shell 8 ($180mm^3$). In addition, some airways are found in shells 9 and 10 for the current model while the SHCM does not calculate any airway presence in those shells. On the other hand, both models seem to agree on the mean shell position of the airways of generation 8, with the Deterministic predicting it within the region between shells 6 and 7 (max at shell 6) while the SHCM spreads it a bit more between shells 6 and 8 (max at shell 7). This is confirmed by the 3D image of Figure 6-19, which shows the cylindrical airways of generation 8 in gray color and superimposed on transverse slices of the Segmental Model of the lung space on which the shell analysis has been executed.

The histogram related to table V_{i11} is shown in Figure 6-18(b). Again, normalisation for the different number of airways (2^{11} in SHCM, 1344 in the Deterministic Model) and for the different lung volumes is implemented. It can be observed that in this generation the SHCM calculates consistently higher volumes per shell than the Deterministic Model, with a maximum difference of $550mm^3$ and $320mm^3$ at shell 9 for the right and the left lung respectively. Still, the mean shell position of the airways is again very close, with the latter model finding it to be between shells 7 and 8 (max at shell 8) whereas the SHCM finds it to be between shells 7 and 9 (max at shell 9). Further analysis of other airway generations demonstrates similar trends, i.e. that the Deterministic Model computes lower V_{ij} but positions the airways in lung spaces comparable to the SHCM.
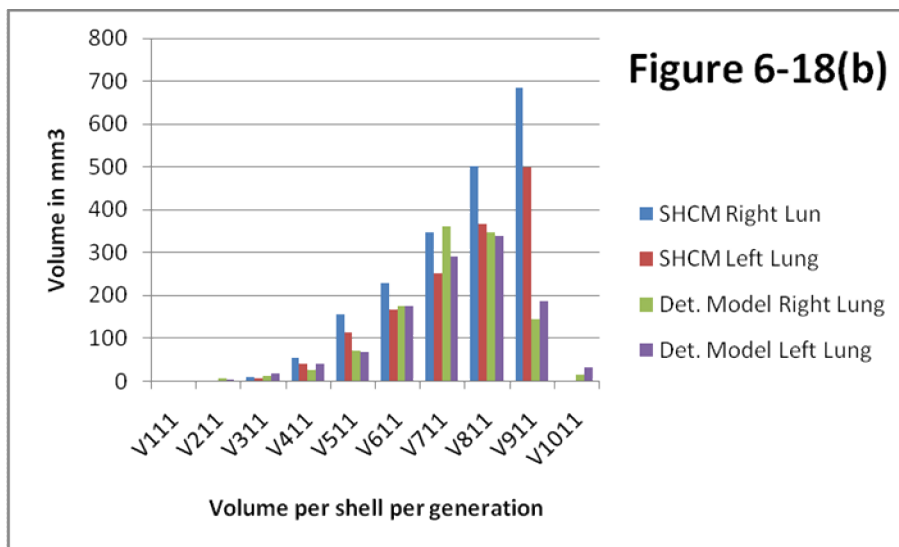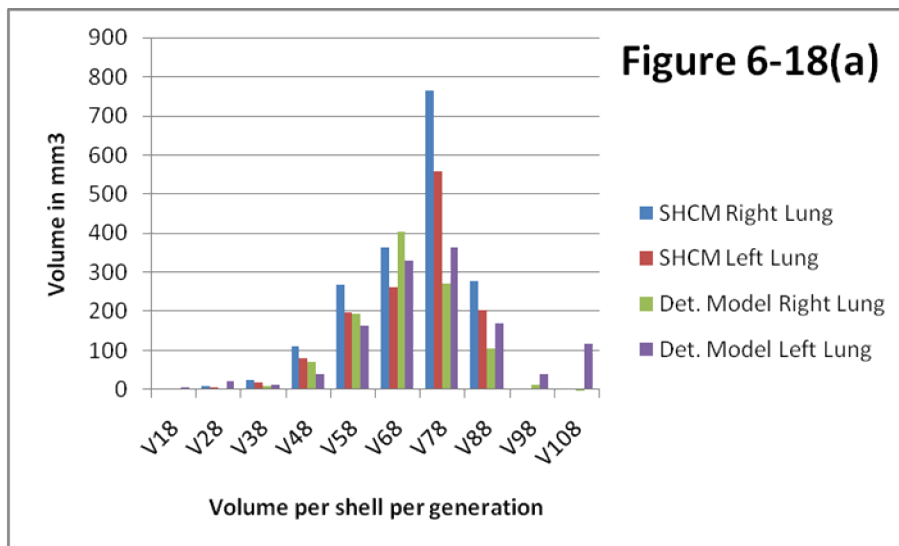
Figure 6-18: Volume per shell per generation for the SHCM and the Deterministic Model for (a) Generation 8 and (b) Generation 11.
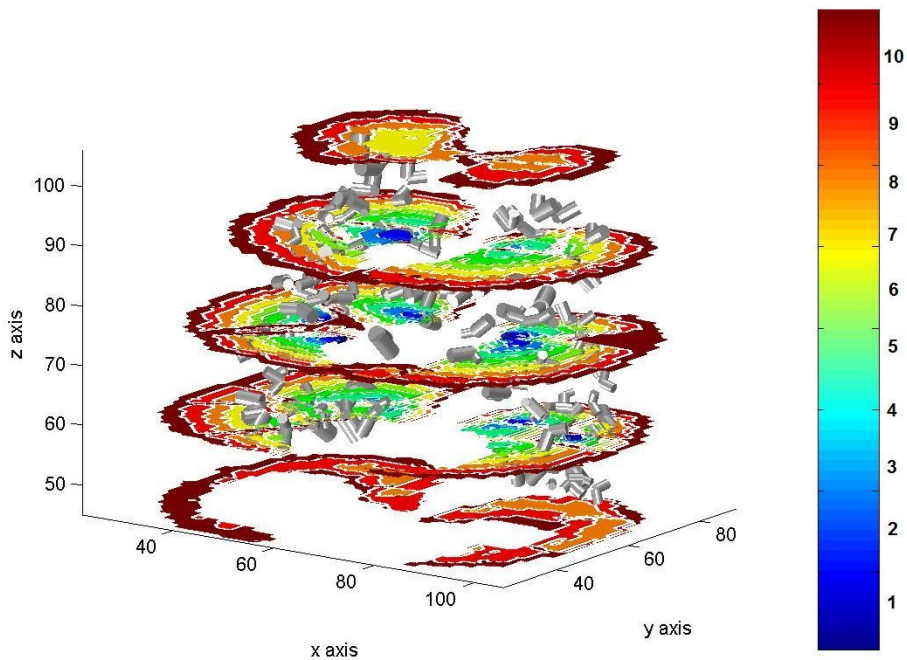
Figure 6-19: 3D representation of the airways of generation 8 as predicted by the Deterministic Model (gray cylinders) superimposed on transverse slices of the Segmental Model of the lung space on which a shell analysis has been performed. The shells are color coded.

Generation number	RU Lobe	RM Lobe	RL Lobe	LU Lobe	LM Lobe
6	16-0	4-0	12-0	16-0	16-0
7	32-0	8-0	22-2	32-0	30-2
8	58-6	10-6	42-2	58-6	56-4
9	114-2	20-0	78-6	104-12	92-20
10	210-18	36-4	146-10	186-22	158-26
11	392-28	70-2	274-18	338-34	290-26
12	738-46	128-12	524-24	626-50	528-52
13	1394-82	238-18	984-64	1157-95	924-132
14	2552-236	428-48	1760-208	1926-352	1551-297
15	4398-706	743-113	2976-544	3243-609	2449-635

Table 6.3: The number of airways and acini per generation per lobe as predicted by the Deterministic Model. Every airway that remains non-calculated by the Deterministic Model in the first 15 generations of the tree is considered to give rise to an acinus.

Discussion

The Deterministic Model results are shown in 3D in the images of Figure 6-13. The fact that the airways (up to generation 11 in this Figure) occupy all the space available to them denotes clearly that the local lung shape becomes important to the growth of the tree. Furthermore, the morphometry of the sub-trees shown in these images seems to be typical of the bifurcating structure of the lung with now extreme changes and differences within similar regions. The fact that acinar structures begin to exist as early as generation 7 (also see Table 6.3) adds to the authenticity of the model, since this form of asymmetry is distinctive of the human lung. This result also agrees with previous models such as the ones presented by Yeh and Schum (1980), Kitaoka et al. (1999) and Tawhai et al. (2000).

When compared to previous studies, the morphometry of the Deterministic Model seems to also be in very good agreement with several literature models. The diameter decline pattern with respect to the generation number, shown in the graph of Figure 6-14, is a characteristic example of this. Since the diameters are generally comparable between the model and the ICRP data, which are basically mean values obtained from several morphometric models available in the literature, the Deterministic Model is relatively close in mean values to a significant number of studies. The same conclusion can be extended to the lengths displayed in Figure 6-15, which also agree very well with many datasets available [Soong et al. (1979), Koblinger and Hofmann (1985), ICRP (1994), Sauret PhD thesis (2000)].

A comparison made between the bifurcation angles of the Deterministic Model (Figure 6-16) and previous morphometric studies also shows that the branching angles of this model associate well with their literature counterparts. With the exception of some specific airway generations which display uncharacteristically high branching angles, a fact in itself not very highly improbable as explained by Koblinger and Hofmann(1985), the rest of the dataset is very close to the mean value of 52 calculated in most projects

for the range between generations 6 and 15 [Tawhai et al. (2000), Sauret PhD thesis (2000)]. The slightly exaggerated angles can be attributed to inter-subject variability, which is an important factor when evaluating different lung morphometries. This becomes obvious from the relatively high STDs, also charted in Figure 6-16, which suggest a very high variability not only between different subjects but also within different regions of the lungs of the same subject. Even though not much data exist on that characteristic of the lung morphometry, the values predicted by the Deterministic Model are very close to what is available in the literature. More specifically, Tawhai et al. (2000) calculated the STD to be close to 20° for a full model of the tracheobronchial tree, while Sauret found it to vary maximally in the range 6°-34° for generation 6, with a mean value of 25° between generations 6-9. The strong angular variability is also evident in the planar rotation angles with a mean of 90° and an STD of 45°, which is equal in all the projects that have investigated this characteristic. It has to be noted that high bifurcation angles indicate that either the airway directionality is against the force of gravity, as is likely in the RU lobe, or that the local space by which the airways are constrained must be flatter than usual, as is the case with some segments in the LL Lobe.

Even though the angular data maintain the expected amount of variability, this is not strictly the case with the diameters. The diameter STDs in the Deterministic Model are estimated to be relatively smaller than the ones estimated in other studies, with most prominent the ones by Soong et al. (1979), Koblinger and Hofmann (1985) and Sauret (PhD thesis, 2000), and they have a more structured decline rate, which is very similar to the decline rate per generation of the diameter mean values. This, along with the fact that mean diameter values are very close in each generation for each lobe, suggests that the tracheobronchial tree structure constructed by the model is relatively more symmetric than necessary. However, the extent to which this symmetry affects the model cannot be easily quantified since there is a great scarcity of literature data on that specific aspect of lung morphometry.

At this point, a special note to the comparison between the results of the Deterministic model and the SHCM has to be made. It can clearly be seen that there is considerable difference in the absolute volume values calculated by each model. This in itself could imply that the two models could not coincide. However, this difference can be mostly attributed to three major factors: the inter-subject variability, the different numbers of airways per generation, which seems to be a complicating factor when symmetric models are associated to asymmetric ones, and the disparities introduced due to the digital nature of the data. Even more importantly, both models agree very well on the relative positioning of the airways within the lung space, an inference made with the help of the histograms in Figure 6-18 and corroborated by the 3D image in Figure 6-19. This is an important type of confirmation for the validity of the Deterministic Model, as both the positioning and the orientation of the airways constitute the greatest challenge for the implementation of any non-generalistic model of a bifurcating structure. This becomes even more significant since, as indicated by the work of Sauret, the root airways of a tree heavily affect the configuration of the whole bifurcating structure.

In conclusion, after several comparisons, the Deterministic Model finalised in this Section seems to fit really well with the data presented by previous studies in the field. The model has a series of key advantages, the most important of which is the correct placement of the individual airways in the lung space. Moreover, the model makes possible the quantification of morphometric data per segment of the lung, which is an original approach to lung modelling. Equally important is the fact that the bronchi geometry and configuration follows the local shape of the lung, as the sub-trees adapt to fit the contours of their relevant segments. Furthermore, both asymmetry and variability have been introduced to imbue the tree with characteristics apparent to the real biological bifurcating formations. Even if this initial variability may not be sufficient to fully characterise the human lungs, this attribute can be easily modified since the model implementation allows for adjustments to parameter values. This also allows for minor or major

modifications of the model to occur as the knowledge on the subject grows and more data become available by future projects.

6.4 Conclusion

In this chapter the creation of a fully descriptive model of the human tracheobronchial tree is illustrated. The algorithmic process for its development is broken down to 4 important sub-processes and each one is then investigated and discussed. The resulting tree structure, called the Deterministic Model, is subsequently analysed and compared to data and other models that are available in the literature. Furthermore, the model is validated also against the SHCM that was constructed in the previous chapter. The Deterministic Model agrees well with other projects studying the morphometry of the human lung; hence its validity is confirmed to a very high degree. In addition, the model enhances our knowledge of the human bronchial tree, with most of its attention directed towards the air-conducting portions of it. Even though certain improvements can be made, the Deterministic Model can become a very valuable tool in many applications that involve good knowledge of the lung mechanics, such as diagnosing disease with the help of medical imaging or predicting aerosol deposition, which is an important aspect of targeted inhalation therapy.

In the next chapter, which is the final part of this study, the conclusions of this project will be drawn and some suggestions as to the future work this line of research may take will be indicated.

Chapter 7

Conclusions and future work

7.1   Main Contributions

As has been mentioned in previous chapters, the importance of aerosolised medications as a method for targeting the respiratory and the vascular system of human patients using non-intrusive methods has increased, in direct connection with the international rise in medical practice standards and the technological developments transcending the field of medicine. Today, the respiratory tract is commonly being used as the entry point for particles deployed for both diagnosis and treatment purposes. However, in order to increase the efficiency of such methods, a good understanding of the aerosol behaviour when they penetrate the human lungs is required. This, in turn, demands intimate knowledge of the anatomy of the target organ in question so as to be able to predict the effects of a treatment and also to interpret the results of a diagnostic examination.

In the past, such knowledge came in the form of data extracted by morphometric studies of the lung, which could then be utilised in clinical applications via the use of generalistic statistical models. In this respect, the huge technological advances in medical imaging over the last few years, which had the additional effect of rapidly commercialising the relevant imaging methods, enabled clinicians to produce better images of the human tracheobronchial tree in-vivo; this gave a more focused insight into the workings and biological structures of the organ while it still functioned and paved the way for more efficient treatments and diagnostic tests through the use of patient-specific data.

Still, medical imaging technology currently places many limitations on the level of accuracy attainable in-vivo for clinical applications. For that reason,

only airways down to certain depth can be captured and analysed. Hence, the utilisation of anatomical lung models remains crucial for the creation of personalised treatments. The purpose of these models, which have evolved along with computer technology to be able to calculate the position and dimensions of airways in a descriptive fashion, is currently to enable experts to fill the gaps in anatomy in depths that cannot be studied by medical imaging modalities.

This project was undertaken in the Nuclear Medicine Department of Southampton General Hospital, where extended use of anatomical models is used in conjunction with medical imaging for clinical purposes. Several such models have been developed in the past; the goal of this thesis was to make certain improvements to them with the creation of new, enhanced anatomical models of the lung that would overcome the disadvantages of previous efforts and could be used in conjunction with medical imaging protocols to produce patient-specific data that could in turn be employed within the department. Furthermore, the 3D topology and morphology of the tree-structures predicted is investigated and then validated for these models. Special note has to be given to the availability of data for regions of the lung that have not been explored in such depth before. These two features represent the main contributions of this study.

7.2   Summary Of The Work

The first part of this project was concerned with the improvement of the Conceptual Model, which was developed for the use in medical imaging and aerosol deposition analysis within the Department. The improvements involved the introduction of two new major attributes: the inclusion of CT images of the first few airway generations of the airway tree to the core of the model and the more realistic spatial division of the calculated volumes per generation in the lung space. The results of this combined model, which

was named the Hybrid Conceptual Model (or HCM), were then validated to ensure its applicability.

Next, a method was developed for the subdivision of the lung space into smaller biological structures, the bronchopulmonary segments, based on the information acquired by the CT data. Very few efforts have been made in the past to model the lung space on the segmental level; the Segmental Model created was compared to them and to biological atlases and its validity was confirmed. In addition, a dynamic method for the generation of the Segmental Model with the use of minimal information on the initial morphology of the lung was outlined, resulting in the Segmental Atlas. To the best of our knowledge, this is an original concept first explored in this study. Finally, the HCM was expanded to fit the segmented lung, producing the Segmental Hybrid Conceptual Model (or SHCM).

The final part of the study expanded on the creation of a fully descriptive algorithm of the tracheobronchial tree morphology and topology in 3D. The algorithm was divided into 4 discrete steps, each of which was analysed and validated separately. The implementation of the algorithms was made in an efficient way, being able to provide results for each segment in a time-frame between 5-40 minutes. The initial inputs of the process are the first few airway generations of the human tracheobronchial tree, which may be either found using imaging modalities or via anatomical atlases, and a relevant confining space. The calculation of airway dimensions and orientation was performed with the help of mathematical principles known through previous studies to dominate the lung physiology and statistical datasets available to us through the relevant literature and was implemented using the MATLAB pc suite. The 3D realism of the final model, which is referred to as the Deterministic Model, is verified both visually and in comparison with other data. The new model was shown to have important advantages over many of its predecessors and to compare well with the morphometry of the lung. Furthermore, the data produced are available for each segment separately, an approach not encountered in any previous literature on the subject.

However, the lack of a variety of information hinders the further improvement and verification of the results.

7.3   Future Work

With regards to the SHCM, a more comprehensive way of combining the image data and the model needs to be devised. Additionally, the volume distribution, which is an important aspect of the model, could possibly become even more lifelike by taking a shape different than the one imposed by a strictly radial distribution, as is currently the case.

Certain improvements can also be made to the Deterministic Model. A method for avoiding airway superposition, an issue not addressed in this thesis, needs to be devised to add to the 3D reality of the data. Furthermore, more dynamic methods for the selection of the airway morphometries, with reference to the local lung space, could be developed. This can be investigated in conjunction with an exploration of the parameter space of the algorithm and the utilisation of non-tubular shapes for the bronchi; in fact, no curvature was considered for the airways in this project, which is an unrealistic assumption for so complex a biological structure as the human lung.

In more general terms, all studies of this sort suffer from the lack of a standardised set of morphometric data that can be used for comparison and validation purposes. This lack of information did not allow for further validation of the realism of the Deterministic Model. For that reason, some particular characteristics of the lung morphology, such as the inter- and intra-subject variability of the morphometry per segment, cannot be quantified. In the future, a database in which several sets of data are catalogued would be invaluable not only for lung modellers but also for aerosol deposition and other anatomical studies.

Appendix A

Flow-chart representation of the Deterministic Model algorithmic processes

The appendix contains:

1. The flow chart of the unconstrained-tree process.
2. The flow chart of the envelope-space calculation process.
3. The flow chart of the expansion-dilation process.

1. The unconstrained-tree process

(6, 8)

9. Calculation of symmetric morphometry of "daughters" branching out of predetermined "mother" (utilise angle detection routines)

(20)

10. Calculation of "mother"vector.

14. Calculate the coordinates from origin of two "daughter" vectors on the x-y plane of a unitary Cartesian coordinate system employing the length and branching angle.

The segmental data table contains more than 1 entry

15. Perform rotation on the two "daughters" according to the planar rotation angle calculated.

Yes

No

11b. Calculation of "mother's" sibling vector from the segmental data.

Full initial condition data on airways exist

Yes

No

11a. Calculation of "mother's" sibling vector from the initial condition data.

11c. Defind the "mother's" sibling as the extrapolation of the mother vector on the x-y plane with the "mother" start point as the origin.

12. Calculation of the "mother" plane normal vector.

13. Calculation of the axes defining a rotated Cartesian system using the "mother" vector, the normal vector and their cross-product.

(16)

(13, 15)

16. Re-rotate the planar-rotated "daughter" vectors so that the unitary Cartesian system axes match the rotated Cartesian system axes, maintaining the origin unchanged.

17. Displace the "daughters" to the original airway-tree coordinate system.

"Daughters" are symmetric

Yes

(7)

21. Redefine the "mother" airway to be the next available in the table of segmental data.

"Daughters" are within the confining space

No

Yes

18. Store "daughters" as new entry positions at the end of the data table.

19. Predict which "daughter" is the major and which the minor.

20. Calculate the morphometry for the major and the minor "daughter".

(14)

2. The envelope-space calculation process

1. Inputs: Airway coordinate table, ID table

2. Calculation of the surface elements of the envelope and classification of the triangular facets forming it in tabular form using a convex hull determination algorithm.

3. Pick the next triangular facet.

4. Calculate the vertices of a triangle equivalent to the facet in 2D.

6. Calculate a new rotated axial system based on the orientation of the facet.

5. Calculate the integer points that comprise the 2D triangle surface.

7. Rotate the 2D integer points to fit the rotated axial system orientation.

8. Displace the rotated integer points to the original coordinate system.

9. Store the displaced integers into a 3D matrix.

More unprocessed facets exist

Yes

No

10. Filter the stored 3D space with a 3D unitary cubic filter to induce robustness to the surface.

11. Fill the empty internal voxels confined by the surface.

12. End of the Process.

3. The expansion-dilation process

12. Calculate the "daughter" shadows on the axis defind by the unit vector.

13. Calculate the new "daughter" shadows based on the ratio

$$\text{new shadow} = \text{old shadow} \times \frac{\text{segment length}}{\text{envelope length}}.$$

14. Get the difference vector between the new and the old shadow.

15. Add the difference vector to the "daughter" vectors thus forming the expanded-dilated version of the airways.

16. Calculate the "daughter" morphometry and store in their relevant positions in the final table.

17. Recalculate the coordinates (using rotation, displacement) of the airways that form the subtrees with roots the newly calculated "daughters" without changing the already found morphometries.

18. Apply the envelope-space calculation algorithm to obtain the space occupied by the modified tree.

19. Choose the next mother in the final table.

20. Check the generation number of most distal expanded-dilated "daughters" already stored in the final table.

Yes ← Generation number < 16 → No

Glossary

Generation In a bifurcating system, each branching gives rise to a new generation of units.

Hilum The position where the main bronchi penetrate into the lungs.

Lung Edge While following a straight line, an edge is defined as the point where the transition from the inside to the outside (or the opposite) occurs.

Mother In a bifurcating branching system, mother is defined as the branch that gives rise to two or more branches that are more distal to the stem than the mother itself.

Voxel Unit element of a 3D volume image. It is the equivalent of the pixel, i.e. picture element, a term typically used in 2D imaging.

References and Bibliography

M.S. Albert, G.D. Gates, B. Driehuys, W. Happer, B. Saam, C.S. Springer Jr. and A. Wishnia, *"Biological magnetic resonance imaging using laser-polarized 129Xe"*, Nature 370:199-201, 1994.

J.S. Andrade Jr., A.M. Alencar, M.P. Almeida, J. Mendes Filho, S.V. Buldyrev, S. Zapperi, H.E. Stanley and B. Suki, "Asymmetric flow in symmetric branched structures", Phys. Rev. Letters, 81: 926-929, 1998.

D. Aykac, E.A. Hoffman, G. McLennan and R.M. Reinhardt, *"Segmentation and analysis of the human airway tree from three dimensional X-ray CT images"*, IEEE Transactions on Medical Imaging, 22:940-950, 2003.

C.B. Barber, D.P. Dobkin and H.T. Huhdanpaa, *"The Quickhull Algorithm for Convex Hulls"*, ACM Trans. Mathematical Software, 22: 469-483, 1996.

M.I. Baskin, A.G. Abd and J.S. Ilowite, *"Regional deposition of aerosolized pentamidine. Effects of body position and breathing pattern"*, Ann. Intern. Med., 113: 677-683, 1990.

F.J. Beekman, C. Kamphuis and E.C. Frey, *"Scatter compensation methods in 3D iterative SPECT reconstruction: A simulation study"*, Phys. Med. Biol. 42: 1619-1632, 1997.

J.D. Blanchard, J. Heyder, C.R. Donnell and J.D. Brain, *"Aerosol-derived lung morphometry: comparisons with a lung model and lung function indexes"*, J. Appl. Physiol., 71: 1216-1224, 1991.

E.A. Boyden, *"The structure of the pulmonary acinus in a child of six years and eight months"*, Am. J. Anat., 132: 275-300, 1971.

G. Bonsignore and G. Cumming, *"The Lung and its environment"*, Plenum Press, New York-London, 1980.

R.H. Brown and E. Zerhouni, *"New techniques and developments in physiologic imaging of airways"*, Radiol. Clin. North Am., 36(1): 211-230, 1998.

R.H. Brown, E.A. Zerhouni and W. Mitzner, *"Visualisation of airway obstruction in vivo during pulmonary vascular engorgement and edema"*, J. Appl. Physiol., 78(3): 1070-1078, 1995.

P.H. Burri, *"Fetal and postnatal development of the lung"*, Ann. Rev. Physiol., 46: 617-628, 1984.

S. Busayarat, T. Zrimec, *"Detection of Bronchopulmonary Segments on High-Resolution CT – Preliminary Results"*, Proceedings 20th IEEE Inter. Sympos. on Computer Based Med. Systems, 199-204, 2007.

J.P. Butler, *"The Green's function for the convection-diffusion equation in an analytic lung model"*, Bull. Math. Biol., 39(5): 543-563, 1977.

C.G. Caro, D.J. Doorly, M. Tarnawski, K.T. Scott, Q. Long and C.L. Dumoulin, *"Non-planar curvature and branching of arteries and non-planar type flow"*, Proceedings of the Royal Society of London: Mathematical, Physical and Engineering Sciences, 452: 185-197, 1996.

C.G. Caro, R.C. Schroter, N. Watkins, S.J. Sherwin and V. Sauret, *"Steady inspiratory flow in planar and non-planar models of human bronchial airways"*, Proceedings of the Royal Society of London A: Mathematical, Physical and Engineering Sciences, 458: 791-809, 2002.

A. Chartuvedi and Z. Lee, *"3 dimensional segmentation and skeletonisation to build an airway tree data structure for small animals"*, Phys. Med. Biol., 50: 1405-1419, 2005.

R.V. Damadian, *"Tumor detection by Nuclear Magnetic Resonance"*, Science, 171: 1151, 1971.

E. Denny and R.C. Schroter, *"A mathematical model for the morphology of the pulmonary acinus"*, J. Biomech. Eng., 118: 210-215, 1996.

M.J. Egan and W. Nixon, *"A model of aerosol deposition in the lung for use in inhalation dose assessment"*, Radiation Protection Dosimetry, 11(1): 5-17, 1985.

W. Findeisen, *"Uber das absetzen kleiner, in der luft suspendierte teilchen in der menschlichen lunge bei der atmung"*, Pfluegers Arch., 236: 367-379, 1935.

W.H. Finlay, K.W. Stapleton, H.K. Chan, P. Zuberbuhler and I. Gonda, *"Regional deposition of inhaled hygroscopic aerosols: in vivo SPECT compared with mathematical modelling"*, J. Appl. Physiol., 81(1): 374-383, 1996.

J.S. Fleming, *"A technique for using CT images in attenuation correction and quantification in SPECT"*, Nuclear Med. Comm., 10: 83-97, 1989.

J.S. Fleming, J.H. Conway, S.T. Holgate, A.G. Bailey and T.B. Martonen, *"Comparison of methods for deriving aerosol deposition by airway generation from three-dimensional radionuclide imaging"*, J. Aerosol Sci., 10: 1251-1259, 2000.

J.S. Fleming, A.H. Hashish, J.H. Conway, R. Hartley-Davies, M.A. Nassim, M.J. Guy, J. Coupe, S.T. Holgate, E. Moore, A.G. Bailey and T.B. Martonen, "*A technique for simulating radionuclide images from the aerosol deposition pattern in the airway tree*", J. Aerosol Med., 10(3):199-212, 1997.

J.S. Fleming, A.H. Hashish, J.H.Conway, M.A. Nassim, S.T. Holgate, P. Halson, E. Moore, A.G. Bailey and T.B. Martonen, "*Assessment of deposition of inhaled aerosol in the respiratory tract of man using three-dimensional multimodality imaging and mathematical modeling*", J. Aerosol Med., 9(3): 317-327, 1996.

J.S. Fleming, M. Nassim, A.H. Hashish, A.G. Bailey, J. Conway, S. Holgate, P. Halson, E. Moore and T.B. Martonen, "*Description of pulmonary deposition of radiolabeled aerosol by airway generation using a conceptual three dimensional model of lung morphology*", J. Aerosol Medicine, 8: 341-356, 1995.

J.S. Fleming, V. Sauret, J.H. Conway, S.T. Holgate, A.G. Bailey and T.B. Martonen, "*Evaluation of the accuracy and precision of lung aerosol deposition measurements from single-photon emission computed tomography using simulation*", J. Aerosol Med., 13(3): 187-198, 2000.

J.S. Fleming, V. Sauret, J.H. Conway and T.B. Martonen, "*Validation of the conceptual anatomical model of the lung airway*", J. Aerosol Medicine, 17:260-269, 2004a.

J.S. Fleming, D.R. Whalley, J.V. Skrypniuk, P.H. Jarritt, A.S. Houston, P.S. Cosgriff and D. Bailey, "*UK audit of relative lung function measurement from planar radionuclide imaging*", Nucl. Med. Commun. 25: 923-934, 2004b.

T.R. Gerrity, C.S. Garrard and D.B. Yeates, "*Theoretic analysis of sites of aerosol deposition in the human lung*", Chest, 80(6): 898-901, 1981.

T.R. Gerrity, P.S. Lee, F.J. Hass, A. Marinelli, P. Werner and R.V. Lourenco, "*Calculated deposition of inhaled particles in the airway generations of normal subjects*", J. Appl. Physiol., 47(4): 867-873, 1979.

H. Gray, "*Anatomy of the human body*", Philadelphia: Lea & Febiger; (Bartleby.com, http://www.bartleby.com/107/240.html#i970, 2000), 1918.

J.F. Green, "*Mechanical concepts in Cardiovascular and pulmonary physiology*", Henry Kimpton Publishers, London, 1977.

G.M. Green, G.J. Jakab, R.B. Low and G.S. Davis, "*Defense mechanisms of the respiratory membrane*", Am. Rev. Resp. Dis., 115:479-514, 1977.

J.F. Golden, J.W. Clark and P.M. Stevens, "*Mathematical modelling of pulmonary airway dynamics*", IEEE Transactions on Biomedical Engineering BME-20, 4:397-404, 1973.

B. Haefeli-Bleuer and E.R. Weibel, *"Morphometry of the human pulmonary acinus"*, Anatomical Record 220: 401-414, 1988.

J.E. Hansen and E. P. Ampaya, *"Human air space shape, sizes, areas and volumes"*, Journal of Applied Physiology, 38: 990-995, 1975.

J.E. Hansen, E.P. Ampaya, G.H. Bryant and J.J. Navin, *"Branching pattern of airways and air spaces of a single human terminal bronchiole"*, J. Appl. Physiol., 38(6): 983-989, 1975.

A.H. Hashish, J.S. Fleming, J.H. Conway, P. Halson, E. Moore, T.J. Williams, A.G. Bailey, M. Nassim and S.T. Holgate, *"Lung deposition of particles by airway generation in healthy subjects: three-dimensional radionuclide imaging and numerical model prediction"*, J. Aerosol Sci., 29: 205-215, 1998.

J. Heyder, L. Armbruster, J. Geghart, E. Grein and W. Stahlhofen, *"Total deposition of aerosol particles in the human respiratory tract for nose and mouth breathing"*, J. Aerosol Sci., 6: 311-328, 1975.

W. Hofmann, B. Asgharian and R. Winkler-Heil, *"Modeling intersubject variability of particle deposition in human lungs"*, J. Aerosol Science, 33: 219-235, 2002.

K. Horsfield and G. Cumming, *"Angles of branching and diameters of branches in the human bronchial tree"*, Bull. Math. Biophys. 29:245-259, 1967.

K. Horsfield and G. Cumming, *"Morphology of the bronchial tree in man"*, Journal of Applied Physiology, 24(3): 373-383, 1968.

K. Horsfield, G. Dart, D.E. Olson, G.F. Filley and G. Cumming, *"Models of the human bronchial tree"*, Journal of Applied Physiology, 31: 207-217, 1971.

K. Horsfield and A. Thurlbeck, *"Volume of the conducting airways calculated from morphometric parameters"*, Bull. Math. Biol, 43:101-109, 1981(a).

K. Horsfield and A. Thurlbeck, *"Relation between diameter and flow in branches of the bronchial tree"*, Bull. Math. Biol., 43: 681-691, 1981(b).

International Commission on Radiological Protection (ICRP) Task Group on Lung Dynamics, *"Deposition and retention models for internal dosimetry of the human respiratory tract"*, Health Physics, 12: 173-207, 1966.

International Commission on Radiological Protection (ICRP) Task Group, *"Publication 66. Human Respiratory tract model for radiological protection"*, Pergamon, 1994.

A. Kamiya, T. Togawa and A. Yamamoto, *"Theoretical relationship between the optimal models of the vascular tree"*, Bull. Math. Biol., 36: 311-323, 1974.

H.U. Kauczor, "*Commentary: Helium-3 imaging of pulmonary ventilation*", Brit. J. Radiol., 71: 701-703, 1998.

H.U. Kauczor, R. Surkau and T. Roberts, "*MRI using hyperpolarized noble gases*", Eur. Radiol., 8: 820-827, 1998.

M. King, A. Gilboa, F.A. Meyer and A. Silberberg, "*On the transport of mucus and its rheologic simmulants in ciliated systems*", Am. Rev. Resp. Dis., 113:347-379, 1974.

H. Kitaoka, R. Takaki and B. Suki, "*A three-dimensional model of the human airway tree*", J. Appl. Physiol, 87: 2207-2217, 1999.

H. Kitaoka, S. Tamurai and R. Takaki, "*A three-dimensional model of the human pulmonary acinus*", J. Appl. Physiol, 88: 2260-2268, 2000.

L. Koblinger and W. Hofmann, "*Analysis of human lung morphometric data for stochastic aerosol deposition calculations*", Phys. Med. Biol. 30: 541-556, 1985.

L. Koblinger and W. Hofmann, "*Monte Carlo modeling of aerosol deposition in human lungs. Part I: Simulation of particle transport in a stochastic lung structure*", J. Aerosol Science, 21(5): 661-674, 1990.

E. Kresch, "*Cross-sectional shape of flexible tubes*", Bull. Math. Biol., 39(6): 679-691, 1977.

H.D. Landahl, "*On the removal of airborne droplets by the human respiratory tract. I. The lung*", Bull. Math. Biophys., 12:43-56, 1950.

Z. Lee and M.S. Berridge, "*PET Imaging-based evaluation of aerosol drugs and their delivery devices: nasal and pulmonary studies*", IEEE Trans. Med. Imaging, 21(10): 1324-1331, 2002.

Z. Lee, M.S. Berridge, W.H. Finlay and D.L. Heald, "*Mapping PET-measured triamcinolone acetonide (TAA) aerosol distribution into deposition by airway generation*", International Journal of Pharmaceutics, 199: 7-16, 2000.

P.T. Macklem, R.G. Fraser and D.V. Bates, "*Bronchial pressures and dimensions in health and obstructive airway disease*", J. Appl. Physiol, 18: 699-706, 1963.

T.B. Martonen, "*On the fate of inhaled particles in the human: a comparison of experimental data with theoretical computations based on a symmetric and asymmetric lung*", Bull. Math. Biol., 45(3): 409-424, 1983.

T.B. Martonen, "*Mathematical model for the selective deposition of inhaled pharmaceuticals*", J. Pharm. Sci., 82(12): 1191-1199, 1993.

T.B. Martonen, C.J. Musante, R.A. Segal, J.D. Schroeter, D. Hwang, M.A. Dolovich, R. Burton, R.M. Spencer and J.D. Fleming, *"Lung models: Strengths and Limitations"*, Respiratory Care, 45: 712-736, 2000.

T.B. Martonen, J.D. Schroeter, D. Hwang, J.S. Fleming and J.H. Conway, *"Human lung morphology models for particle deposition studies"*, Inhal. Toxicol., 12:109-121, 2000.

T.B. Martonen, Y. Yang, D. Hwang and J.S. Fleming, *"Computer simulations of human lung structures for medical applications"*, Comput. Biol. Med., 25(5): 431-446, 1995.

R.R. Mercer and J.D. Crapo, *"Three-dimensional reconstruction of the rat acinus"*, J. Appl. Physiol., 63: 785-794, 1987.

J. Milic-Emili, J.A.M. Henderson, M.B. Dolovich, D. Trop and K. Kanenko, *"Regional distribution of inspired gas in the lung"*, J. Appl. Physiol., 21(3):749-759, 1966.

C. Mitsakou, C. Helmis and C. Housiadas, *"Eulerian modelling of lung deposition with sectional representation of aerosol dynamics"*, J. Aerosol Science, 36: 75-94, 2005.

S. Montesantos, *"Airway Tree Models: The Hybrid Conceptual Model"*, University of Southampton, Faculty of Medicine, Health and Life Sciences Postgraduate Conference, 31, 2006.

S. Montesantos, J.S. Fleming and L. Bolt, *"The Hybrid Conceptual Model of the Human Lung"*, Proceedings of the 10th Medical Image Understanding and Analysis Conference, 1: 36-40, 2006.

J.D. Mortensen, J.D. Young, L. Stout, A. Stout, B. Bagley and R.N. Schaap, *"A numerical identification system for airways in the lung"*, Anat. Record 206:103-114, 1983.

C.D. Murray, *"The physiological principle of minimum work"*, Procl. Natl. Acad. Sci. USA 12: 207-214, 1926.

J.A. Nadel, *"Physiology and pharmacology of the airways"*, Marcel Dekker, Inc., New York-Basel, 1980.

T.J. Pedley, *"Pulmonary Fluid Dynamics"*, Annual Review on Fluid Mechanics 9:229-274, 1977.

S. Perring, Q. Summers, J.S. Fleming, M.A. Nassim and S.T. Holgate, *"A new method of quantification of the pulmonary regional distribution of aerosols using combined CT and SPECT and its application to nedocromil sodium administered by metered dose inhaler"*, British Journal of Radiology, 67: 46-53, 1994.

R.F. Phalen, M.J. Oldham, C.B. Beaucage, T.T. Crocker and J.D. Mortensen, *"Postnatal enlargement of human tracheobronchial airways and implications for particle deposition"*, Anat. Record 212: 368-380, 1985.

R.F. Phalen, H.C. Yeh, O.G. Raabe and D.J. Velasquez, *"Casting the lungs in situ"*, Anatomical Record 177:255-264, 1973.

R.F. Phalen, H.C. Yeh, G.M. Schum and O.G. Raabe, *"Application of an idealized model to morphometry of the mammalian tracheobronchial tree"*, Anatomical Record 190: 167-176, 1978.

C.G. Phillips and S.R. Kaye, *"Diameter-based analysis of the branching geometry of four mammalian bronchial trees"*, Respiration Physiol. 102:303-316, 1995.

C.G. Phillips and S.R. Kaye, *"On the asymmetry of bifurcations in the bronchial tree"*, Respiration Physiol. 107: 85-98, 1997.

C.G. Phillips, S.R. Kaye and R.C. Schroeter, *"A diameter based reconstruction of the branching pattern of the human bronchial tree. Part I. Description and application"*, Respir. Physiol. 98:193-217, 1994(a).

C.G. Phillips, S.R. Kaye & R.C. Schroeter, *"A diameter based reconstruction of the branching pattern of the human bronchial tree. Part II. Mathematical formulation"*, Respir. Physiol. 98:219-226, 1994(b).

P.R. Phipps, I. Gonda, D.L. Bailey, P. Borham, G. Bautovich and S.D. Anderson, *"Comparisons of planar and tomographic gamma scintigraphy to measure the penetration index of inhaled aerosols"*, Am. Rev. Resp. Dis., 139(6): 1516-1523, 1989.

H.D. Prange, *"Laplace's law and the alveolus: A misconception of anatomy and a misapplication of physics"*, Adv. Physiol. Educ., 27: 34-40, 2003.

B. Quatember, *"Human respiratory system: Simulation of breathing mechanics and gas mixing processes based on non-linear mathematical model"*, 2003 International Conference on Health Sciences Simulation, 2003.

O.G. Raabe, H.C. Yeh, G.M. Schum and R.F. Phalen, *"Tracheobronchial Geometry: Human, Dog, Rat, Hampster (report LF-53)"*, Albuquerque, NM: Lovelace Foundation Medical Educational Resources, 1976.

V. Sauret, *"Topology and morphology of pulmonary anatomical features for aerosol deposition applications using medical imaging"*, PhD Thesis, 2000.

V. Sauret, P.M. Halson, I.W. Brown *et al.*, *"Study of the three-dimensional geometry of the central conducting airways in man using computed tomographic (CT) images"*, J. Anat. 200: 123-134, 2002.

V. Sauret, K.A. Goatman, J.S. Fleming and A.G. Bailey, "*Semi-automated tabulation of the 3D topology and morphology of branching networks using CT application to the airway tree*", Phys. Med. Biol. 44:1625-1638, 1999.

R.B. Schlesinger and L.A. McFadden, "*Comparative morphometry of the upper bronchial tree in six mammalian species*", Anat. Record 199: 99-108, 1981.

A. Schmidt, S. Zidowitz, A. Kriete *et al.*, "*A digital reference model of the human bronchial tree*", Computerised Medical Imaging and Graphics, 28:203-211, 2004.

J.P. Schreider and O.G. Raabe, "*Structure of the human respiratory acinus*", Am. J. Anat., 162: 221-232, 1981.

J.D. Schroeter, J.S. Fleming, D. Hwang and T.B. Martonen, "*A computer model of lung morphology to analyze SPECT images*", Computerised Med Imaging and Graphics, 26: 237-246, 2002.

M. Schum, H.C. Yeh, "*Theoretical evaluation of aerosol deposition in anatomical models of mammalian lung airways*", Bull. Math. Biol., 42(1): 1-15, 1980.

T. Sera, H. Fujioka, H. Yokota *et al.*, "*Three dimensional visualisation and morphometry of small airways from microfocal X-ray computed tomography*", J. Biomech., 36: 1587-1594, 2003.

T.T. Soong, P. Nicolaides, C.P. Yu and S.C. Soong, "*A statistical description of the human tracheobronchial tree geometry*", Respiration Physiol., 37: 161-172, 1979.

D.B. Taulbee and C.P. Yu, "*A theory of aerosol deposition in the human respiratory tract*", Journal of Applied Physiology, 38:77-85, 1975.

M.H. Tawhai and K.S. Burrowes, "*Developing integrative computational models of pulmonary structure*", Anat. Rec. B. New Anat., 275: 207-218, 2003.

M.H. Tawhai, P. Hunter, J. Tschirren, J. Reinhardt, G. McLennan and E.A. Hoffman, "*CT-based geometry analysis and finite element models of the human and ovine bronchial tree*", J. Appl. Physiol, 97:2310-2321, 2004.

M.H. Tawhai, A.J. Pullan and P.J. Hunter, "*Generation of an anatomically based three-dimensional model of the conducting airways*", Ann. Biomed. Eng., 28: 793-802, 2000.

A. Thurlbeck and K. Horsfield, "*Branching angles in the bronchial tree related to order of branching*", Respir. Physiol. 41: 173-181, 1980.

H.B.M. Uylings, *"Optimization of diameters and bifurcation angles in lung and vascular tree structures"*, Bull. Math. Biol. 39: 509-519, 1977.

B. Waters, J. Owers-Bradley and M. Silverman, *"Acinar structure in symptom free adults by Helium-3 magnetic resonance"*, Am. J. Respir. Crit. Care Med., 173(8): 847-851, 2006.

E.R. Weibel, *"Morphometry of the human lung"*, Heidelberg: Springer-Verlag, 1963.

E.R. Weibel, *"Design of airways and blood vessels as branching trees"*, In: R.G. Crystal, J.B. West, P.H. Barnes, N.S. Cherniak, E.R. Weibel, editors. The lung: Scientific foundations, vol. 1. New York: Raven Press, 711-720, 1991(a).

E.R. Weibel, *"Fractal Geometry: A design principle for living organisms"*, Am. J. Physiol., 261: L361-369, 1991(b).

E.R. Weibel, C.C. Hsia and M. Ochs, *"How much is there really? Why stereology is essential in lung morphometry"*, J. Appl. Physiol. Review, 2006.

B.J. West and W. Deering, *"Fractal Physiology for Physicists: Levy Statistics"*, Elsevier Science B.V., Amsterdam, 1994.

S.A. Wood, E.A. Zerhouni, J.D. Hoford, E.A. Hoffman and W. Mitzner, *"Measurement of three dimensional lung tre structures by using computed tomography"*, Journal of Applied Physiology, 79: 1687-1697, 1995.

H.C. Yeh & G.M. Schum, *"Models of the human lung airways and their application to inhaled particle deposition"*, Bull. Math. Biol. 42: 461-480, 1980.

C.P. Yu, *"A two-component theory of aerosol deposition in lung airways"*, Bull. Math. Biol., 40(6): 693-706, 1978.

C.P. Yu and C.K. Diu, *"A probabilistic model for intersubject deposition variability of inhaled particles"*, Aerosol Science Technology, 1: 335-362, 1982.

E.A. Zerhouni, C.J. Herold, R.H. Brown, R.C. Wetzel, C.A. Hirshman, J.L. Robotham and W. Mitzner, *"High-resolution computed-tomography -- physiologic correlation"*, J. Thorac. Imaging, 8(4): 265-272, 1993.